SYNTHESIS, PROCESSING, AND THERMOELECTRIC PROPERTIES OF GERMANIUM-ANTIMONY-TELLURIUM BASED COMPOUNDS AND ALLOYS

By

Jared Brett Williams

A DISSERTATION

Submitted to
Michigan State University
in partial fulfillment of the requirements
for the degree of

Materials Science and Engineering — Doctor of Philosophy

2017

ABSTRACT

SYNTHESIS, PROCESSING, AND THERMOELECTRIC PROPERTIES OF GERMANIUM-ANTIMONY-TELLURIUM BASED COMPOUNDS AND ALLOYS

By

Jared Brett Williams

Society has become increasingly more aware of the negative impacts which nonrenewable energy sources have on the environment, and therefore the search for new and more efficient means of energy production has become an important research endeavor. Thermoelectric modules possess the unique ability to convert wasted heat into useful electrical energy via solid state processes, which could vastly improve the efficiency of a number of applications. The materials which accomplish this are typically comprised of semiconductors which exhibit high electrical conductivity, Seebeck coefficient, and thermal resistivity. Together these properties give us a gauge for the overall efficiency of the thermal to electrical energy conversion. Phase change materials are a class of materials primarily used for optical data storage in CDs, DVDs, and Blu-Ray discs. Today's state of the art phase change materials are based on alloys of GeTe and Sb_2Te_3. These materials have also been found to exhibit high thermoelectric efficiencies. These high efficiencies stem from their complex crystal structure and degenerate semiconducting nature. The purpose of this work was to study and engineer the thermoelectric properties of various alloys and compounds which belong to this family of materials. Specifically studied were the compounds Ge_4SbTe_5 and $Ge_{17}Sb_2Te_{20}$. In each case various synthesis and processing strategies were implemented to increase the thermoelectric performance and better understand the fundamental electrical and thermal properties. Finally various proposals for future work on these materials are presented, all of which are based on the findings described herein.

I would like to dedicate this work to Teresa McConnell. An amazing woman who poured her love and soul into everyone she knew. Teresa, I know you would be proud. Rest in peace.

1963-2014

ACKNOWLEDGMENTS

I would like to acknowledge my advisor, Dr. Donald T. Morelli. Thank you for creating an environment which was nurturing, challenging, and accepting of all questions and ideas. I would also like to thank my doctoral committee Dr. Richard Lunt, Dr. Yue Qi, and Dr. Nelson Sepulveda. This work was supported at Michigan State University as part of the Center for Revolutionary Materials for Solid State Energy Conversion, an Energy Frontier Research Center funded by the U.S. Department of Energy, Office of Science, Office of Basic Energy Sciences under Award Number DE-SC0001054. I would like to acknowledge financial support from the Michigan State Graduate School through the University Distinguished Fellowship. I would like to acknowledge Karl Dersch from the laboratory of Dr. Timothy Hogan for assistance with spark plasma sintering and thermal diffusivity measurements. I would also like to acknowledge the laboratory of Dr. Ctirad Uher at the University of Michigan for the many collaborations over the years. I would like to acknowledge Dr. Alex Zevalkink and David Smiadak for assistance with high temperature X-ray diffraction.

I would like to thank my wife, Morgan, and children, Addison, Dakota, and Chandler. Despite what stresses and hardships I faced they always had a way of helping me keep them in perspective and remember what the truly important aspects in life are. I would like to acknowledge all of the researchers I had the pleasure of working with at Michigan State University, particularly Spencer Waldrop, Winston Carr, and Spencer Mather. Thank you for the many fruitful discussions over coffee and beer as well the countless hours of assistance in the lab. Go for the Gusto! The success of my life thus far would not stand without the amazing support and love of my family. To my parents and grandparents, both biological and by marriage, thank you for the unwavering support and love throughout these years.

Scott Williams, Lisa Adams, Teresa McConnell Williams, Robert Adams, Gayle Fowler, Allan Fowler, and Daniel Wesley to name a few (if I missed your name I am truly sorry). To say this would have been impossible without you is an understatement. I can only hope to spend the rest of my life paying the selflessness forward. To my brothers, thank you for being a constant source of joy in my life. I would also like to acknowledge Karl Fowler, you have an amazing mind and bring a smile to my face. I would like to thank all of the support throughout these years from my friends, Evan Bibb, Jordan Jones, Josh Lee, and Dallas Viva, and many more which I could not name here simply due to length constraints. To my undergraduate advisor, Dr. Terry Tritt, thank you for believing in me and laying the foundations for my career in materials science and solid state physics. I would also like to the thank mentorship and guidance from Dr. Dale Hitchcock and Dr. Daniel Thompson, who spent hours in the lab at Clemson University answering questions from an interested undergraduate. Lastly, I would like to acknowledge the musical writings of Antonín Dvořák, Andy McKee, Hanz Zimmer, B.B. King, and John Mayer.

TABLE OF CONTENTS

LIST OF TABLES

LIST OF FIGURES

Chapter 1

Introduction: Electronic and Thermal Properties of Semiconductors

The United States consumed approximately 97.5 Quads of energy in 2015 alone.[1] One Quad is equivalent to 10^{15} BTU of energy, or $1.055x10^{18}$J. In fact, since 1976 the total energy consumed by the United States has increased more than 35%, and although we are more technologically advanced, the percentage of that energy which is rejected has also increased, as can be seen in Figure 1.1.

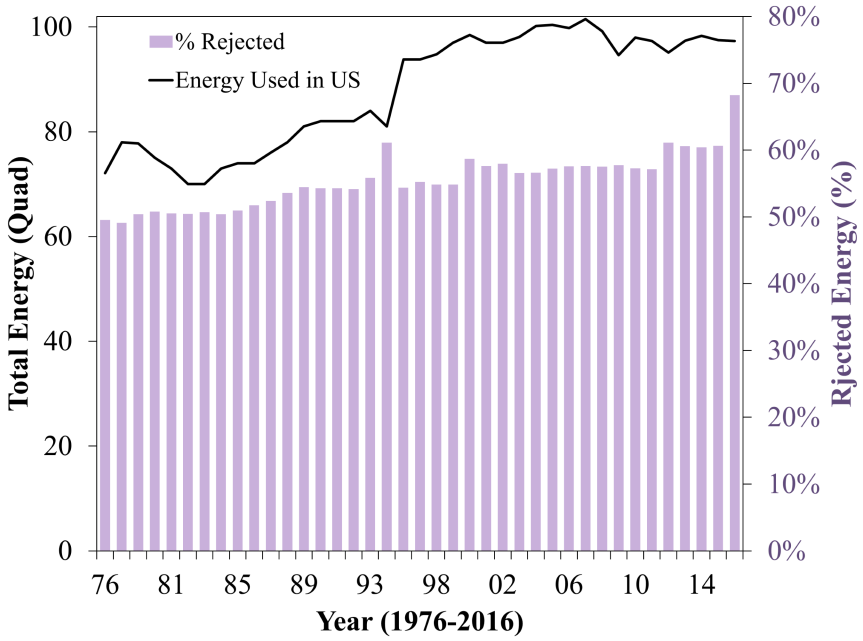

Figure 1.1: The total energy consumed in the United States since 1976 (black line), with the percent which is rejected represented by purple bars.

This rejected energy is mainly in the form of waste heat and represents a large untapped energy source. Additionally, the majority of the energy produced was done using resources which are nonrenewable such as petroleum, coal, and natural gas. The combustion of these resources has also been shown to emits high levels of CO_2, which contributes to global warming by the greenhouse effect.[2, 3] Carbon neutral resources such as solar, nuclear, wind, geothermal, and biomass had a combined total of less than 20%. Thermoelectric materials could alleviate this issue by using the wasted heat from a number of processes and directly converting it back into useful electricity.

1.1 Thermoelectric Power Generation

Thermoelectric materials posses the ability to convert wasted thermal energy directly into useful electrical energy through a direct, solid-state process. Thermoelectric modules are the

leading design for waste-heat recovery and cooling applications. These modules consist of an array of n-type and p-type thermoelectric legs, which are placed in series electrically and in parallel thermally, as can be seen in Figure 1.2.

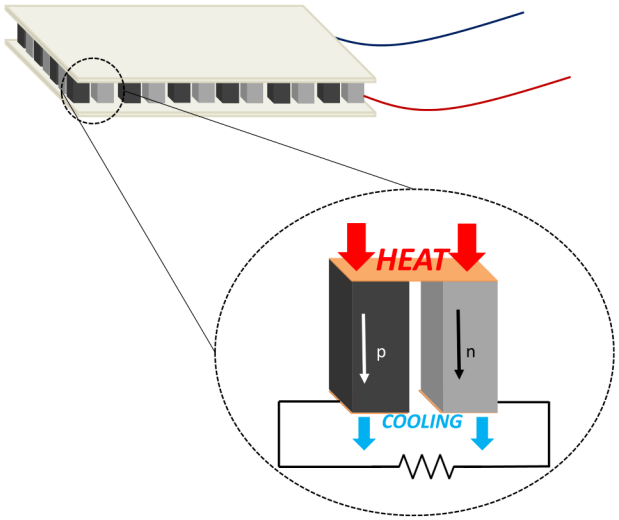

Figure 1.2: Modern day thermoelectric module and unicouple. Governed by the Seebeck effect, electrons and holes will flow according to a temperature gradient established by a heat source and generate a voltage difference.

In the presence of a temperature gradient the holes and electrons in the p-type and n-type legs, respectively, will respond by generating an electric field until an equilibrium is established. The result is a voltage difference ΔV which directly balances the temperature difference ΔT. The ratio of voltage difference to temperature difference is related to an intrinsic property of all materials, the Seebeck coefficient S. The efficiency of a number of applications which produce waste heat could be improved by incorporating thermoelectric devices. However, the current utilization of thermoelectric modules is limited to niche applications, which can be traced to the high cost of synthesis and low efficiency.

The efficiency of a thermoelectric generator is dependent upon the Carnot efficiency and

the unitless parameter ZT, as can be seen in equation (1.1).

$$\eta = \left(\frac{T_H - T_C}{T_H}\right)\left(\frac{\sqrt{1+ZT_{avg}}-1}{\sqrt{1+ZT_{avg}}+(\frac{T_C}{T_H})}\right) \tag{1.1}$$

where T_H, T_C, and T_{avg} are the hot side temperature, cold side temperature, and average temperature of the thermoelectric legs, respectively. From equation (1.1) it is clear to see that a high efficiency thermoelectric module can be obtained by increasing the temperature difference between T_H and T_C and/or increasing ZT_{avg}. The dimensionless figure-of-merit ZT and the materials properties which define it will be discussed in greater detail in subsequent sections. The square-root dependence of efficiency on ZT implies that the greatest gains in efficiency from improving ZT will happen for values less than approximately 4, as can be seen in Figure 1.3(a).

The majority of today's state-of-the-art thermoelectric materials exhibit ZT values approximately equal to unity or slightly higher. Some representative compounds include, but are not limited to, Bi_2Te_3, PbTe, $Cu_{12}Sb_4S_{13}$, and $AgPb_xSbTe_{2-x}$, which can be seen in Figure 1.3(b).[4, 5, 6, 7] The primary focus of thermoelectrics research has gone into finding new materials with increased stability, higher ZT values, and more cost effective and earth abundant comprising elements.

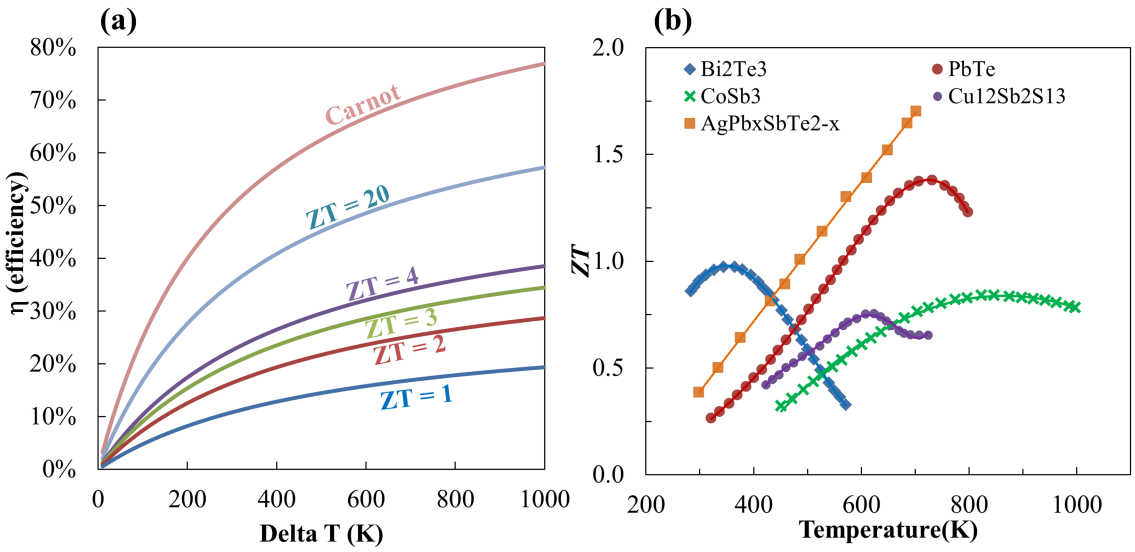

Figure 1.3: (a) Thermoelectric efficiency (η) versus ΔT for various ZT values. (b) ZT versus temperature for Bi_2Te_3, PbTe, $Cu_{12}Sb_4S_{13}$, and $AgPb_xSbTe_{2-x}$.[4, 5, 6, 7]

1.2 Thermoelectric Phenomena

In 1821 Thomas Johann Seebeck found that when the junctions of two dissimilar metals were held at different temperatures a compass needle would be deflected.[8] This was originally thought to be due to the generation of a magnetic field from the temperature difference, but it was soon realized that an electric current was the source. More specifically, the magnitude of the voltage difference is directly proportional to the temperature difference and related by S, the Seebeck coefficient ($\Delta V = -S\Delta T$). This effect stems from a difference in Fermi levels between the dissimilar materials and the temperature dependence of the Fermi energy in a metal, as will be discussed later, and is the basis for modern day thermocouples. Using two materials with well defined Seebeck coefficients, an absolute temperature can be determined based on the voltage generated from a temperature difference as can be seen in Figure 1.4.

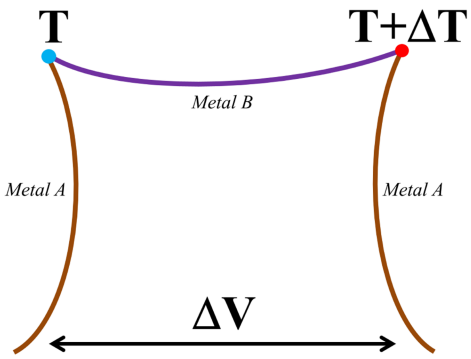

Figure 1.4: When the junction of two dissimilar metals are held at different temperatures a voltage difference will be generated, which is governed by the Seebeck coefficient.

In 1834 the French watchmaker Jean Charles Athanase Peltier observed that by applying an electrical current through a system similar to that seen in Figure 1.1 heat would either be rejected or absorbed at the junctions, depending on the direction of the current.[9] The quantity of heat rejected or absorbed at a junction is related to the Seebeck coefficient, which is expressed using the following relation:[10]

$$\Pi = ST \tag{1.2}$$

where Π is the Peltier coefficient, S is the Seebeck coefficient, and T is the temperature. A third related property is the Thomson effect (γ), which can also be expressed in terms of the Seebeck coefficient:[11]

$$\frac{\gamma}{T} = \frac{dS}{dT} \tag{1.3}$$

The Seebeck coefficient is the fundamental phenomenon governing thermoelectric power generation, whereas the Peltier effect is the basis for thermoelectric refrigeration. Both refrigeration and power generation for thermoelectrics are dependent on ZT, the dimensionless

figure-of-merit which is derived from intrinsic physical properties:

$$ZT = \frac{S^2\sigma}{\kappa_e + \kappa_l}T = \frac{S^2}{\rho(\kappa_e + \kappa_l)}T \tag{1.4}$$

where S is the Seebeck coefficient, σ is the electrical conductivity (the inverse of which is ρ, the electrical resistivity), κ_e is the electronic component of thermal conductivity, and κ_l is the lattice component, which sum to yield the total thermal conductivity, and T is the operating temperature. To achieve high-ZT it can be seen from equation 1.3 that a low thermal conductivity and high $S^2\sigma$ (or power factor, PF) is desirable. More specifically, lowering thermal conductivity is generally achieved through lowering the lattice component, κ_l, because, for a given temperature the ratio of $\frac{\kappa_e}{\sigma}$ is constant due to the constraints of the Weidemann-Franz Law, which is stated as thus:[12]

$$\kappa_e = L\sigma T \tag{1.5}$$

where L is the Lorenz number, generally taken as $2.44 * 10^{-8}\mathrm{W\Omega K^{-2}}$. Additionally, the Seebeck coefficient, which scales indirectly with carrier concentration, competes with the electrical conductivity.

Because of the contraindicated nature of the electrical and thermal properties which comprise ZT, sophisticated materials engineering is needed to achieve values which would render thermoelectric materials viable for commercial utilization. In the following sections each of the aforementioned properties will be discussed in detail, and the methods used to achieve high ZT values in today's state-of-the-art materials will be presented.

1.2.1 Electrical Conductivity in Semiconductors

For the general case of a semiconductor containing both electrons holes the electrical conductivity (σ) is expressed as:[11]

$$\sigma = \mu_e e n + \mu_h e p \tag{1.6}$$

where μ_e and μ_h are the mobilities for electrons and holes, respectively, n and p are the electron and hole concentrations, respectively, and e is the fundamental unit of charge ($1.602x10^{-19}$C). In the case where $n \gg p$, or vice versa, equation (1.6) can be further reduced to contain only the contributions from the dominant carrier. To determine and understand the nature of the charge carrier concentration and the charge carrier mobility which determine the electrical conductivity, one must undergo a more rigorous study of the fundamental way in which electrons behave in materials.

Electrons obey the Pauli exclusion principle, which states that no two electrons can have the same quantum state. Because electrons are indistinguishable a statistical analysis is applied to determine the probability of finding an electron at a specific energy, as is expressed by the Fermi-Dirac distribution:[13]

$$f(E) = \frac{1}{1 + e^{\frac{E - E_F}{k_B T}}} \tag{1.7}$$

In equation (1.7) E is the energy, E_F is the Fermi energy, k_B is the Boltzmann constant ($8.617 * 10^{-5}\text{eVK}^{-1}$), and T is the temperature. It is clear to see from equation (1.7) that at $T = 0K$ all states below E_f are filled and all states at energies above the E_F are unfilled. As T increases electrons from lower energy states become excited and fill states with higher

energy. This distribution can be seen in Figure 1.5. At high enough temperatures the Fermi-Dirac distribution approaches that of a classical Boltzmann distribution.[14]

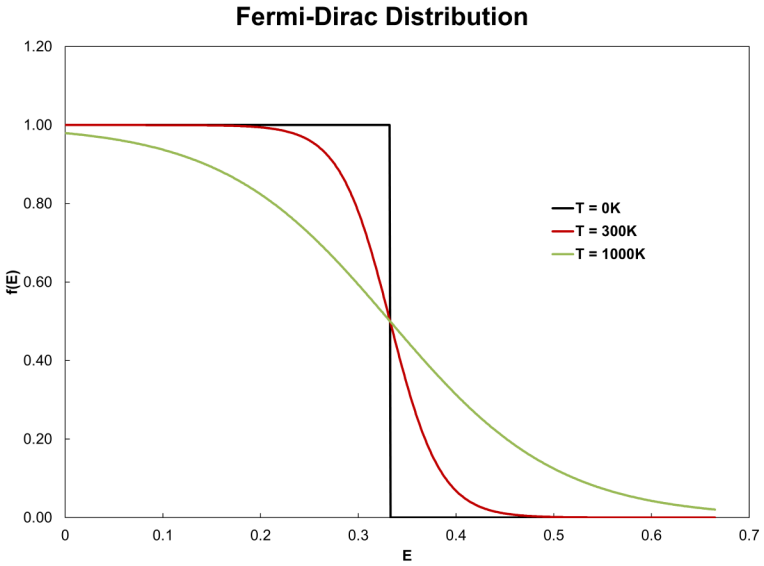

Figure 1.5: Fermi-Dirac distribution at 0K, 300K, and 1000K.

In metals the Fermi energy resides deep within the conduction band, while in an insulator the band gap is typically too large for thermal excitation, and the Fermi energy therefore is defined as residing halfway between the top of the highest energy filled band (valence band) and the lowest energy unfilled band (conduction band) inside the forbidden energy gap. A semiconductor is defined as a material with a band gap, but typically has bandgap energies on the order of a few eV. The density of states available for electronic population, *g(E)dE*, is defined as the number of states in the energy interval E to $E+dE$ per unit volume. For the case of free electrons the density of states is defined as:[13]

$$g(E) = \frac{1}{2\pi^2}\left[\frac{2m}{\hbar^2}\right]^{3/2} E^{1/2} \tag{1.8}$$

An integration of the Fermi-Dirac distribution weighted by the electronic density-of-states as a function of energy yields the carrier concentration in a solid, as can be seen in equation

(1.9).[13]

$$n = \int_0^\infty f_n(E) g(E) dE \tag{1.9}$$

By combining equations (1.8) and (1.9) the electron concentration in a metal can be expressed as:

$$n = \int_0^\infty \frac{1}{2\pi^2} \left[\frac{2m}{\hbar^2}\right]^{3/2} E^{1/2} \left[\frac{1}{1 + e^{\frac{E-E_f}{k_B T}}}\right] dE \tag{1.10}$$

1.2.1.1 Transport in Intrinsic and Extrinsic Semiconductors

Unlike metals, semiconductors contain a band gap in their band structure. The bandgap changes the transport equations, because in order for electronic conduction to take place electrons must be thermally excited into the conduction band. The carrier concentration will now be defined in relation to the band edge (E_C for the conduction band and E_V for the valence band):

$$n = \int_{E_C}^\infty g(E) f(E) dE \tag{1.11}$$

where the density of states, $g(E)$ for semiconductors is defined as:[13]

$$g(E) = g_c \frac{\sqrt{2}}{\pi^2} \frac{(E - E_C)^{1/2}}{\hbar^3} (m^*)^{3/2} \tag{1.12}$$

where g_c is the band degeneracy, which is defined as the overlap of energy bands, and m^* is the effective mass of the charge carrier, in this case electrons, and $\hbar$ is the Planck constant divided by 2π ($\hbar = h/2\pi = 1.054x10^{-34} Js$). The effective mass is a tensor quantity which

is best understood as the mass of an electron as a result of their acceleration, dv_g/dt from an externally applied force F_{ext}, such as from an electric field.[14]

$$\mathbf{F}_{ext} = -m^* \frac{dv_g}{dT} \tag{1.13}$$

which can be rewritten as:

$$m^* = \frac{1}{\hbar^2} \nabla_k^2 E \tag{1.14}$$

m^* is dependent on the symmetry of the crystal. For example, in Si which has an ellipsoidal energy surface, the effective mass has two components, the longitudinal and the transverse.[15] The total effective mass is therefore written as $m^* = (m_l^* m_t^{*2})^{1/3}$. By combining equations (1.11) and (1.12) the carrier concentration can be expressed as:

$$n = N_C \frac{2}{\sqrt{\pi}} F_{1/2} \left[\frac{E - E_C}{k_B T} \right] \tag{1.15}$$

where $F_{1/2}$ is the Fermi integral with one-half index, which is used assuming a parabolic band.[13]

$$F_{1/2} = \int_0^\infty \frac{E^{1/2} dE}{1 + e^{\frac{E - E_F}{k_B T}}} \tag{1.16}$$

and N_C is defined as the effective density of states:[13]

$$N_C = 2 \left[\frac{2\pi m^* k_B T}{h^2} \right] g_C \tag{1.17}$$

For a non-degenerate semiconductor, where Boltzmann statistics are adequate in describ-

ing the population of electronic states $F_{1/2}$ approaches the value of $\sqrt{\pi}e^{\eta/2}$, where η is the reduced Fermi energy (E_F/k_BT). The carrier concentration can then be further simplified as:[11]

$$n = N_C e^{-\frac{E_C - E_F}{k_B T}} \tag{1.18}$$

These equations are similar for describing the transport in the valence band by holes (p-type). At temperatures greater than 0K electrons can be excited across the band gap into the conduction band, leaving a hole in the valence band. The law of mass action states that the number of holes and electrons will be equal in order to preserve charge neutrality, $n = p = n_i$.[15] The product of n and p at any temperature will therefore be a constant known as the intrinsic carrier concentration, n_i.

$$np = n_i^2 = N_C N_V e^{\frac{-E_{gap}}{k_B T}} \tag{1.19}$$

By rearranging equation (1.19) the Fermi energy with respect to the valence band edge can be explicitly calculated.[16]

$$E_F - E_V = \frac{1}{2}E_{gap} + \frac{k_B T}{2} ln\left[\frac{N_C}{N_V}\right] \tag{1.20}$$

Impurity atoms which are not isovalent to the host atom can contribute additional electrons (or holes) to the material, which can change the charge carrier concentration. For example, B atoms in Si contain one less electron and introduce an acceptor state (hole), while P atoms contain one extra electron and introduce a donor state (electron). The process of adding impurity atoms to change the carrier concentration is called doping. To preserve

neutrality the total negative charges (electrons and ionized acceptors) must equal the total positive charges (holes and ionized donors). In the case of n-type doping, $n = N_D^+ + p$, where the number of ionized donors is given by:[16]

$$N_D^+ = N_D \left[1 - \frac{1}{1 + \frac{1}{2} e^{\frac{E_D - E_F}{k_B T}}} \right] \tag{1.21}$$

At low temperature these impurities are said to be frozen-out, meaning there lacks sufficient energy to ionize all of the donors/acceptors. The carrier concentration in this regime depends on N_D, N_A, and the donor ionization energy E_D.[15]

$$n \approx \left[\frac{N_D - N_A}{2N_A} \right] N_C e^{\frac{-E_D}{2k_B T}} \tag{1.22}$$

As the temperature continues to increase, for a non-degenerate semiconductor, all of the impurities will become excited, but the energy necessary to excite electrons across the bandgap is not reached. This is called the extrinsic regime, and is marked by a carrier concentration independent of temperature. At sufficiently high temperature, the energy needed to excite carriers across the bandgap is reached; this is called the intrinsic regime and is marked by an equal number of holes and electrons ($n \approx p \gg N_D$). By combining the law of mass action for intrinsic semiconductors and the neutrality equation for extrinsic semiconductors the total carrier concentration in the intrinsic regime can be expressed as:

$$n = 1/2 \left[(N_D - N_A) + \sqrt{(N_D - N_A)^2 + 4n_i^2} \right] \tag{1.23}$$

The carrier concentration versus temperature for n-type Si ($N_D = 10^{15}$) can be seen in Figure 1.6, with the freeze-out, extrinsic, and intrinsic regimes labeled accordingly.[17]

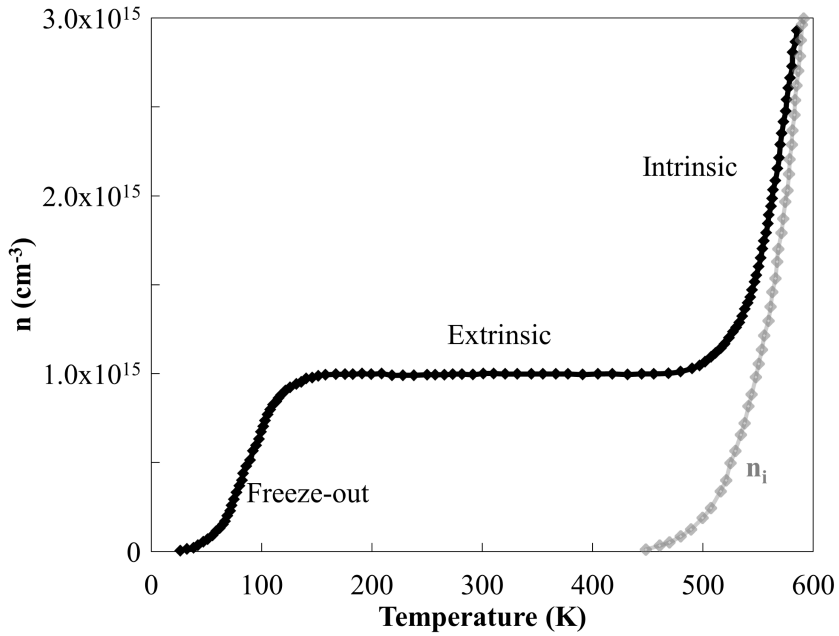

Figure 1.6: Carrier concentration versus temperature for n-type Si, ($N_D = 10^{15}$). The freeze-out, extrinsic, and intrinsic regimes can be clearly distinguished.[17]

In the case of a heavily-doped, or degenerate, semiconductor the above equations, which use Boltzmann statistics, are no longer valid; Fermi-Dirac statistics must be used. In this case the Fermi energy rests within 2 to $3k_BT$ of the conduction band minimum, or valence band maximum.[11] In this case σ decreases with temperature, as is observed in metals. Also the law of mass action, $np = n_i^2$ is no longer valid. In degenerate semiconductors the high level of impurities, donors or acceptors, are unable to become ionized, and n typically reaches a saturation value of approximately $10^{19} - 10^{20}\text{cm}^{-3}$.[12]

1.2.1.2 Mobility and Conductivity

The mobility of charge carriers in a crystal is given by equation (1.24),

$$\mu = \frac{e\bar{\tau}}{m^*} \tag{1.24}$$

where $\bar{\tau}$ is the scattering relaxation time. A number of processes affect the relaxation and therefore mobility, which has an effect on all the transport properties in a material. According to Matthiesen's rule, the total charge carrier mobility is the reciprocated sum of all the mobilities associated with various processes:[12]

$$\frac{1}{\mu} = \frac{1}{\mu_L} + \frac{1}{\mu_i} + \frac{1}{\mu_N} + \frac{1}{\mu_{def}} + \dots \tag{1.25}$$

and therefore the scattering relaxation rates also sum accordingly:

$$\frac{1}{\bar{\tau}} = \frac{1}{\tau_L} + \frac{1}{\tau_i} + \frac{1}{\tau_N} + \frac{1}{\tau_{def}} + \dots \tag{1.26}$$

where τ_L represents scattering by acoustic phonons, τ_i is the scattering from ionized impurities, τ_N is scattering from neutral impurities, and τ_{def} is scattering from defects such as dislocations, grain boundaries, vacancies, etc. Each scattering mechanism contributes varying degrees of magnitude and temperature dependencies based on the nature of the scattering center. Three of the most common, and which have the strongest temperature dependence are τ_L, τ_i, and τ_{def}. The scattering from point defects, for example, has a square root dependence on temperature.[18] The scattering associated with acoustic phonons is proportional to temperature as $\tau_L \propto T^{-3/2}$.[19] For the case of ionized impurity scattering the dependence on temperature is as follows, $\tau_i \propto T^{3/2}$.[20] In actual materials the isolation of a single scattering mechanism is rare, but rather the relaxation time contains multiple contributions. For most cases τ can be generally defined as:[16]

$$\tau(E) = \tau_o(T)(\epsilon^*)^{\lambda} \tag{1.27}$$

where ϵ^* is the reduced energy, $E - E_C/k_BT$, and λ is the scattering parameter, which is defined as $-1/2$, for acoustic phonon and point defect scattering, 0 for optical phonon scattering below the Debye temperature, and 3/2 for ionized impurity scattering. By considering only acoustic phonons and ionized impurities, the scattering relaxation time can be expressed as:[13]

$$\tau = \frac{\tau_{oL}(\epsilon^*)^{3/2}}{(\epsilon^*)^2 + (\frac{\tau_{oi}}{\tau_{oL}})^2} \tag{1.28}$$

The presence of neutral impurities and point defects affect the overall magnitude of the mobility, but acoustic scattering and ionized impurities cause the strongest temperature dependence. The charge carrier mobility versus temperature for GaAs can be seen in 1.24. The scattering from ionized impurities and acoustic phonons contributes to the overall mobility and cause a peak with increasing temperature.

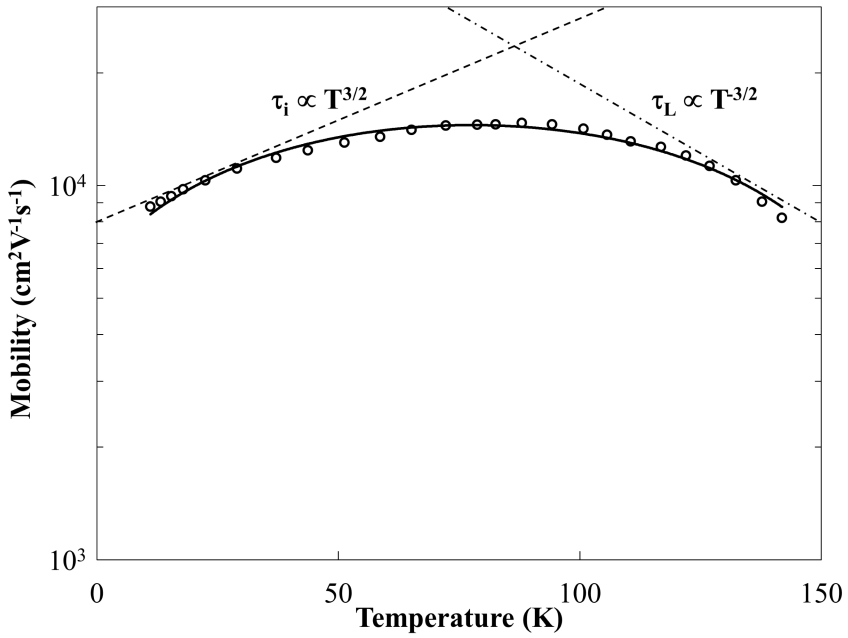

Figure 1.7: Electron mobility versus temperature for GaAs, with the temperature dependencies of ionized impurity and acoustic phonon scattering labeled.[17]

Ohm's law simply states that under the presence of an electric field, **E**, a current density, **J** will be produced which is proportional to the electrical conductivity of the material.[12]

$$\mathbf{J} = \sigma \mathbf{E} \tag{1.29}$$

By combining equation (1.29) and the Boltzmann transport equation for electrical conductivity, the current density can be fully expanded as:[16]

$$\mathbf{J} = \frac{e^2 \mathbf{E}}{3\pi^2 m^*} \int_0^\infty k^3 \tau(\mathbf{k}) \frac{\partial f_o}{\partial k} dk \tag{1.30}$$

More commonly however the electrical conductivity is written very generally as:

$$\sigma = ne\mu \tag{1.31}$$

In the case of an intrinsic semiconductor, electrons in the conduction band and holes in the valence band will both contribute to conduction:

$$\sigma = q(n\mu_n + p\mu_p) \tag{1.32}$$

where μ_n and μ_p are the electron and hole mobilities, respectively. The magnitude and temperature dependence of electrical conductivity varies by the specific material. For example, in metals and degenerate semiconductors the electrical conductivity decreases with temperature, while, generally for extrinsic semiconductors, the electrical conductivity will follow a trend very close to the carrier concentration as a function of temperature. The magnitude of the electrical conductivity spans multiple orders of magnitude, with metals such as copper on the order of $10^7 \Omega^{-1}\mathrm{m}^{-1}$ and fused quartz on the order of $10^{-18} \Omega^{-1}\mathrm{m}^{-1}$.[21, 22]

1.2.2 Seebeck Coefficient

The Seebeck effect is at the crux of thermoelectric materials. At its most essential, it is defined as the ratio of the voltage generated by a given temperature difference for a specific material. The following section will give a more detailed explanation of the Seebeck effect in various materials.

If a material, in an open circuit, is placed under a temperature gradient, ∇T, the charge carriers will diffuse from hot to cold. The driving force of the temperature gradient is compensated by an established electric field, $\mathbf{E}$, which arises from the gradient of electrons across the material. The ratio of the electric field to the temperature gradient is the material specific Seebeck coefficient, $S = \mathbf{E}/\nabla T$.[23] A dramatized schematic of this effect can be seen in 3.14.

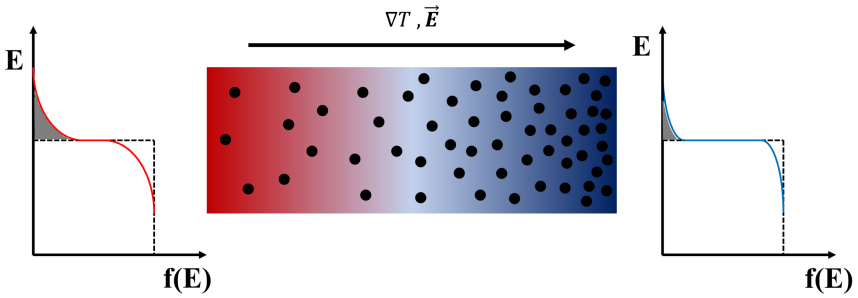

Figure 1.8: Seebeck effect in a single conductor. The Seebeck coefficient is defined as the ratio of the electric field established, $\mathbf{E}$, in the presence of a temperature gradient, ∇T.

The magnitude of the Seebeck coefficient can vary from a few μVK^{-1} for metals to as high as $40000 \mu VK^{-1}$ for insulators such as $FeSb_2$.[24, 25] The Seebeck coefficient can be thought of as the amount of entropy per carrier ($S \approx C/e$, where C is the specific heat).[26] For a classical electron gas with average energy $3/2k_BT$, $S \approx k_B/e \approx 87 \mu VK^{-1}$. For metals

the relationship can be approximated as follows:

$$S \approx \left(\frac{k_B}{e}\right)\frac{k_B T}{E_F} \tag{1.33}$$

These equations give a qualitative understanding of the Seebeck effect, but to understand it for non-degenerate and degenerate semiconductors, which are crucial for thermoelectric applications, a more general expression must be derived. For materials with parabolic bands and charge carrier scattering which can be assigned to a simple relaxation time approximation ($\tau \approx E^{\lambda}$) the Seebeck coefficient can be expressed as:[16]

$$S = -\frac{k_B}{e}\left[\frac{\int_0^{\infty} \epsilon^{*(5/2+\lambda)} + \lambda\frac{\partial f_o}{\partial \epsilon^*} d\epsilon^*}{\int_0^{\infty} \epsilon^{(*3/2+\lambda)} + \lambda\frac{\partial f_o}{\partial \epsilon^*} d\epsilon^*} - \eta\right] \tag{1.34}$$

where λ defines the energy dependence of the scattering relaxation time, ϵ^* is the reduced energy, and η is the reduced Fermi energy. Equation (1.34) can be further reduced to the form which includes Fermi integrals, similar to the case of carrier concentration:

$$S = \mp\frac{k_B}{e}\left[\frac{(5/2+\lambda)F_{3/2+\lambda}(\eta)}{(3/2+\lambda)F_{1/2+\lambda}(\eta)} - \eta\right] \tag{1.35}$$

This equation represents the generalized description of the Seebeck coefficient where Fermi-Dirac statistics are necessary. In the case of a classical non-degenerate semiconductor, equation (1.35) can be greatly reduced.[11]

$$S = \mp\frac{k_B}{e}\left[\frac{5}{2} + \lambda - \eta\right] \tag{1.36}$$

where the negative sign applies to n-type materials and the positive sign applies to p-type materials. At high temperature $\lambda = 1/2$ for optical phonon scattering and 3/2 for ionized

impurity scattering.[20] It should be noted that in the case of non-covalent materials such as ionic crystals, the relaxation time approximation is not applicable.[27] Figure 1.9 shows Seebeck, S versus the reduced Fermi energy, η for the classical treatment (equation (1.36)) and Fermi-Dirac statistics (equation (1.35)). As η goes beyond a value of -2 the difference in Seebeck coefficient between the classical and quantum treatments become appreciable; the classical statistics are therefore no longer valid.

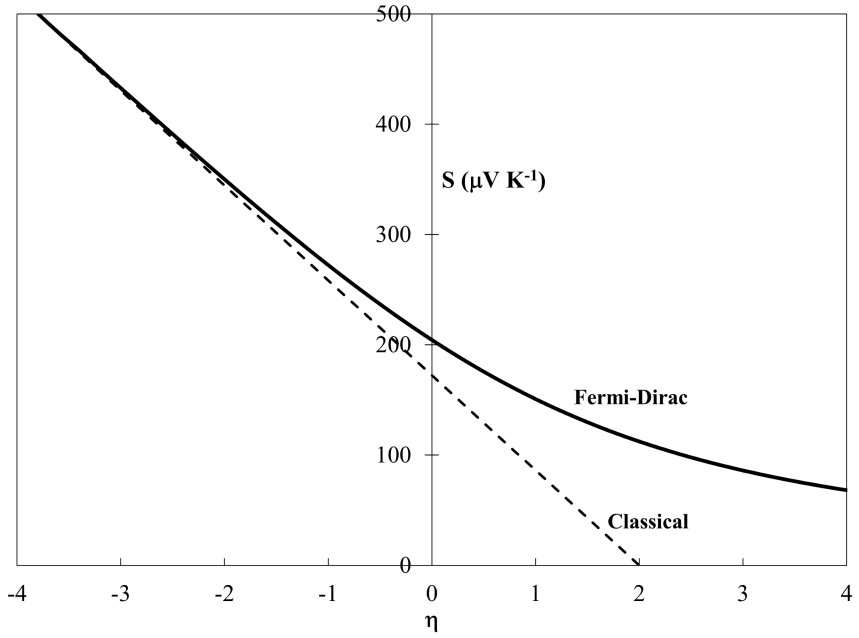

Figure 1.9: Seebeck coefficient versus η, the reduced Fermi energy (E_F/k_BT) using Fermi-Dirac and classical statistics. Notice that at around $\eta = -2$ the values of Seebeck for the two treatments begin to diverge. As η approaches a value of 2, the classical treatment predicts a Seebeck value of 0.

In the case of mixed conduction, such as in intrinsic semiconductors and past the intrinsic temperature of extrinsic semiconductors, the Seebeck coefficient is affected by the electronic and hole contributions (equation (1.37)).

$$S \approx \frac{S_e\sigma_e + S_p\sigma_p}{\sigma_e + \sigma_p} \tag{1.37}$$

If $n = p$, equation(1.37) can be reduced to:

$$S \approx \frac{S_e \mu_e + S_p \mu_p}{\mu_e + \mu_p} \tag{1.38}$$

Since the signs of the Seebeck coefficient for n-type and p-type materials are negative and positive, respectively, mixed conduction where the mobilities for electrons and holes are similar will result in very low values. The conclusion is that a single carrier type is ideal for optimizing Seebeck coefficient. Figure 1.10 is the Seebeck coefficient versus temperature for PbTe doped with monovalent Na at 0.1 and 1.0%. As the amount of dopant is increased the overall magnitude of the Seebeck coefficient is decreased due to the increased carrier concentration, but the decrease due to mixed conduction occurs at a higher temperature. Because the hole concentration is higher in 1% Na doped PbTe, a higher number of electrons is needed to offset the p-type Seebeck coefficient.

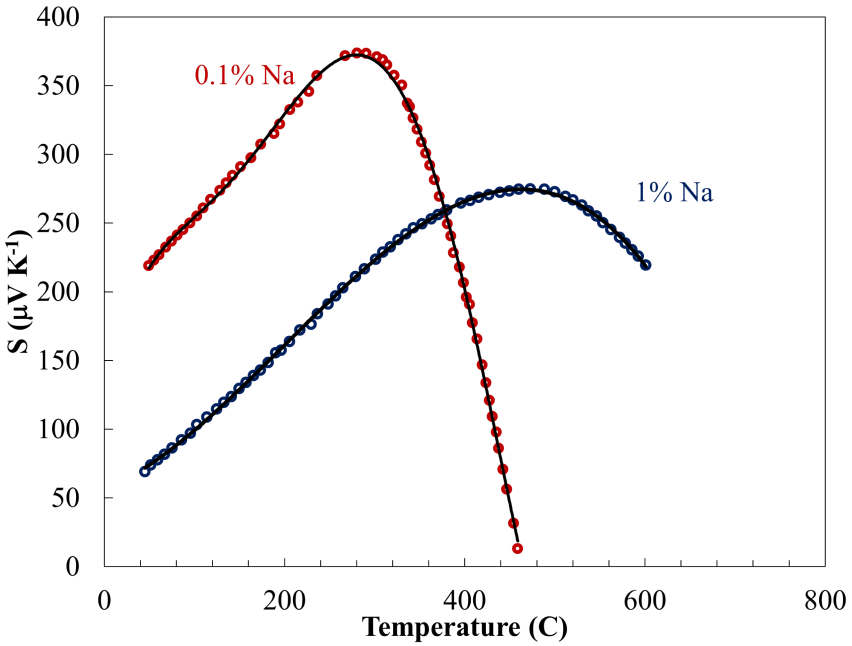

Figure 1.10: Seebeck coefficient versus temperature for 0.1 and 1.0% Na doped PbTe. Note that the peak in Seebeck coefficient due to intrinsic excitation of carrier across the bandgap happens at a higher temperature since the number of holes is greater in 1%Na-PbTe and therefore a higher concentration of excited electrons is needed to compensate.[28]

In the case of strong degeneracy in a semiconductor ($\eta \geq -2$), the Seebeck coefficient can be expressed as:[11]

$$S = \mp \frac{\pi^2}{3} \frac{k_B}{e} \frac{(3/2 + \lambda)}{\eta} \tag{1.39}$$

Equation (1.39) can be further simplified under the assumption that the relaxation time, τ is energy independent as:[29]

$$S = \frac{2k_B^2}{3e\hbar^2} m^* T \left(\frac{\pi}{3n}\right)^{2/3} \tag{1.40}$$

Equation (1.40) reveals two important qualities about the Seebeck coefficient: 1. S is directly proportional to m^*, which implies that a band structure with wide flat bands will yield a high S value; 2. S is inversely proportional to n and therefore implies an optimization

of S^2n, which contributes to the power factor ($S^2\sigma$) and the overall ZT. Goldsmid predicted that the optimization of S^2n happens around $0 \leq \eta \leq 1$, which is a heavily doped or degenerate semiconductor.[11]

1.2.3 Thermal Transport

The heat flow in an isotropic material obeys the relation originally formulated by Fourier:[30]

$$\mathbf{Q} = -\kappa \nabla T \tag{1.41}$$

where $\mathbf{Q}$ is the heat flux density (Wm^{-2}), κ is the thermal conducivity ($\mathrm{Wm}^{-1}\mathrm{K}^{-1}$), and ∇T is the temperature gradient (Km^{-1}). The process of heat conduction is a diffusive process, meaning that thermal energy propagates through a material by enduring frequent collisions caused by scattering sites, such as defects, lattice atoms, impurities, electrons, etc. The magnitude of thermal conductivity values fluctuate less for different materials than say electrical conductivity, with maximums ranging from 1000 to 20000$\mathrm{Wm}^{-1}\mathrm{K}^{-1}$ for metals and non metals at room temperature.[31]

Heat is predominantly conducted through materials by electrons and quantized lattice vibrations, called phonons, however other mechanisms of heat conduction have been shown to exist by diffusion of electron-hole pairs[32], diffusion of excitons[33], and transport of photons[34]. These mechanisms are not pertinent to this work and will not be discussed. The total thermal conductivity can therefore be defined as the summation of the electronic and lattice contributions, $\kappa = \kappa_e + \kappa_L$. The following sections will further outline the theory and importance behind both contributions.

1.2.3.1 Electronic Thermal Conductivity

Electrons, in addition to charge, can act as conductors for heat through a material. Metals such as copper and silver have relatively high thermal conductivity values, which can be traced to their high electrical conductivity. Recall that the electrical conductivity can be expressed as $\sigma = ne\mu$, or more fully as:

$$\sigma = \frac{ne^2 l}{2m_e v} \tag{1.42}$$

where, n is the electron concentration, l is the electron mean free path, m_e is the electron mass, and v is the average thermal velocity (the scattering relaxation time, which was used in the previous section can be defined as $\tau = l/v$). In a classical treatment the electrons behave as a kinetic gas, and the thermal conductivity is therefore expressed as:[31]

$$\kappa = \frac{1}{3} n c_e v l \tag{1.43}$$

where c_e is the heat capacity per electron. The electronic contribution to heat capacity is defined as $C_e = nc_e$. The Wiedemann-Franz law, a ratio of thermal conductivity to electrical conductivity, can be expressed using equations (1.42) and (1.43).

$$\frac{\kappa}{\sigma} = \frac{2}{3} \frac{m_e v^2 c_e}{e^2} \tag{1.44}$$

By using a quantum statistical treatment, c_e fully expressed is proportional to T, and v is considered constant, so that equation (1.44) becomes:[31]

$$\frac{\kappa}{\sigma} = \frac{\pi^2}{3} \left(\frac{k_B}{e} \right)^2 T \tag{1.45}$$

Equation (1.45) is defined as the Wiedemann-Franz-Lorenz law and shows the ratio of thermal to electrical conductivity. At a given absolute temperature $\kappa/\sigma T$ is a constant. The constant is known as the ideal Lorenz number and is $2.45x10^{-8}\mathrm{W\Omega K^{-2}}$. Most often however there is disagreement between the experimental values of Lorenz number for metals and the ideal value, most notably in the intermediate temperature range, where assuming a classical treatment is invalid. In actuality, the Lorenz number L_o is governed by the way the electron scattering time depends on the electron velocity and can take on a range of values from $(1-4)*10^{-8}\mathrm{W\Omega K^{-2}}$.[14] In a non-degenerate semiconductor, where Boltzmann statistics are applicable and assuming a simple energy dependence for the scattering relaxation time ($\tau = \tau_o E^{\lambda}$), the Lorenz number can be expressed as:[31]

$$L_o = \left(\frac{k_B}{e}\right)^2 (5/2+\lambda) \tag{1.46}$$

where λ determines the energy dependence of the relaxation time. It should be noted that for most semiconductors, unless heavily doped, the electronic contribution to thermal conductivity is negligible compared to the lattice thermal conductivity. For example, in the case of silicon, the electronic contribution at high temperature contributes approximately 5% to the overall thermal conductivity. In the case of a heavily doped, or degenerate semiconductor, where Fermi-Dirac statistics are necessary, the Lorenz number is given in terms of the energy dependence of the scattering relaxation time (λ) and Fermi integrals ($F_{\lambda+s}(\eta)$):[11]

$$L = (k_B/e)^2 \left[\frac{(\lambda+7/2)F_{\lambda+5/2}(\eta)}{(\lambda+3/2)F_{\lambda+1/2}(\eta)} - \left[\frac{(\lambda+5/2)F_{\lambda+3/2}(\eta)}{(\lambda+3/2)F_{\lambda+1/2}(\eta)}\right]^2\right] \tag{1.47}$$

For a more complete understanding of thermal transport in materials, especially in semiconductors, an understanding of the lattice contribution to thermal conductivity is essential.

1.2.3.2 Lattice Thermal Conductivity

For non-metals and materials with a low electronic thermal conductivity relative to the total thermal conductivity the lattice contribution to thermal conductivity is the dominant mechanism of thermal transport. The propagation of heat via lattice atoms is done through the diffusion of phonons. Phonons are quantized modes of vibration for a given lattice of atoms. By assuming the atomic bonds are approximated as spring-like forces the energy states for phonons are quantized, as for a quantum harmonic oscillator ($E = \hbar\omega(n+1/2)$).[35] For a monoatomic, linear chain of atoms with mass M, held together with harmonic forces that have a spring constant of k, and separated by a distance a, the frequency as a function of wavenumber, q can be expressed as:[31]

$$\omega(q) = 2\sqrt{k/M}|sin(qa/2)| \tag{1.48}$$

This relation is called the dispersion curve, and ranges from $\pm\pi/a$, which is termed the Brillouin zone, as can be seen in Figure 1.11(a).[12] The dispersion curve for a monoatomic chain is called the acoustic branch. Notice as the curve approaches the Brillouin zone edge the group velocity ($v_g = d\omega/dq$) approaches zero. For a similar linear chain where there are two atomic species with different masses the creation of a second higher frequency branch call the optic branch appears, as seen in Figure 1.11(b). The optic branch has low group velocity, and therefore generally does not contribute to heat conduction.

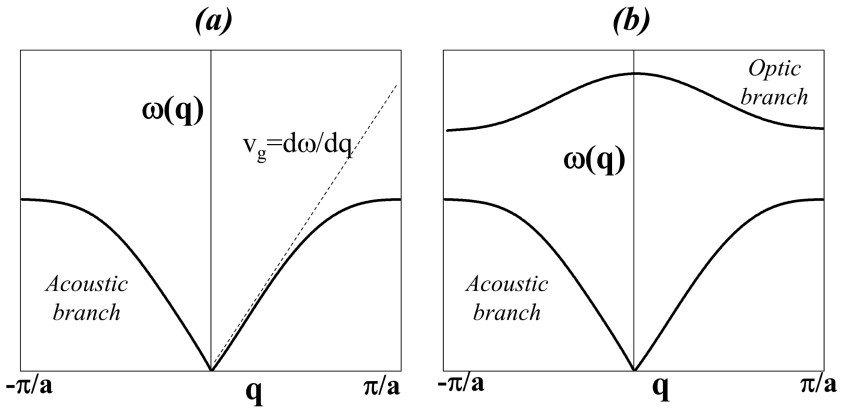

Figure 1.11: (a) Model of phonon dispersion curve for a one-dimensional monoatomic lattice, with equal masses and atomic spacing a. The result is a single acoustic branch. (b) Phonon dispersion curve for one-dimensional diatomic lattice (unequal masses). The creation of the higher frequency, low group velocity optic branch is a result of of the two atomic species with unequal masses.

In the case of a real crystal, which is 3-dimensional, the dispersion curves seen in Figure 1.11 are oversimplified. For the general case of N types of atoms there will exist three acoustic branches, one longitudinal and two transverse, and $3(N-1)$ optic branches.

The total heat current in a material contributed by all phonon modes is expressed as:[31]

$$\mathbf{h} = \Sigma N(q)\hbar\omega\mathbf{v}_g(q) \tag{1.49}$$

where $N(q)$ is the number of phonons with mode q. This distribution is determined from Bose-Einstein statistics, since phonons may be treated as bosons. The thermal conductivity is then found by dividing the heat current by the temperature gradient along a material. By further adopting some of the simplifying assumptions of the Debye model, i.e. a linear dispersion relation for all branches, and equal group velocities among acoustic branches, the Boltzmann transport equation for thermal conductivity can be expressed as:[31]

$$\kappa = \frac{1}{3} v \int l(x) C(x) dx \tag{1.50}$$

where $x = \hbar\omega / k_B T$, $l(x)$ is the phonon mean free path, and $C(x)dx$ is the differential contribution to the heat capacity (in the Debye approximation). For the simplistic volume averaged case, developed by Debye, equation (1.50) can be further simplified and expressed as:

$$\kappa = \frac{1}{3} C v l \tag{1.51}$$

It is typical to describe the potential energy of the bonds in a crystal as harmonic. If this assumption was true the phonons propagating through a defect-free crystal would experience no interactions and the thermal conductivity would tend to infinity. However, even ideal single crystals have finite thermal conductivity in reality. To understand why there is inherent phonon resistance in all crystals it is vital to understand that the potential energy of the atomic bonds is not quadratic. The anharmonic displacement of atoms caused by a phonon will therefore interact with other phonons. The interaction probability for a three phonon process, two initial phonons of wave vectors, $\mathbf{q}_1$ and $\mathbf{q}_2$, and a final phonon, $\mathbf{q}_3$ can be simply written as:[31]

$$\mathbf{q}_1 + \mathbf{q}_2 = \mathbf{q}_3 + \mathbf{g} \tag{1.52}$$

where $\mathbf{g}$ is a reciprocal lattice vector. If the interaction of $\mathbf{q}_1$ and $\mathbf{q}_2$ results in a mode $\mathbf{q}_3$ which lies within the Brillouin zone, $\mathbf{g} = 0$. These interactions are called Normal processes.[36] When $\mathbf{q}_1$ and $\mathbf{q}_2$ sum to a value which is outside the Brillouin zone,

g is equivalent to the reciprocal lattice ($\pm 2\pi/a$). Adding or subtracting **g** then folds the resulting phonon mode back into the Brillouin zone. This process is called Umklapp scattering and reverses the direction of the phonon flux thereby adding resistance to the heat flow.[37] Umklapp processes give rise to thermal resistance, while normal processes do not and can be effectively ignored when determining thermal conductivity. At sufficiently high temperatures, $\hbar\omega/k_BT$ becomes small for all phonon modes and the probability of Umklapp processes taking place increases. The lattice thermal conductivity due to the anharmonic Umklapp scattering can be expressed as:[38]

$$\kappa_L = A\frac{M_a a \theta_D^3}{N^{\frac{2}{3}} T \gamma^2} \tag{1.53}$$

where A is a material specific proportionality constant, N is the number of atoms per unit cell, M_a is the atomic mass, a^3 is the volume per atom, θ_D is the Debye temperature, and γ is the Grüneisen parameter. The Grüneisen parameter is defined as the rate of change of frequency of mode i with the volume of the crystal ($\gamma_i = -\partial ln\omega_i/\partial lnV$). The Grüneisen parameter is essentially a measure of the anharmonic nature of the bond energy in a material and is directly related to the thermal expansion coefficient.[31] It is clear to see from equation (1.53) that the lattice thermal conductivity at temperatures above the Debye temperature goes as $1/T$ with temperature.

At low temperature phonon-phonon scattering processes become less prominent. In this temperature regime crystal/grain boundaries and defects become the dominant scattering event for phonons. The lattice thermal conductivity associated with phonon scattering at grain boundaries or crystal boundaries can be expressed as:[14]

$$\kappa_{boundaries} = \frac{LT^3}{C} \tag{1.54}$$

where L is the linear size of the boundaries and C is a materials specific constant. The thermal conductivity associated with defect scattering is dependent on the number of defects/impurities (N) in the crystal:[14]

$$\kappa_{defects} = (BNT^p)^{-1} \tag{1.55}$$

where B is a materials specific constant, and $p < 1$. All of the various scattering mechanisms for thermal conductivity sum according to Matthiesen's rule, similar to that for electrical conductivity.

$$\frac{1}{\kappa_L} = \frac{1}{\kappa_{anharmonic}} + \frac{1}{\kappa_{boundary}} + \frac{1}{\kappa_{defects}} \tag{1.56}$$

The temperature dependence of thermal conductivity is determined by many factors, including the bonding nature in a material, the degree of crystallinity, the specific temperature regime relative to the Debye temperature, and unit cell size to name a few. The thermal conductivity as a function of temperature for sapphire (crystalline Al_2O_3) can be seen in Figure 1.12.[12, 39]

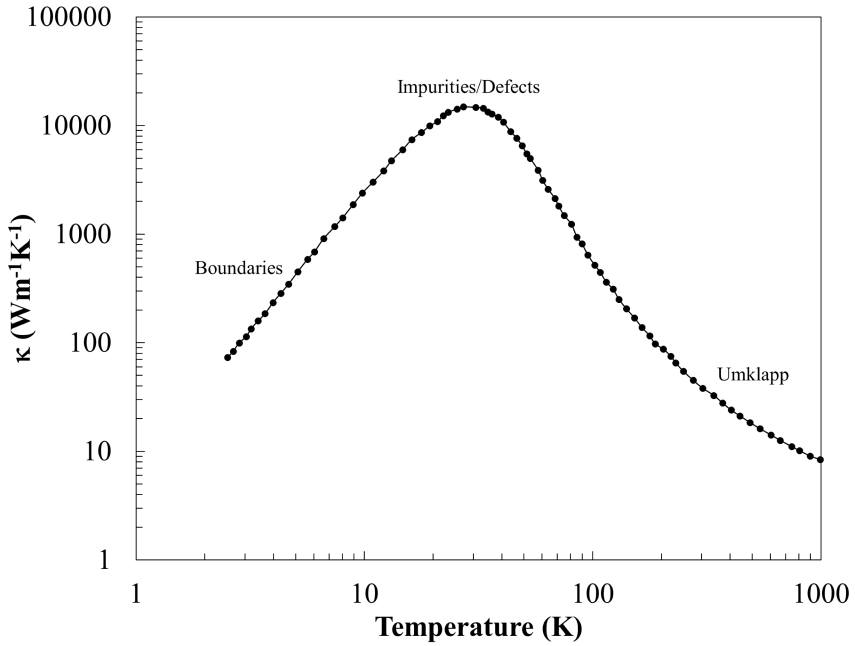

Figure 1.12: Thermal conductivity as a function of temperature for sapphire. The scattering events which are dominant in their temperature regime are labeled: boundary scattering at low temperature, defect scattering in mid temperature range, and anharmonic phonon-phonon (Umklapp) scattering at high temperature.[12]

1.2.4 ZT and Methods of Enhancement

The majority of today's state of the art thermoelectric materials exhibit peak ZT values around unity or slightly higher. The low efficiency and often expensive manufacturing of these compounds are to blame for thier lack of commercial use. Specific examples include compounds such as PbTe and $AgSbTe_2$-GeTe alloys, which have ZT approaching 2, but which are brittle, not cost-effective and contain toxic elements.[40, 28] Oxide-based thermoelectrics such as BiCuSeO and $SrTiO_3$ are stable at high temperature, but lack sufficiently high ZT values.[41, 42] Materials based on the Skutterudite mineral, $CoSb_3$, have been extensively researched and are now being integrated into radioisotope thermoelectric generators for power generation applications in deep space voyages.[43, 44] Cu-based compounds have garnered much attention recently because of their low cost and low thermal conductivity and

have been shown to yield ZT values near unity.[45, 46, 47]

The low efficiency of thermoelectric materials, as aforementioned, can be traced to the contraindicated properties of the dimensionless figure of merit, ZT. In terms of the Seebeck coefficient, S, the electrical conductivity, σ, thermal conductivity, κ, and the absolute temperature, T, ZT is expressed as:

$$ZT = \frac{S^2\sigma}{\kappa}T \tag{1.57}$$

By substituting the one carrier approximation for electrical conductivity ($\sigma = ne\mu$) ZT can be further expressed as:

$$ZT = eT(S^2n)\frac{\mu}{\kappa} \tag{1.58}$$

Equation (1.58) more clearly displays the contraindicated nature of ZT. The Seebeck coefficient is, in general, inversely proportional to the carrier concentration, while the electrical conductivity is directly proportional. There is an optimization point for S^2n as a function of carrier concentration. Also, the ratio of mobility, μ to the thermal conductivity, κ is directly contradictory. Increasing the number of scattering centers in a crystal will lower the thermal conductivity, but also lower the mobility. Using a single parabolic band model the optimization of power factor and ZT as a function of charge carrier concentration can be seen in Figure 1.13. For insulators ($\leq 10^{18}\text{cm}^{-3}$) the electrical conductivity is too low, while for metallic materials ($\geq 10^{22}\text{cm}^{-3}$) the Seebeck coefficient is too low. Power factor is optimized for a heavily doped or degenerate semiconductor.

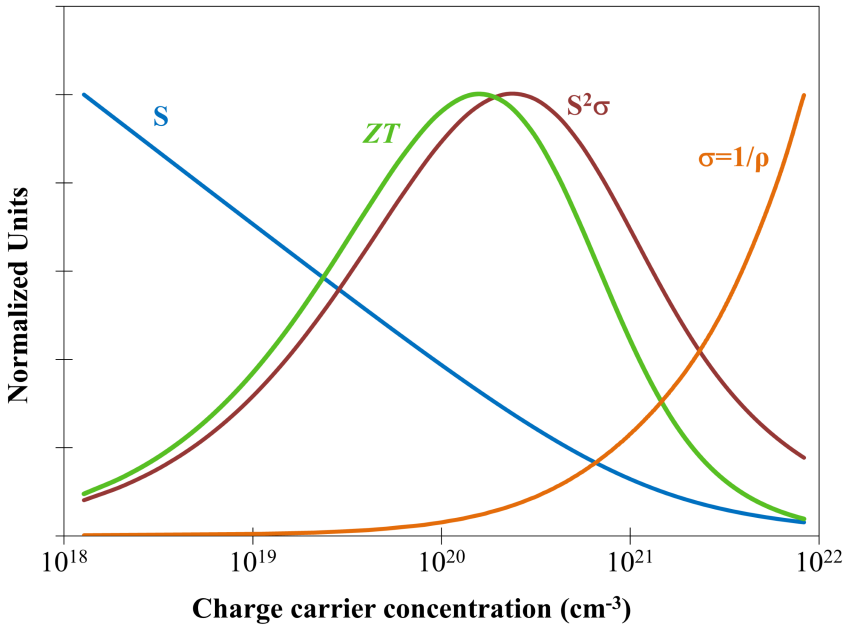

Figure 1.13: Seebeck coefficient (S), electrical conductivity (σ), power factor ($S^2\sigma$), and ZT fo an arbitrary thermoelectric material. Optimization of power factor and ZT are done at relatively high charge carrier concentrations of approximately $10^{19} - 10^{20}\text{cm}^{-3}$, which corresponds to heavily doped, or degenerate, semiconductors.

Adjusting the carrier concentration in a semiconductor is an effective means of optimizing thermoelectric performance. Because the electronic thermal conductivity is tied to the electrical conductivity, lowering the lattice contribution has been shown to be an effective means of increasing overall ZT for a number of materials as well.[48] The following sections will give an outline of the various theoretical and experimental techniques used in the field to enhance the power factor and decrease the thermal conductivity of thermoelectric materials.

1.2.4.1 Optimizing Power Factor

One of the most routine methods for enhancing and optimizing the power factor in thermoelectrics is through doping. By adding foreign atoms which contribute one less (p-type) or one extra (n-type) electron than the host atoms, the charge carrier concentration in a semiconductor can be controlled. Many of the properties and equations associated with doping

to tune carrier concentration were explained in previous sections.

In 1993 Hicks and Dresselhaus published work outlining the possibility of enhancing the Seebeck coefficient of materials by manipulating the density of states.[49] The idea can be explained by examining the Mott equation of the Seebeck coefficient for metals which is expressed as:

$$S = \frac{\pi^2 k_B^2 T}{3e} \frac{1}{\sigma(E)} \left[\frac{d\sigma(E)}{dE} \right]_{E=Ef} \tag{1.59}$$

By then substituting the differential energy form of electrical conductivity, equation (1.59) can be expressed as:

$$S = \frac{\pi^2 k_B^2 T}{3e} \left[\frac{1}{g(E)} \frac{dg(E)}{dE} + \frac{1}{\tau(E)} \frac{d\tau(E)}{dE} + \frac{2}{v(E)} \frac{dv(E)}{dE} \right]_{E=Ef} \tag{1.60}$$

where $g(E)$ is the electronic density of states, $\tau(E)$ is the electron relaxation time, and $v(E)$ is the electron velocity. It is clear to see from equation (1.60) that a sharp increase in the density of states at the Fermi energy is beneficial for the Seebeck coefficient. Recall however that the typical density of states for a bulk material has a square root dependence on the energy. Hicks and Dresselhaus showed that by reducing the dimensionality of a material the density of states as a function of energy could be fundamentally altered. Specifically, for 2D quantum wells, 1D nanowires, and 0D quantum dots, there exists discontinuities at quantized energy levels in the density of states. In theory these nanostructures could be endotaxially incorporated into bulk materials, meaning an alignment of the lattice parameters. This would allow uninhibited electron transport and altered density of states, and ultimately, and increased Seebeck coefficient. The proof of concept demonstration was initially reported using PbTe/$Pb_{1-x}Eu_x$Te quantum well superlattices synthesized by molec-

ular beam epitaxy.[50, 51] Unfortunately, due to the complicated and intricate synthesis of lower dimensional nanostructures, little experimental work beyond this has been reported.

Engineering the band structure is another method towards enhancing power factor. Specifically engineering degeneracy into the band structure increases the effective density of states and has been shown to increase electrical conductivity and Seebeck coefficient.[52] This situation can take place when either multiple band extrema overlap at essentially the same energy (within a few k_BT) or multiple carrier pockets exist within the Brillouin zone due to crystal symmetry.[53] Many of today's state of the art thermoelectric materials have been shown to exhibit band degeneracy, for example Bi_2Te_3[54], PbTe[53], $CoSb_3$[55], and SnSe[56].

Aside from doping, the examples provided above can be complicated and expensive to carry out. Much of the success in thermoelectrics engineering has been achieved through lowering the lattice thermal conductivity. Some of these principles will be discussed in the next section.

1.2.4.2 Achieving Low Thermal Conductivity

In 1956 Ioffe first suggested that optimizing the ratio of mobility to lattice thermal conductivity would be an effective route to optimizing ZT.[57] Point defects, defined as defects which are much smaller than the phonon wavelength, scatter phonons and can lower lattice thermal conductivity. The classification of point defects can include atomic substitutions, vacancies, and interstitial atoms. For substitutional atoms which have the same valence configuration as the host atom, and differ only by mass, a simple perturbation theory can

be used to express the scattering rate as:[58]

$$\frac{1}{\tau_{\Delta M}} = \frac{c_p a^3 \omega^4}{4\pi v^3} \left[\frac{\Delta M}{M}\right]^2 \tag{1.61}$$

where c_p is the ratio of the number of point defects to the number of lattice sites, a^3 is the average volume per atom, ω is the phonon frequency, and v is the phonon group velocity. It should be noted that the scattering rate associated with mass fluctuation point defects is independent of temperature and quadratically dependent on the mass difference between the host and substituted atom. The thermal conductivity versus mol fraction InAs for a GaAs-InAs solid solution can be seen in Figure 1.14; a reduction in thermal conductivity of nearly an order of magnitude was achieved.

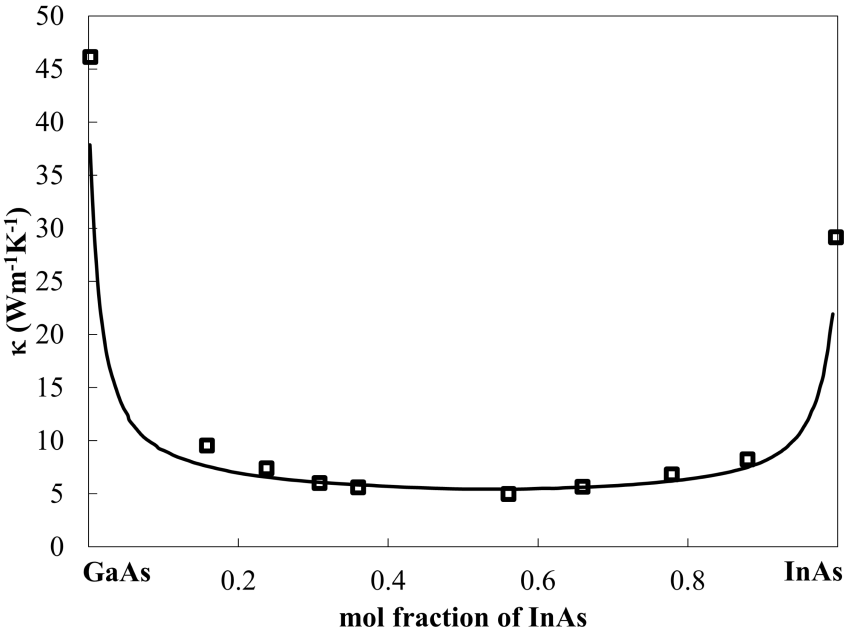

Figure 1.14: Thermal conductivity versus mol fraction of InAs in GaAs.[59]

In the early 1990s Slack proposed that good thermoelectric materials would, in general, have a large unit cell, heavy constituent atoms, and high carrier mobilities.[60] These se-

lection rules outline what is called the phonon-glass electron-crystal (PGEC) approach to materials selection.[61] In this model the ideal thermoelectric material would exhibit electronic mobility akin to a single crystal, but have poor thermal properties, like a glass. One of the first demonstrations of this concept was in the use of Ge-based clathrate materials.[62] Clathrates have cage-like structures and have been shown to exhibit minimum thermal conductivity values while maintaining high carrier mobility. The Skutterudite compound, generally written as MX_3, where M represents a metal atom and X a pnictide atom, crystallizes in a large cubic structure with high carrier mobilities.[63] To minimize the thermal conductivity rare earth atoms such as Ce, Yb, and La are substituted into the interstitial sites of the Skutterudite unit cell.[43] These rare earth atoms are called filler atoms, or rattlers, and are so named because of the specific frequency mode at which they rattle. This vibrational mode then scatters phonons and greatly lowers thermal conductivity.[64] The mineral based compound, tetrahedrite ($Cu_{12}Sb_4S_{13}$) has recently garnered attention. The material exhibits attractive thermoelectric properties, with high levels of anharmonicity and a large unit cell, all of which lead to minimized thermal conductivity.[65] Recently, it was shown through experimental and computational techniques that the some of the Cu atoms, which have lone-pair electrons, resonate like a rattler atom, thus classifying it as a PGEC material.[66]

In 2012, Biswas *et al* used hierarchical structuring in Na-doped PbTe to achieve record high ZT values.[67] They achieved multi-scaled phonon scattering through alloying, nanostructured precipitation, and grain size reduction. Since the total lattice thermal conductivity is a sum of the phonon relaxation rates related to various scattering mechanisms, using a myriad of defects to scatter phonons across multiple wavelengths can help minimize the lattice thermal conductivity. It should be noted however that the synthesis associated with these materials is timely and expensive, and so commercial applicability is limited. In the

following work alloys and compounds based on Ge-Sb-Te phase change materials were synthesized and characterized. A more in-depth discussion of these materials is presented in chapter 3.

Chapter 2

Background: Phase Change Materials

In 1965 Gordon Moore postulated that the number of transistors per square inch on integrated circuits would double every year, which has been shown to correlate well with the growth of computers.[68] To maintain this trend the size of the modern transistor is now within the range of non-negligible quantum effects, such as electron tunneling. An alternative area of improving computer performance is memory. Today the primary memory storage devices in computers are based on random access memory (RAM). RAM technologies have inherent downsides such as volatility and the necessity of relatively large magnetic fields. Phase change memory is the next generation of memory technology now being implemented in some of the new memory designs of companies such as Intel.[69]

Though Stanford Ovshinsky is generally credited with developing phase change materials for memory applications, it was Alan Waterman in the early 1900s who originally discovered the resistive switching character of MoS_2. Waterman discovered that with the application of electrical heating MoS_2 would undergo multiple resistive states, namely α: the high resistance state and β: the low resistance state. These resistive states were both stable and reversible upon thermal or photonic switching.[70] In 1968 Ovshinsky reported on the electrically controlled threshold switching of Si-Ge-As-Te compounds while also outlining the utilization of other chalcogenide alloys for use in memory devices which exploit this switching

effect.[71] Based on the pioneering work of Ovshinsky, phase change materials can now be found in nonvolatile and rewriteable applications such as CD's, DVD's, and Blu-Ray discs. In the following section an explanation of the function and nature of these memory devices, crystal structure, and applicability in thermoelectrics will be presented.

2.1 Phase Change Memory

Dynamic random access memory (DRAM) and static random access memory (SRAM) have natural drawbacks when compared with today's state-of-the-art memory storage alternatives. DRAM and SRAM can currently be used for approximately 100,000 rewrite cycles before degrading and are volatile, which means data is stored only while power is supplied. Non-volatile phase change memory (PCM) operates on the same principle as CDs and DVDs, but utilizes the swinging electrical properties rather than optical properties. In a typical PCM device, as is illustrated in Figure 2.1, a large, high-intensity electrical (or laser pulse) is used to reset a local area of phase change material to the amorphous phase. This amorphous phase is of a high resistance state, while the crystalline state is of low resistance. To set the state, a slightly longer duration, low-intensity electrical (or laser pulse) is applied to the phase change material allowing for crystallization. This crystallization happens on extremely small time-scales (approximately 100s of nanoseconds). Operational devices using a similar setup to that seen in Figure 2.1 have been demonstrated by companies such as Samsung, Intel, and IBM.[69, 72, 73] The unique ability of phase change materials to quickly alternate between the crystalline and amorphous phases, while also demonstrating high stability and structural integrity is a large requirement. The majority of today's state of the art phase change memory alloys can be traced to the binary tie-line of GeTe and Sb_2Te_3, as can be

seen in Figure 2.2.

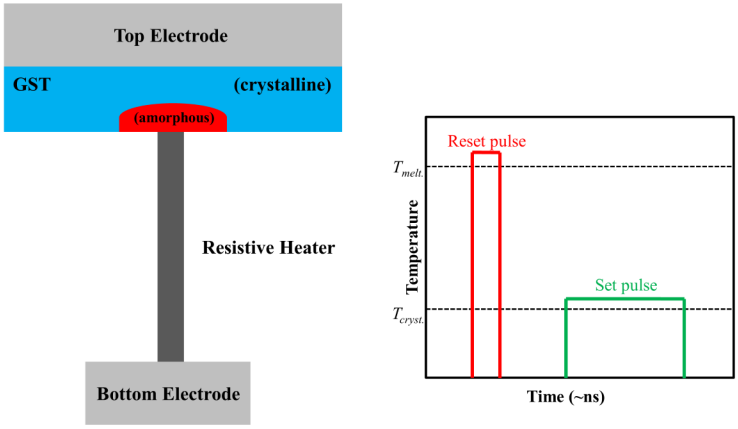

Figure 2.1: Schematic of memory unit using phase change materials where the high resistance state (reset state) is activated with a short, high intensity electrical pulse and the low resistance state (set state) is activated with a long, low intensity electrical pulse.

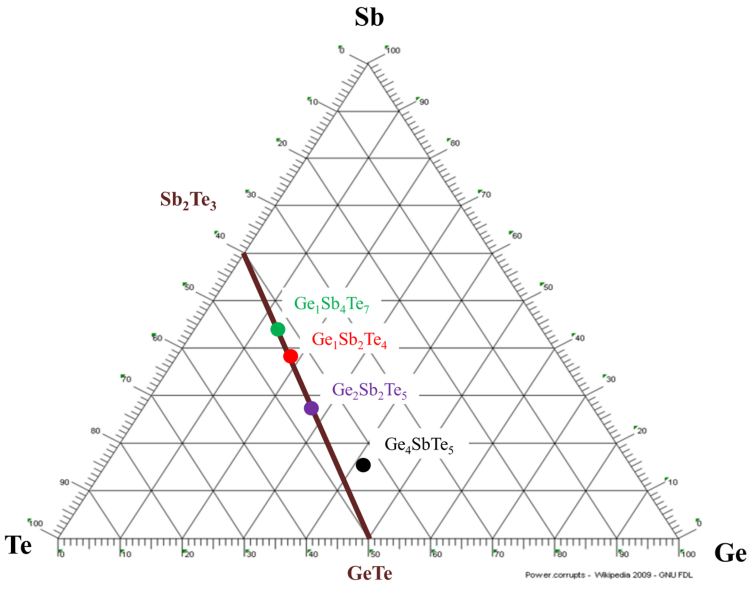

Figure 2.2: Ternary phase diagram of Ge, Sb, Te with the pseudo-binary tie-line of GeTe and Sb_2Te_3 and Ge_4SbTe_5 highlighted.

The study of GeTe-Sb_2Te_3 (GST) alloys for phase change memory applications, typically

involves the synthesis of the compounds in thin film form. Thin film deposition techniques such as chemical vapor deposition (CVD), atomic layer deposition (ALD), and molecular beam epitaxy (MBE) are all techniques which allow for rapid cooling rates.[74] Using these techniques with Ge-Sb-Te phase change materials yield the amorphous phases necessary for storing data. The following sections will discuss the crystal structure, and related phase transitions, for GeTe-Sb_2Te_3 alloys.

2.2 Structure and Bonding

The ability to switch between the amorphous and crystalline states is not a unique property to phase change materials, but the large optical/resistive contrast found in these compounds sets them apart.[75, 71, 76] The origin of the optical contrast between the amorphous and crystalline states has been a subject of experimental and theoretical investigations.[77] For traditional semiconductors such as Si and Ge, the transition from crystalline to amorphous yields only a change in the long-range order; the local tetrahedral bonding structure is maintained, but in Ge-Sb-Te compounds the crystalline phase exhibits octahedral coordination.[78] Specifically, the Ge atoms, Sb atoms, and vacancies randomly occupy the cation site of the rocksalt crystal structure with Te occupying the anion sublattice. Upon amorphization the local structure changes to tetrahedral coordination. This also changes the number of bonds between Ge and Te. The change in local structure and number of bonds has been shown experimentally and theoretically to be the origin of the optical contrast.[79]

2.2.1 Resonance Bonding

It has recently been shown that resonance bonding is a vital characteristic of phase change materials.[80] Resonance bonding is a term originally coined by Linus Pauling to describe the bonding nature in benzene.[81] Recently the theory has been extended to explain the undersaturated bonding nature in GST phase change materials. Resonance bonding is more generally defined as the superposition of symmetry-equivalent saturated bond configurations, which can be expressed using equation (2.1).[82]

$$\psi = \frac{1}{\sqrt{1+\alpha^2}}(\Phi_I + \alpha\Phi_{II}) \tag{2.1}$$

Most materials, such as Si, Ge, GaAs, and $CuInS_2$ have a mixing coefficient, α, which is very small or very large resulting in the covalent bonding structure of either Φ_I or Φ_{II}. In the case of materials with high levels of resonance bonding α is very close to unity, which yields a ground state wave function ψ that involves both bonding structures, Φ_I and Φ_{II}. In other words, for typical materials such as Si the average number of valence electrons per atom is equal to 4. This results in sp^3 hybridization and therefore tetrahedral bonding, but in $(GeTe)_mSb_2Te_3$ alloys the average number of valence electrons per atom is closer to, or equal to, 3. This bonding scenario is primarily promoted by the p electrons and yields no sp^3 hybridization, but rather delocalized electrons which are shared in the octahedral bonding.

The resonance bonding in phase change materials has a direct effect on the electrical and thermal properties. It has been shown that the high polarizability and incipient ferroelectricity in Ge-Sb-Te phase change materials is due to the strong electron-phonon interactions which are a direct effect of the resonance bonding.[83, 80, 84] The resonance bonding and associated distorted structure have also been shown to produce the degenerate p-type

semiconducting nature seen in $(GeTe)_m Sb_2Te_3$ alloys.[85, 86] Also the highly disordered structure and soft transverse optical phonon modes generated by the resonance bonding yield low thermal conductivity and low frequency optical phonon contributions to thermal conductivity.[87, 88, 89]

2.2.2 Crystal Structure

GeTe exists in the rhombohedral crystal structure ($R\bar{3}m$) below 673K. This rhombohedral structure can be understood as the distortion of the symmetric 6-fold coordinated rocksalt structure ($Fm\bar{3}m$) along the [111] crystal direction. This is consistent with the theory of Peierls distortion. Rather than 6 energy equivalent bonds, the unit cell of GeTe collapses to allow for 3 short bonds and 3 long bonds.[85] Group IV elements typically undergo the sp^3 hybridization, but this general rule falls short for elements such as Sn and Pb when relativistic effects become non-negligible and hybridization does not exist.[90]

On the other extreme of the GeTe-Sb_2Te_3 pseudo-binary tie-line is Sb_2Te_3 whose crystal structure can also be understood as a distorted cubic, or rhombohedral structure. Unlike GeTe, Sb_2Te_3 has an unequal number of cations and anions. The specific stacking sequence goes in units $Te - Sb - Te - Sb - Te$ with Te layers weakly bound by van der Waals forces. The crystal structure of these two compounds can be seen in Figure 2.3.

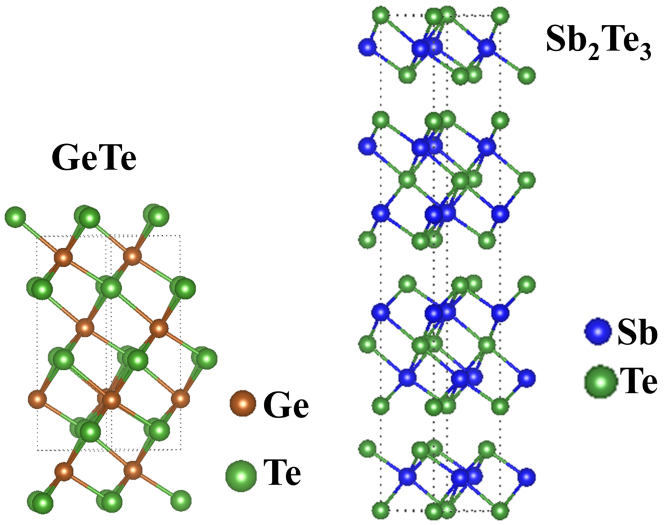

Figure 2.3: Crystal structure of GeTe and Sb_2Te_3, which has repeating vacancy layers between Te layers.These structures were generated using VESTA.[91]

$(GeTe)_mSb_2Te_3$ phase change materials can be best thought of as an intermediary between the crystal structures of GeTe and Sb_2Te_3. In the metastable rocksalt structure, which forms after the crystallization of the amorphous phase, Ge and Sb atoms, and vacancies randomly occupy the cation site, and Te atoms occupy the anion sublattice, while in the rhombohedral structure long repeating chains of Ge, Sb, and Te are interrupted by vacancy layers which connect the Te layers by van der Waals bonding. For the specific case of $Ge_2Sb_2Te_5$ the rocksalt and rhombohedral structures can be see in Figure 2.4.

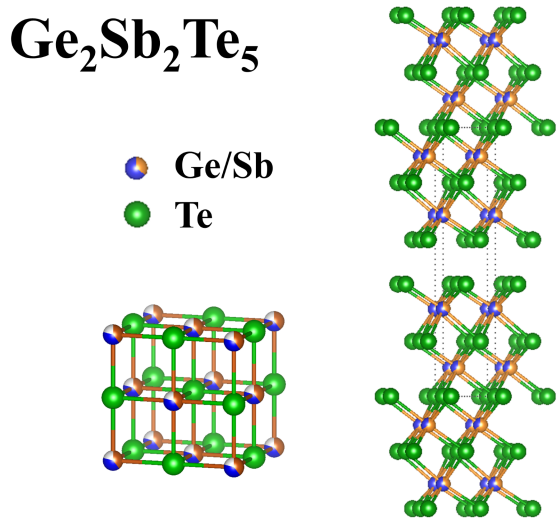

Figure 2.4: Rocksalt and Rhombohedral Crystal Structure of $Ge_2Sb_2Te_5$. These structures were generated using VESTA.[91]

The phase transition from the metastable rocksalt crystal structure seen in $(GeTe)_mSb_2Te_3$ phase change materials to the stable rhombohedral structure is an ordering transition. The phase transition is structural in nature, but is also accompanied by a change in the electrical properties. The transition is categorized as an insulator-metal transition and will be further explained in the following section.

2.2.3 Insulator-Metal Transition

Upon heating, the amorphous phase of GST materials transitions to the metastable cubic rocksalt structure, as was aforementioned. Upon further heating, the metastable cubic phase undergoes an ordering transition to the stable rhombohedral phase. This phase transition is structural in nature as the randomly assorted Ge and Sb atoms, and vacancies, order to form the layered trigonal $R\bar{3}m$ phase. However, in addition to the structural phase transition a change in the electrical resistivity is also seen at elevated temperature in GST materials.

Insulators can in general be defined as displaying a temperature coefficient of resistivity which is less than zero ($\frac{d\rho}{dT} < 0$), while metals display a positive temperature coefficient of resistivity ($\frac{d\rho}{dT} > 0$). Some materials display a transition in the electrical resistivity from insulating to metallic. This is categorized as a insulator-metal transition (IMT). One of the first theoretical investigations of IMTs was given by Mott in 1968.[92] He found that if the Coulomb energy (E_C) exceeds the Fermi energy (E_F) in materials, insulating behavior will be observed. Because both E_C and E_F are strongly dependent on the charge carrier concentration, there exists a critical charge carrier concentration for which E_C will either always be less than or greater than E_F. For GST materials the critical carrier concentration exceeds the Mott criterion and can not be explained in terms of a Mott transition.

A recent study of the phase change material $GeSb_2Te_4$ found that charge carrier mobility is anomalously low, with values less than $10 cm^2 V^{-1} s^{-1}$ for the rocksalt structure.[93] For most undoped semiconductors charge carrier mobility exceeds values of $100 cm^2 V^{-1} s^{-1}$. The small range of mobility seen for $GeSb_2Te_4$ implies highly localized charge carriers, as is also observed in amorphous semiconductors.[94] As the temperature of the material is increased the carrier mobility is increased nearly two orders of magnitude with little change in the carrier concentration, as can be seen in Figure 2.5.

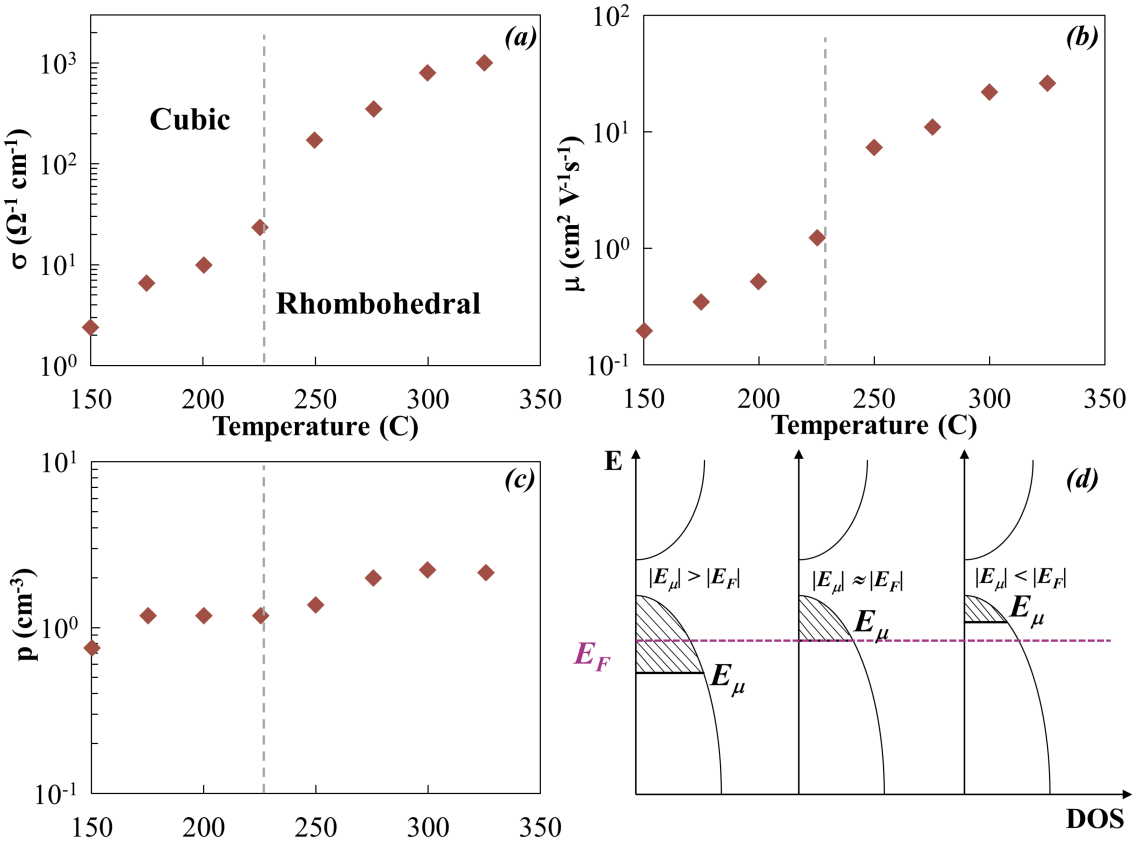

Figure 2.5: (a)Electrical conductivity versus temperature around the insulator-metal transition (represented here by dashed line) for $GeSb_2Te_4$, (b) and (c) hole concentration and hole mobility, respectively, around the insulator-metal transition. (d) Schematic of the mobility edge, E_μ in relation to the Fermi energy, E_F, which is the governing principle of an Anderson localization insulator-metal transition. In this schematic, zero energy is defined as the top of the valence band. The data in this figure was digitized and replotted from the work of Siegrist, *et al.* [93]

Though one would initially assume the IMT is associated with the structural phase transition, and therefore band gap, there is little change in the band gap from rocksalt to rhombohedral. Rather the ordering of the vacancies causes an increase in the hole mobility with little change in the hole concentration, as can be seen in Figure 2.5. This type of IMT can be described as an Anderson localization transition. The phenomenon is named after the physicist P.W. Anderson, who originally proposed the possibility of localized electrons in a semiconductor with a sufficiently high defect or impurity concentration.[95] As Anderson

outlined, the mobility edge, E_μ, is the energy at which electrons are localized. If E_F lies within these localized states, insulating behavior is seen, or $|E_\mu| > |E_F|$. As the temperature increases the mobility edge moves towards the Fermi energy($|E_\mu| \approx |E_F|$). Eventually the mobility edge crosses the Fermi energy, and electronic states become delocalized ($|E_\mu| < |E_F|$). A schematic of this effect can be seen in Figure 2.5(d).

Anderson localization transitions have been observed in photonic systems such as quantum-correlated materials and Bose-Einstein condensates.[96, 97] The phenomenon has also been observed in materials such as $Li_xFe_7Se_8$ and GST phase change materials.[98, 99]

2.3 Thermoelectric Properties

Many of today's state of the art thermoelectric materials are derived from chalcogenide based compounds. PbTe for example has been studied for thermoelectric power generation since the 1950s and is still being engineered to unrivaled ZT values.[100, 101] Bi_2Te_3 and Sb_2Te_3 were first studied in the 1950s and are still used for room temperature thermoelectric applications and Peltier cooling.[102] GeTe and $AgSbTe_2$, have also been studied for thermoelectrics since the 1960s.[40] Much of the success of this class of materials in thermoelectrics is attributed to low frequency phonons which lend to low lattice thermal conductivity and high charge carrier mobility.[103] The specific alloys which pertain to state of the art phase change materials, namely $(GeTe)_{1-x}(Sb_2Te_3)_x$ alloys have only recently begun to catch the attention of the thermoelectrics research community. The science and understanding behind GST phase change materials is still emerging, and in the following chapters various aspects of the thermoelectric properties of Ge-Sb-Te based materials will be explored in our quest to understand and engineer this intriguing class of materials.

Chapter 3

Experimental Procedures

The process of characterizing thermoelectric materials requires a number of techniques. For instance, understanding the crystal structure, microstructure, and elemental composition of the materials synthesized requires techniques such as X-ray Diffraction and Scanning Electron Microscopy/Energy Dispersive Spectroscopy. Additionally, characterization of the electrical and thermal properties is necessary to quantify the ZT and further understand the fundamental processes which elucidate high-ZT thermoelectric materials. The following sections will describe the experimental procedures used for the synthesis, processing, and characterization of the materials studied in this work.

3.1 Materials Synthesis

The following sections will describe the processes used to synthesize the bulk polycrystalline materials used in this work. Specifically, the general procedure used to achieve highly dense single phase GeTe-Sb_2Te_3 alloys will be presented.

3.1.1 Heating Procedures and Powder Processing

The following description of the process used to synthesize Ge-Sb-Te compounds is general in nature. In sections where additional chemicals and procedures are used a more specific description of the experimental processes will be presented. Stoichiometric amounts of Alfa Aesar germanium (Ge ingot, zone-refined, 99.9999%), Alfa Aesar antimony (Sb shot, 99.999%, 6 mm and smaller), and Alfa Aesar tellerium (Te lump, 99.999%) were placed in SiO_2 ampoules with 10mm inner diameter. The ampoules were evacuated to approximately 10^{-5} Torr and sealed using an oxygen-methane torch.

The samples were then heated to 900°C at a rate of $2°C min^{-1}$ and held for 12h. Samples were quenched using a room temperature water bath. Additional heat treatment at 590°C for 24h followed by water quenching was performed. These heating procedures were performed using a ThermoFisher BF51800 box furnace.

The obtained ingot was then crushed and ball-milled using a SPEX MixerMill 8000D with a stainless steel jar and 6 stainless steel balls for 5min This process ensures a fine, homogeneous powder, which is needed for further densification. The densification of materials in this work was achieved by spark plasma sintering, which will be discussed further in the following section. A graphic of the heating procedures and sample through the various steps of synthesis can be seen in Figure 3.1.

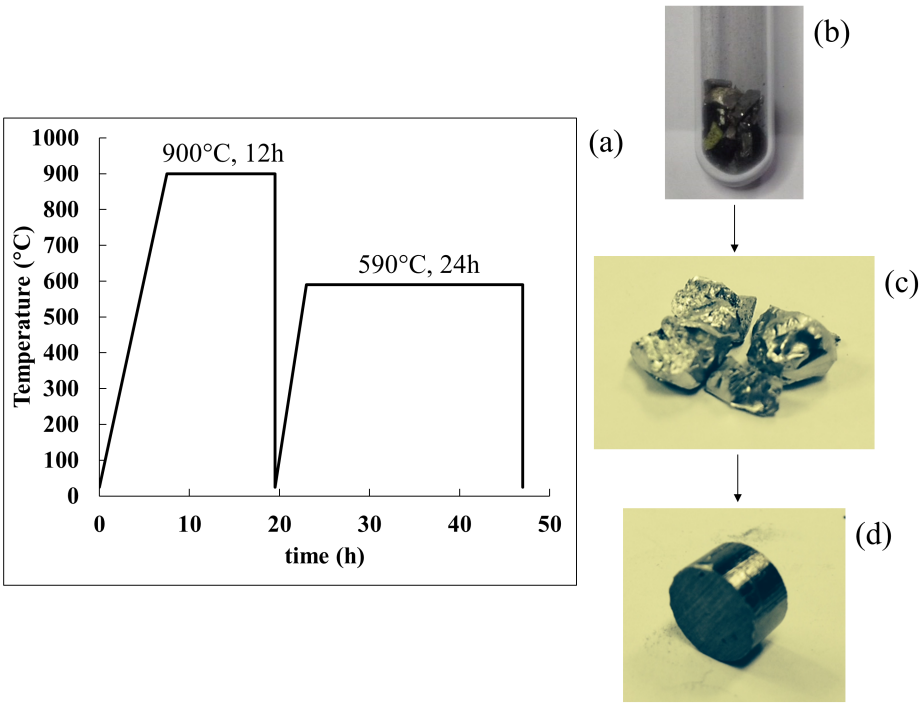

Figure 3.1: (a) Heating procedure shown here as temperature (°C) versus time (h) (b) Raw elements sealed in silica ampoule before heat treatment (c) Ingot obtained after melt and anneal process (d) Final disk obtained after densifying via spark plasma sintering.

3.1.2 Spark Plasma Sintering

Sintering is the act of consolidation of a material through the application of heat and/or pressure without melting, which usually results in an increase in the density.[104] When sintering ceramic materials, such as those used for thermoelectric applications, the heat and pressure used to sinter can be generated in a number of ways. Hot-pressing is a method by which pressure is applied directly to a material while heat is supplied externally. This process can takes upwards of hours to achieve density yields greater than 90%. The long sintering times associated with hot-pressing can cause undesirable grain coarsening, leading to increased grain size and the destruction of favorable thermoelectric performance.[105] An alternative application of heat during sintering is through the introduction of large electric

fields, which is called spark plasma sintering (SPS), electric-field assisted sintering (EFAS), or pulsed electric current sintering (PECS). In the SPS process high amperage ($100\text{A} - 600\text{A}$) DC current is pulsed on for 12s and off for 2s. The applied current induces joule heating within the sample and die, which allows for rapid temperature achievements. Additionally, the on/off behavior of the current is also said to induce high energy spark discharge between neighboring particles within the material, which in turn results in necking. The process of plasma creation is widely debated however and has yet to be unequivocally proven.[106]

SPS was used for the densification of all bulk thermoelectric materials studied in this work, which resulted in density yields greater than 95% theoretical in a matter of minutes. The specific parameters used such as time, temperature, and pressure were dependent on the composition and will be outlined in each corresponding section later, aside from $Ge_{17}Sb_2Te_{20}$, which will be used as an example here. SPS was performed using a Dr. Sinter-Lab spark plasma sintering system, model SPS-211Lx. Powder of $Ge_{17}Sb_2Te_{20}$ was placed in a 10mm graphite die and sandwiched between two layers of graphite foil and graphite plungers. Uniaxial pressure was applied on the graphite plungers while a type-K thermocouple was placed into a hole drilled into the side of the graphite die. A programmed temperature controller was used to control the ramp rate and holding temperature/time for a given sample. For example, $Ge_{17}Sb_2Te_{20}$ was sintered via the following temperature profile: ramp to 300°C in 2min, ramp to 465°C in 3min, hold at 465°C for 5min, with an applied uniaxial pressure of 45 MPa. This procedure was determined through numerous trials for optimization for $Ge_{17}Sb_2Te_{20}$. All SPS runs were performed under vacuum levels of approximately 10^{-2} Torr. Software was used to digitally monitor the voltage, current, temperature, pressure, z-axis displacement, and vacuum level in real time. The data generated from this monitoring system was used to aid in developing the sintering profile of a given material.

Optimizing the sintering temperature and pressure for a given material is an important and necessary step in the synthesis process. The above sintering profile for $Ge_{17}Sb_2Te_{20}$ was utilized to achieve theoretical densities consistently greater than 99%. By adjusting the sintering temperature and monitoring the z-axis displacement as the sample sinters one can collect important data for understanding the sintering process. In Figure 3.2 the displacement of plungers during sintering versus the sintering temperature can be seen. Notice that increasing the temperature while keeping the hold time of 5min constant allowed for an increase in displacement which directly translated to a higher density yield.

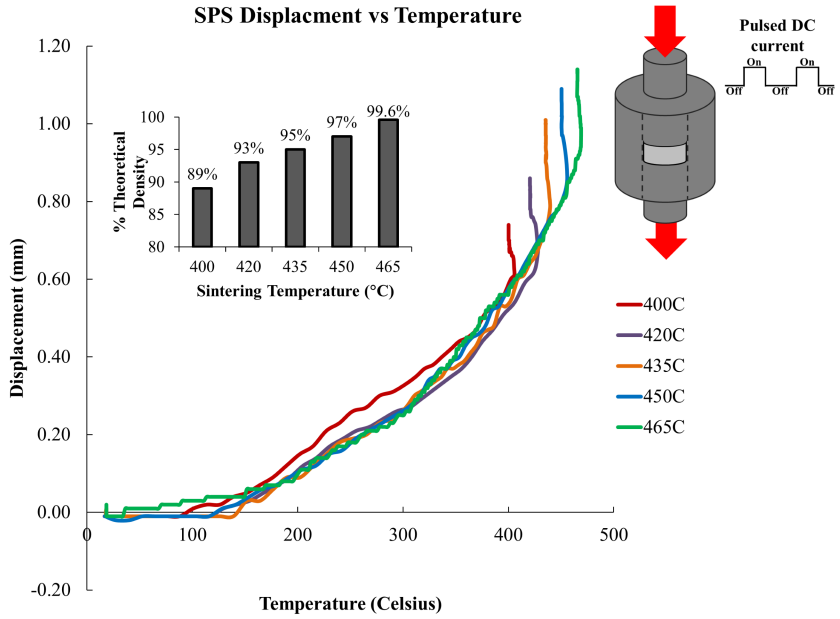

Figure 3.2: Z-axis displacement of sample during SPS versus temeprature for various holding temperatures (*400*°C, *420*°C, *435*°C, *450*°C, *465*°C). A clear correlation between % theoretical density yield and SPS temperature can be observed.

3.2 Characterization Techniques

The following sections will be a description of the techniques used to characterize the materials synthesized in this work. Most of the measurements were performed at Michigan State

University. However, all microscopy was performed using the equipment in the Center for Advanced Microscopy overseen by Dr. Stanley Flegler, and laser flash techniques were performed by Karl Dersch using the equipment in Dr. Timothy Hogan's lab in the Engineering Research Complex.

3.2.1 X-ray Diffraction

X-ray Diffraction was performed using a Rigaku MiniFlex-II at room temperature with Cu-Kα radiation. A small amount of sample was pulverized and mounted onto a glass slide and measured at a rate of $3°\text{min}^{-1}$ in the range of $15-90°2\theta$. High temperature X-ray Diffraction on some of the samples in this work was performed at Oak Ridge National Laboratory in collaboration with Dr. Edgar Lara-Curzio and Dr. Thomas Watkins.

3.2.1.1 Principle of X-ray Diffraction

X-ray diffraction can yield a wealth of information about the structure and phase purity of a material. This information can be extracted from the shape, intensity, position along the 2θ axis, and number of diffraction peaks. To understand the principle of x-ray diffraction it is best to imagine a periodic lattice of atoms, with spacing d. X-rays interact with the atoms (in this case perfectly elastically) and are scattered off of the atoms, some with the same incident angle (θ) to the plane normal, which can be visualized in Figure 5.2.

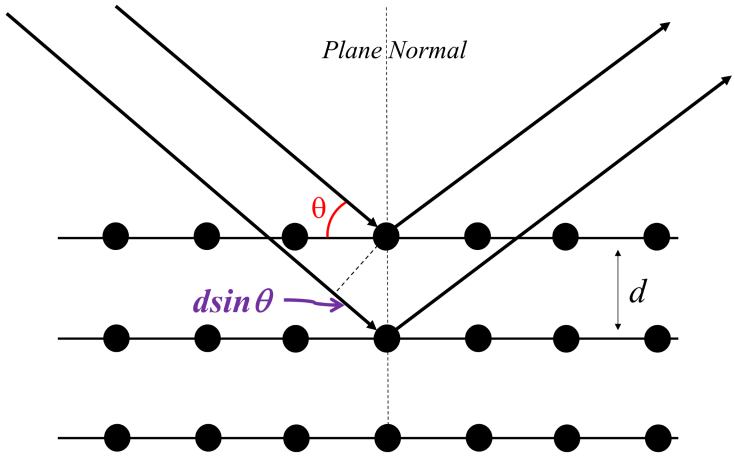

Figure 3.3: A schematic which showcases the principle of X-ray Diffraction with a periodic lattice of atoms.

When the wavelength of the X-rays (λ) is equal to twice the spacing offset $dsin\theta$ the result is constructive interference of the scattered X-rays. The relation between the interplanar spacing, d, and the wavelength of incident X-rays, λ, is known as Bragg's law of diffraction and is expressed in equation (3.1).[107]

$$n\lambda = 2dsin\theta \tag{3.1}$$

The planes of atoms in a given crystal lattice determine the diffraction of X-rays. These atomic planes are expressed using Miller indices (hkl) which are an expression of their location in reciprocal space. For example, for a face-centered cubic crystal structure, the (110) plane intersects 6 atoms, as can be seen in Figure 3.4.

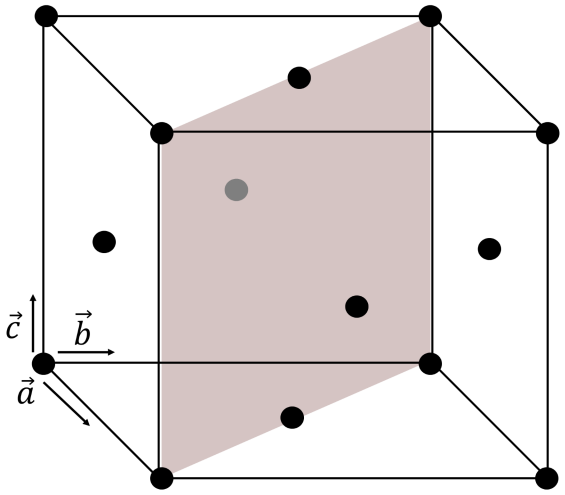

Figure 3.4: The (110) plane in a face-centered cubic crystal structure.

Each diffraction peak in an X-ray diffraction pattern therefore corresponds to an (hkl) plane in a given crystal structure. Once a peak is indexed with its respective Miller index the location on the 2θ axis can be related back to the unit cell parameter. The general definition for relating the d-spacing to the plane normal vector $\mathbf{K}_{hkl}$ can be seen in equation (3.2).

$$d_{hkl} = \frac{2\pi}{|\mathbf{K}_{hkl}|} \tag{3.2}$$

The plane normal vector is defined as $\mathbf{K}_{hkl} = h\mathbf{A} + k\mathbf{B} + l\mathbf{C}$, where $\mathbf{A}$, $\mathbf{B}$, and $\mathbf{C}$ are defined as follows:

$$\mathbf{A} = \frac{2\pi(\mathbf{b} \times \mathbf{c})}{\mathbf{a} \cdot (\mathbf{b} \times \mathbf{c})}, \mathbf{B} = \frac{2\pi(\mathbf{c} \times \mathbf{a})}{\mathbf{a} \cdot (\mathbf{b} \times \mathbf{c})}, \mathbf{C} = \frac{2\pi(\mathbf{a} \times \mathbf{b})}{\mathbf{a} \cdot (\mathbf{b} \times \mathbf{c})} \tag{3.3}$$

In equation (3.3) $\mathbf{a}$, $\mathbf{b}$, and $\mathbf{c}$ are the real space lattice vectors. By applying the necessary symmetry for a given crystal structure equation (3.2) can be greatly simplified. For example, in the case of a cubic crystal structure the relationship between the lattice parameter a, (hkl),

and the interplanar spacing d can be expressed as:

$$d_{hkl} = \frac{a}{\sqrt{h^2 + k^2 + l^2}} \tag{3.4}$$

3.2.1.2 Structure Factor and Diffraction Intensity

In an actual material the scattering process for X-rays depends on the type of atom in the lattice. The Thomson equation, essentially a low-energy limit of Compton scattering, expresses the intensity of coherently scattered electromagnetic waves as being inversely proportional to the square of the mass of the scattering particle.[108] The atomic nucleus therefore plays a small role in scattering the X-rays, rather the electrons are the dominant scattering mechanism. The intensity of diffraction for an X-ray diffraction pattern will therefore be dependent on the atomic number Z for a given atomic species. The atomic scattering factor, f describes the efficiency of scattering for a given atom, and along with the (hkl) plane, plays an important role in determining the intensity and angle of a diffraction peak.

The intensity of the beam diffracted is determined in part by the structure factor, F_{hkl}, which can be written as follows:

$$F_{hkl} = \sum_{i=1}^{N} f_n e^{2\pi i(hu_n + kv_n + lw_n)} \tag{3.5}$$

Equation (3.5) also determines the allowed diffraction peaks for a given crystal structure. For example, for the diamond crystal structure, all of the diffraction peaks must have (hkl) which are either all odd, or all even and sum to a multiple of four.

In addition to the structure a number of other variables play a role in determining the intensity of a diffracted beam. The multiplicity factor, p, considers the relative proportion

of (hkl) planes which contribute to the same reflection. The Lorentz-polarization factor subtracts away from the intensity of a diffracted peak and is expressed as $\frac{1+cos^2 2\theta}{sin^2\theta cos\theta}$. The absorption factor A depends on the diffraction geometry being used and accounts for any absorption taking place within the sample. The temperature contribution is expressed as e^{-2M} where M is dependent on the amplitude and scattering properties of the lattice vibrations within the specimen. The overall intensity calculation can be seen in equation (3.6).[108]

$$I = |F|^2 p[\frac{1 + cos^2 2\theta}{sin^2\theta cos\theta}]A(\theta)e^{-2M} \tag{3.6}$$

3.2.2 Differential Scanning Calorimetry

Differential Scanning Calorimetry (DSC) is a commonly used technique for the thermal characterization of solids and liquids. The relatively simple and accurate measurement can yield information about melting/crystallization behavior, solid-solid phase transformations, glass transitions, degree of crystallinity, specific heat, and more. For the following work DSC was performed on a Netzsch DSC 200-F3 Maia. Aluminum crucibles were used in the temperature range of 50-600°C. All measurements were performed under a constant flow of Argon. Sample masses ranged from 50mg - 100mg. An Al_2O_3 single crystal (100mg) was used for the calculation of heat capacity.

For each run a baseline measurement was performed, in which an empty sample crucible and reference crucible were measured within the temperature range of interest. DSC was performed using the heat flux method. Two aluminum crucibles, each pierced to allow for ventilation of sublimated gases, are placed on heaters. The heating rates of each are precisely controlled and the heat flux to each crucible is monitored throughout the measurement. The sample will change the thermal resistance as compared to the empty reference crucible and is

monitored as a function of the measurement temperature. Using the sapphire standard allows for a ratio method of calculation whereby the heat capacity can be calculated. Figure 3.5 is a schematic of the measurement setup used.

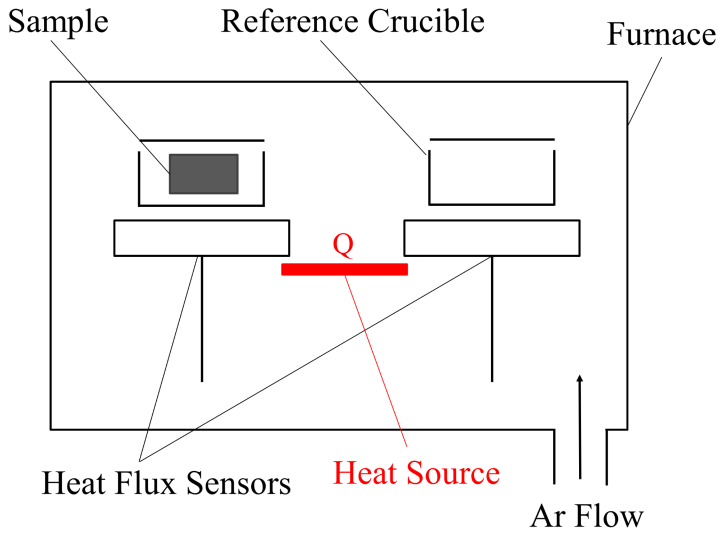

Figure 3.5: A schematic of the setup used for performing DSC. Each crucible is placed on a heater which is precisely monitored to determine the amount of heat flux needed to heat each crucible.

3.2.3 Scanning Electron Microscopy

Scanning Electron Microscopy(SEM) was performed in the Center for Advanced Microscopy at Michigan State University. The specific instrument used was a JEOL 6610 LV, which was also equipped with an Oxford EDX for elemental analysis. The JEOL 6610 LV provides high resolution imaging within the range of 5X to 50,000X.

The most common imaging mode for SEM is through the collection of secondary electrons which are produced from interactions of the electron beam with the material. The high energy electrons of the beam interact inelastically with the atoms near the surface of the material (typically only a few nanometers). These inelastic collisions then produce electrons

from the K-shell of the atoms which are collected. The collected electrons are then accelerated and a photomultiplier converts the signal to a large flux of photons. These photons are then digitally processed and used to create an image. The secondary electrons are typically very low energy ($\leq$ 50eV) and therefore originate from the surface of the material.

Some of the interactions between the electron beam and the material are elastic and result in high energy electrons which are backscattered out of the material. The elastic collisions are dependent on the mass of the atoms, where the higher mass atoms (higher Z-number) will scatter more strongly and the lighter mass atoms (low Z-number) will scatter less strongly. The result of the collection of these high energy electrons is an image where areas with high average atomic number are brighter than those of low average atomic number.

Furthermore, these high energy interactions also generate X-rays which are characteristic of the atomic number of the material at hand. Analyzing these X-rays can allow for an elemental characterization of the material. This form of characterization is therefore called energy dispersive X-ray spectroscopy (EDS, EDX, XEDS). The principle of EDX is based on the fact that each atom has a characteristic atomic structure. Upon interaction with the high energy electron beam an electron will be ejected from an energy level. An electron at a higher energy state will then relax into the unfilled state thereby creating an X-ray. The specific wavelength of the X-ray is dependent on the energy level the electron is transitioning to and from. All of these transitions will produce X-rays which are characteristic of a specific atomic species, and can therefore be used to analyze the elemental composition of a material. A basic schematic of this process and the various energy levels analyzed in EDX can be seen in Figure 3.6.

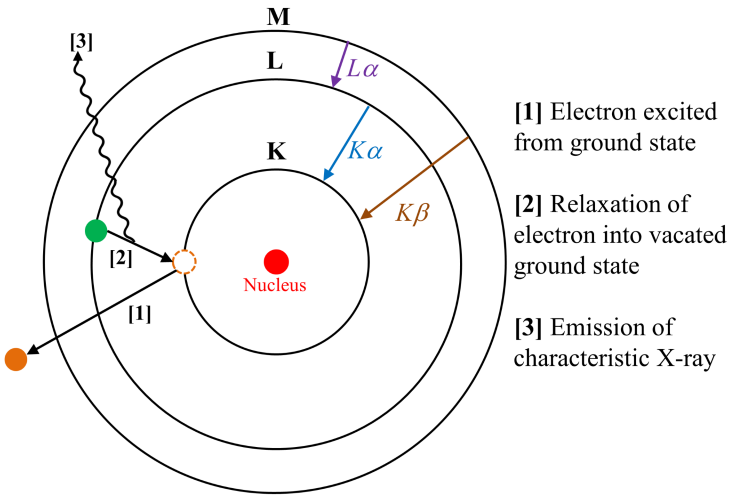

Figure 3.6: A schematic which depicts the principle of energy dispersive X-ray spectroscopy (EDX).

The naming convention used for the types of electron transitions which produce X-rays shows first a letter K, L, or M, followed by a Greek letter, such as α or β. The first letter describes the states into which the higher energy electron is transitioning. The Greek letter describes the number of states transitioned through to reach the destination state. For example, an electron transition from the L state to the K state will produce an X-ray named $K\alpha$.

3.2.4 Hall Measurements

The charge carrier concentration is an important parameter in understanding the thermolectric properties of a material. To directly measure the carrier concentration Hall measurements were performed. These measurements are based upon the Hall effect, originally established by Edwin Hall in 1880.[109] Hall found that when a magnetic field is applied to a material, orthogonal to the current flow, the electrons are deflected resulting in a measurable transverse voltage, ΔV_H. A schematic of the setup for measuring the Hall effect can be seen

in Figure 3.7, where B is the applied magnetic field, I_S is the applied current, ΔV_H is the Hall voltage, ΔV_S is the resistive sample voltage, which is used to calculate the electrical resistivity, w is the sample width, t is the thickness, and p is the probe seperation associated with measuring ΔV_S.

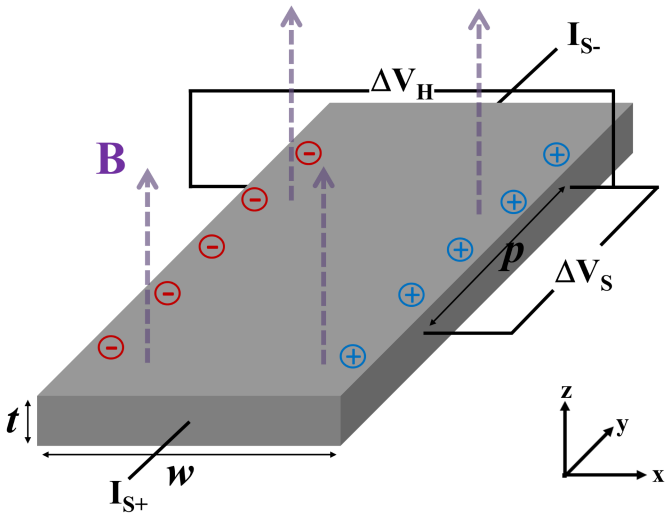

Figure 3.7: A typical mounting setup for measuring the Hall effect, and thereby the carrier concentration, in a material.

With no magnetic filed present, charge carriers move along the length of slab and no transverse voltage is generated. The deflection of charges due to the presence of a magnetic field **B** with drift velocity **v** is a result of the Lorentz force, defined as:

$$\mathbf{F} = q\mathbf{v} \times \mathbf{B} \tag{3.7}$$

As a result of the Lorentz force, negative charges will accumulate on one side of the sample, which results in the establishment of an electric field, E_H, that balances with the Lorentz force, equation (3.8):

$$qE_H = qv_{dx}B_z \tag{3.8}$$

The current density in the y direction can be defined as $J_y = qnv_{dy}$, and therefore equation (3.8) can be expressed as:

$$E_H = (\frac{1}{en})J_y B_z \tag{3.9}$$

Equation (3.9) can be further expressed in terms of the measured quantities: V_H, the Hall voltage, B_z, the applied magnetic field, n, the carrier concentration, e, the elementary unit of charge, and t, the sample thickness.

$$V_H = \frac{I_y B_z}{net} \tag{3.10}$$

From equation (3.10) we can define a parameter called the Hall coefficient as:

$$R_H = \frac{-1}{ne} \tag{3.11}$$

The resistance across the Hall probes for various values of the magnetic field were measured using a 1T magnet. By plotting the resistance versus magnetic field and measuring the slope, the carrier concentration was determined. By also using ΔV_S along with the known probe separation p the electrical resistivity was calculated along with the carrier concentration which allowed for a calculation of the carrier mobility ($\mu = \sigma/ne$, where μ is the mobility, σ is the electrical conductivity, n is the carrier concentration). The Hall measurements were done under a vacuum of approximately 10^{-5} Torr, from $80\text{K} - 300\text{K}$ using liquid nitrogen to reach cryogenic temperatures.

3.2.5 Low Temperature Transport Properties

The electrical resistivity, Seebeck coefficient, and thermal conductivity were measured on a custom-built system between the temperatures of 80K and 350K. Liquid nitrogen is used to reach cryogenic temperatures. The setup seen in Figure 3.8 was built on a Janis cryogenic measurement system. A sample cut into a parallelepiped is attached to a copper base, which acts as a thermal sink, using silver epoxy. A resistor of approximately 800Ω was wrapped in copper and attached to the top of the sample (approximate dimensions: 8mm x 2mm x 2mm), which was also done using silver epoxy. Two small copper strips were attached to the face of the sample using silver epoxy which act as solder points for the thermocouple. Phosphor-bronze wiring was used to inject electrical current to the heater, I_H, and through the sample, I_S. The material was chosen because of its high electrical conductivity but relatively low thermal conductivity, which keeps the thermal conduction losses to a minimum. Two thermocouples made from copper and constantan alloy are soldered to the two copper probes with known separation, l.

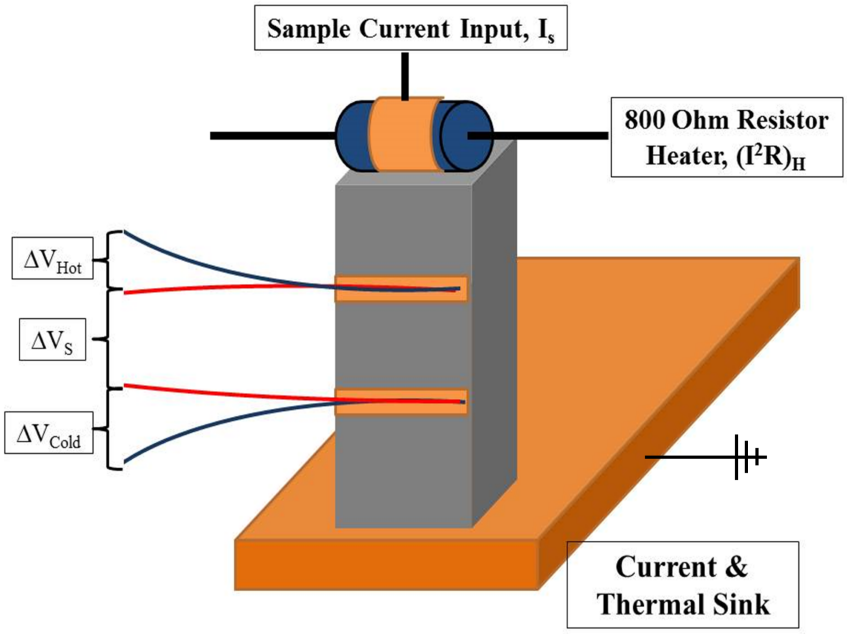

Figure 3.8: Schematic of system used for measuring the electrical resistivity, Seebeck coefficient, and thermal conductivity across the temperature range of 80-350K.

3.2.5.1 Electrical Resistivity

The two copper wires in the thermocouples are used to measure the voltage difference generated by the current injected through the sample, ΔV_S. I_S is applied in both the positive and negative directions so that the voltage contribution from the Peltier effect can be subtracted out. Using ΔV_S and I_S the resulting resistance, R_S can be determined and used to calculate the electrical resistivity. Using the sample dimensions of width, (w), thickness, (t), which together give a surface area, (S) and probe separation, (l) the electrical resistivity is calculated using equation (3.12).

$$\rho = R_S \frac{S}{l} \tag{3.12}$$

I_S and ΔV_S were supplied and measured, respectively, using Keithley 2000 multimeters. The dimensions of the sample were measured using calipers. There is intrinsic error

associated with the voltage measurement and the measurement of the sample dimensions. The uncertainty associated with measuring the electrical resistivity using this setup can be estimated using equation (3.13).

$$\Delta\rho = \rho\sqrt{(\frac{\Delta R}{R})^2 + (\frac{\Delta l}{l})^2 + (\frac{\Delta w}{w})^2 + (\frac{\Delta p}{p})^2} \tag{3.13}$$

For a sample with an electrical resistivity of 1mΩ cm, dimensions of 3mm$x$3mm, and a probe separation of 4mm the uncertainty is approximately $\pm$8%. The majority of the uncertainty associated with the electrical resistivity stems from the error in measuring the dimensions and size of the copper contacts used for the probes.

3.2.5.2 Seebeck Coefficient and Thermal Conductivity

The Seebeck coefficient is a parameter determined directly from the measured voltage difference, ΔV, that is generated by a temperature difference, ΔT, and is therefore independent of geometry, as can be seen in equation (3.14).

$$S = \frac{\Delta V}{\Delta T} \tag{3.14}$$

The error associated with measuring the Seebeck coefficient is dependent only on the uncertainty associated with the multimeters used to measure the voltage readings from the copper wires and thermocouple. The error for Seebeck coefficient is equal to approximately $\pm$2%. The thermal conductivity, on the other hand, is dependent on dimensions and therefore contains more uncertainty. Current is supplied to the resistive heater, I_H, on top of the sample, which in turns induces joule heating equivalent to $I_H^2 R$. This heat is driven through the sample creating a temperature gradient. The associated ΔT is measured and used to

calculate a thermal conductance $K = \frac{(I_H^2 R)}{\Delta T}$. The thermal conductivity is then calculated using the dimensions of the sample and the thermal conductance, as can be seen in equation (3.15).

$$\kappa = K\frac{l}{S} \tag{3.15}$$

where l is the probe separation and S is the surface area; calculated by length of sample, l times the width, w. The uncertainty associated with measuring the thermal conductivity looks similar to the uncertainty calculation for electrical resistivity. The uncertainty is dependent, of course on the value of thermal conductivity, but for a setup similar to that aforementioned for the error calculation in electrical resistivity, and a thermal conductivity around $2\mathrm{Wm}^{-1}\mathrm{K}^{-1}$, the average uncertainty is approximately $\pm 7\%$. The specific equation for the calculated uncertainty of thermal conductivity used in this work can be seen in equation (3.16).

$$\Delta\kappa = \kappa\sqrt{(\frac{\Delta I_H}{I_H})^2 + (\frac{\Delta V_H}{V_H})^2 + (\frac{\Delta dT}{dT})^2 + (\frac{\Delta l}{l})^2 + (\frac{\Delta h}{h})^2 + (\frac{\Delta w}{w})^2} \tag{3.16}$$

When measuring the thermal conductance of a material using this steady-state technique it is assumed that the all of the power generated by the resistive heater flows through the material, but near room temperature heat loss due to radiation becomes significant. According to the Stefan-Boltzmann law, the total energy radiated per unit surface area of a black body per unit time is given by equation (3.17).[110]

$$W = \sigma A T^4 \tag{3.17}$$

where σ is the Stefan-Boltzmann constant (5.070 x $10^{-8}\mathrm{Wm}^{-2}\mathrm{K}^{-4}$), A is the surface area, and T is the temperature.[12] The thermal conductance is therefore expressed as:

$$\frac{dW}{dT} = 4\sigma AT^3 \tag{3.18}$$

Equation (3.18) is an expression for the amount of conductance lost to radiation. It is therefore important to subtract out this contribution to thermal conductivity in order to obtain reliable measurements near room temperature (300K). The actual calculation used to subtract this radiative contribution can be seen in equation (3.19).

$$\kappa = [K_{measured} - K_{loss}(\frac{T}{300}^3)]\frac{l}{S} \tag{3.19}$$

In equation (3.19) the value for K_{loss} is taken to be $0.00146\mathrm{WK}^{-1}$. This value has been determined by independent standardized measurements in our laboratory. The thermal conductivity, with and without the radiation correction, of a sample of Bi_2Te_3 can be see in Figure 3.9.

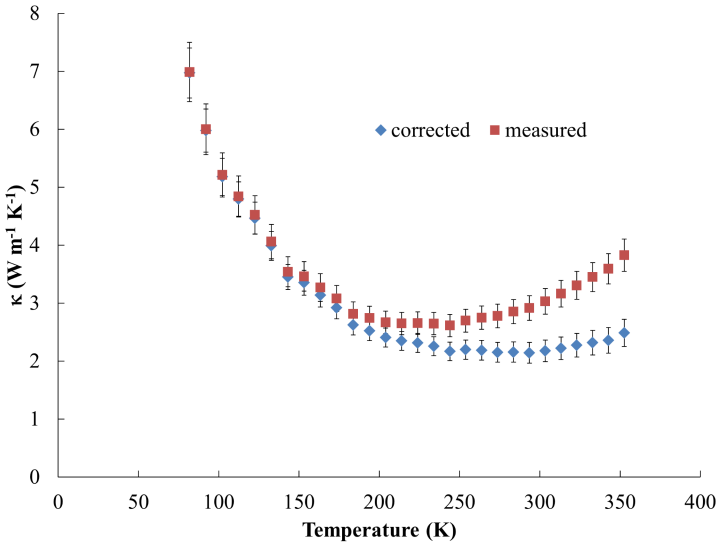

Figure 3.9: Thermal conductivity versus temperature for Bi_2Te_3 with and without the radiation correction, an effect which can cause an overestimation of thermal conductivity, especially at temperatures near and above room temperature.

The additive effect of radiation can especially be seen at temperatures near and above 300K. However as the temperature continues to increase, the ability to accurately subtract the radiative contribution becomes more difficult using this steady-state measurement technique. Other methods for measuring thermal conductivity must therefore be employed as will be discussed in the following sections.

3.2.6 High Temperature Transport Properties

3.2.6.1 Electrical Resistivity and Seebeck Coefficient

The electrical resistivity and Seebeck coefficient at high temperature (300 - 1073K) were measured using a ZEM-3 from ULVAC-RIKO, Inc. The same geometry used for cryostatic transport measurements was used for this procedure as well. The sample rests between two electrodes which apply pressure to ensure Ohmic contacts for inputting electrical and heat currents. Two spring loaded thermocouples form pressure contacts to the side of the sample

for measuring a voltage difference and temperature difference. The mounting chamber is evacuated using a roughing pump and back-filled with helium. Measurements can be performed within ±5% uncertainty between room temperature and 1073K. At each temperature multiple temperature differences are established and the Seebeck coefficient and electrical resistivity are measured for each and averaged.

3.2.6.2 Thermal Diffusivity

At higher temperatures measuring thermal conductivity using a steady-state technique, as was used for the aforementioned crysostat measurements, becomes too difficult. Radiation losses become larger making the uncertainty and noise levels too high for accurate measurement. The alternative is to use a non-steady-state technique. There a number of techniques which can be used, but for bulk polycrystalline samples measuring the thermal diffusivity and calculating the thermal conductivity is reliable. The relationship used to calculate thermal conductivity at high temperatures can be seen in equation (3.20).

$$\kappa = \alpha \Delta C_p \tag{3.20}$$

where α is the thermal diffusivity, Δ is the volumetric density, and C_p is the heat capacity. Laser-flash measurements were used to measure the thermal diffusivity at Michigan State University on a Netzsch LFA-457 MicroFlash system. The laser-flash technique uses a laser induced heat pulse on one side of a disk-shaped sample and measures the time associated with heating the reverse side of the sample. The response is time-dependent and used to calculate the time to half maximum $t_{1/2}$. In the adiabatic case the thermal diffusivity is

calculated as follows:[111]

$$\alpha = 0.1388\frac{d^2}{t_{1/2}} \tag{3.21}$$

Samples for this measurement were cut from the sintered pellets with the approximate dimensions of $10mm$ diameter and $1mm$ thickness. Density was measured at room temperature using an ethanol-based Archimedes method, which is independent of geometry. The specific heat was measured using a Netzsch DSC 200-F3 Maia, as was aforementioned. The uncertainty associated with calculating thermal conductivity using equation (3.20) can be quite high and was calculated using equation (3.22). The values for uncertainty depend on the specific sample, but on average are around $\pm 10\%$.

$$\Delta\kappa = \kappa\sqrt{(\frac{\Delta\alpha}{\alpha})^2 + (\frac{\Delta C_p}{C_p})^2 + (\frac{\Delta\rho}{\rho})^2} \tag{3.22}$$

The figure-of-merit, ZT, at high temperature is a calculation using ρ, S, and κ. The uncertainty associated with ZT can be calculated using equation (3.23), which is typically on the order of $\pm 13\%$.

$$\Delta ZT = ZT\sqrt{(\frac{2\Delta S}{S})^2 + (\frac{\Delta\rho}{\rho})^2 + (\frac{\Delta\kappa}{\kappa})^2} \tag{3.23}$$

Chapter 4

$(GeTe)_{1-x}(Sb_2Te_3)_x$ Compounds

Some of the first thermoelectric studies of $(GeTe)_{1-x}(Sb_2Te_3)_x$ alloys were conducted by Christakudis, *et al* in 1991 and Konstantinov, *et al* in 2001.[112, 113] Each found lattice thermal conducitity values below $2Wm^{-1}K^{-1}$ and ZT values comparable to PbTe in the temperature range of $500K - 800K$. Rosenthal, *et al* in 2011 gave a detailed analysis of the crystal structure and thermoelectric properties of GeTe-rich $(GeTe)_{1-x}(Sb_2Te_3)_x$ alloys.[114] In the following sections a discussion of the crystal structure, phase transition, and thermoelectric properties of $(GeTe)_{1-x}(Sb_2Te_3)_x$ will be presented.

4.1 Experimental

Samples with composition $(GeTe)_{1-x}(Sb_2Te_3)_x$, with x = $0.02, 0.04, 0.059, 0.06$, and 0.083, were synthesized by placing stoichiometric amounts of Ge, Sb, and Te in evacuated and sealed ampoules. The specific samples $x = 0.059$ and $x = 0.083$ correspond to $Ge_{12}Sb_2Te_{15}$ and $Ge_{17}Sb_2Te_{20}$, both of which have been discussed in the literature.[114] The samples were melted at 900°C, held for 12h, and quenched. The resulting ingots were ball-milled for 5min and the powder densified using SPS at 400°C, for 15min, under 40MPa of pressure. Samples for X-ray diffraction, thermoelectric characterization, DSC, and Hall measurements

were cut from the sintered pellet using a circular diamond saw. Thermal conductivity was calculated using the measured thermal diffusivity, the specific heat (which was assumed as the Dulong-Petit value), and the measured volumetric density.

4.2 Results and Discussion

The X-ray diffraction patterns for all samples can be seen in Figure 4.1. Samples up to x=0.059 showed a single phase rhombohedral crystal structure. For greater concentrations of Sb_2Te_3 impurities of elemental Sb were seen in the patterns (PDF#98-000-0095). The rhombohedral structure of GeTe has characteristic double peaks around $43°2\theta$. The peaks are generated because of the rhombohedral unit cell of GeTe, which can be thought of as having a slight distortion in the [111] direction of the rocksalt crystal structure. As the Sb_2Te_3 concentration is increased the separation of these peaks decreases, until $x = 0.06$, which begins to show a single peak at $43°2\theta$, as can be seen in the Figure 4.1 inset. For $x = 0.083$ the doublets are completely replaced by a single peak, which corresponds to the full extension of the distorted rocksalt angle back to $90°$, aside from some peak shoulders which could correspond to the lingering existence of some off-cubic phase.

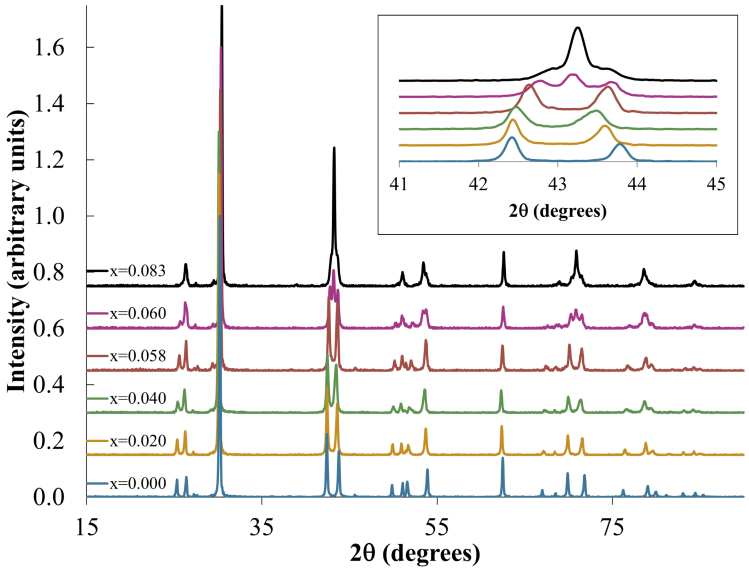

Figure 4.1: X-ray diffraction patterns for $(GeTe)_{1-x}(Sb_2Te_3)_x$, where x varies from 0%, 2%, 4%, 5.9%, 6%, and 8.3% Sb_2Te_3. As Sb_2Te_3 content increases the rhombohedral crystal structure slowly changes to the rocksalt structure, as can be seen in the inset.

GeTe displays an increasing electrical resistivity with increasing temperature from values of less than 0.1mΩ cm at 80K to approximately 0.6mΩ cm above 800K. The phase transition from rhombohedral to cubic at approximately 600K is accompanied with a slight dip in electrical resistivity as well. As Sb_2Te_3 is substituted for GeTe the electrical resistivity is increased nearly two orders of magnitude, with the 8.3% Sb_2Te_3 ($Ge_{12}Sb_2Te_{15}$) having the highest values. The electrical resistivity versus temperature for $(GeTe)_{1-x}(Sb_2Te_3)_x$ can be seen in Figure 4.2.

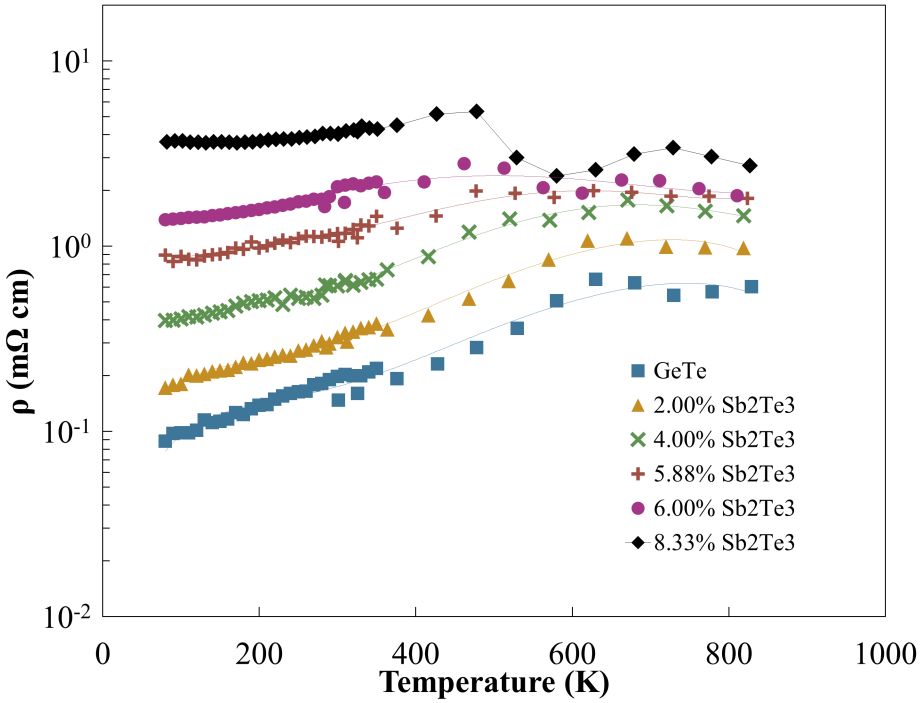

Figure 4.2: Electrical resistivity versus temperature for $(GeTe)_{1-x}(Sb_2Te_3)_x$, where x varies from 0%, 2%, 4%, 5.9%, 6%, and 8.3% Sb_2Te_3.

The increase in electrical resistivity can be traced to an increased concentration of vacancies in the crystal structure which causes a decrease in the hole mobility as the Sb_2Te_3 concentration is increased. These vacancies act as additional scattering sites, which scatter both charge carriers and phonons. It is therefore expected that the thermal conductivity will be decreased as well. The hole concentration and hole mobility, as measured and determined by Hall measurements, can be seen in Figure 4.3.

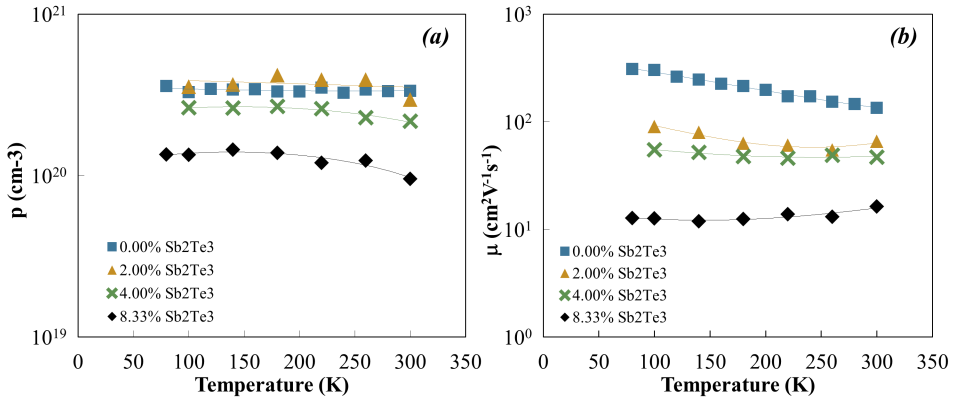

Figure 4.3: Hole Concentration, (a) and Hole Mobility, (b) versus Temeperature for $(GeTe)_{1-x}(Sb_2Te_3)_x$.

The Seebeck coefficient is also increased as a function of Sb_2Te_3 concentration, as can be seen in Figure 4.4. Based on the behavior of the Seebeck coefficient and electrical resistivity it was believed that Sb_2Te_3 was causing a change in the hole concentration. However, the Hall measurements revealed a decrease hole mobility by approximately two orders of magnitude, with little change observed in the hole concentration. The small decrease in the hole concentration is most likely due to an Sb deficiency in the compound, as small Sb impurities were seen in the X-ray diffraction patterns.

The high hole mobility found in GeTe yields low electrical resistivity and power factor values in excess of $50\mu Wcm^{-1}K^{-2}$ above 600K. Substituting Sb_2Te_3 causes a systematic decrease in the power factor, with peak values approximately equal to $20\mu Wcm^{-1}K^{-2}$ for 8.3% Sb_2Te_3, which can be seen in Figure 4.5(a).

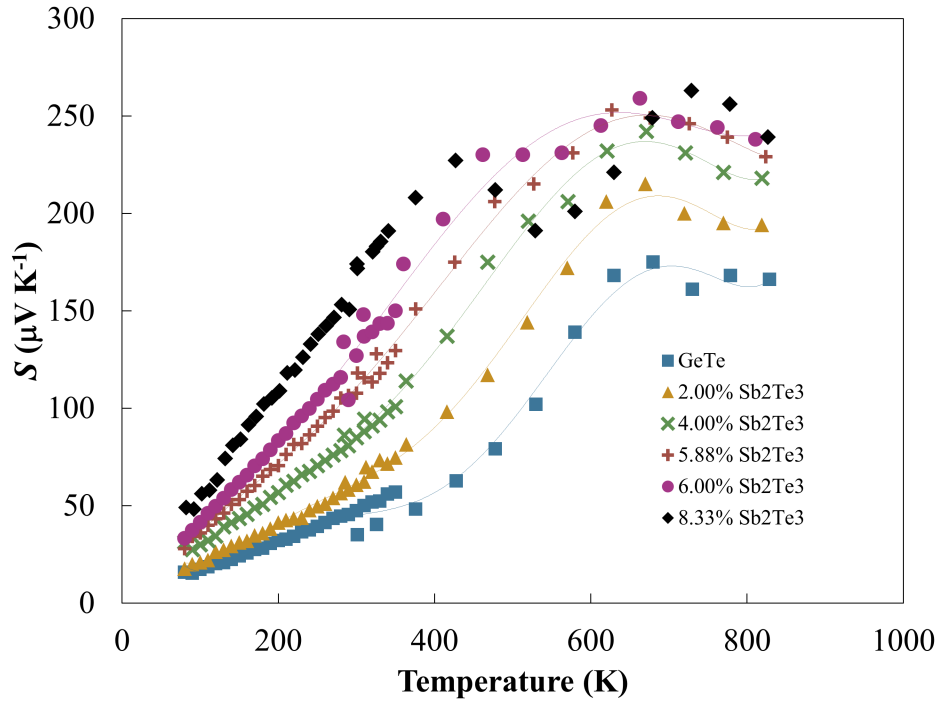

Figure 4.4: Seebeck coefficient versus temperature for $(GeTe)_{1-x}(Sb_2Te_3)_x$, where x varies from 0%, 2%, 4%, 5.9%, 6%, and 8.3% Sb_2Te_3.

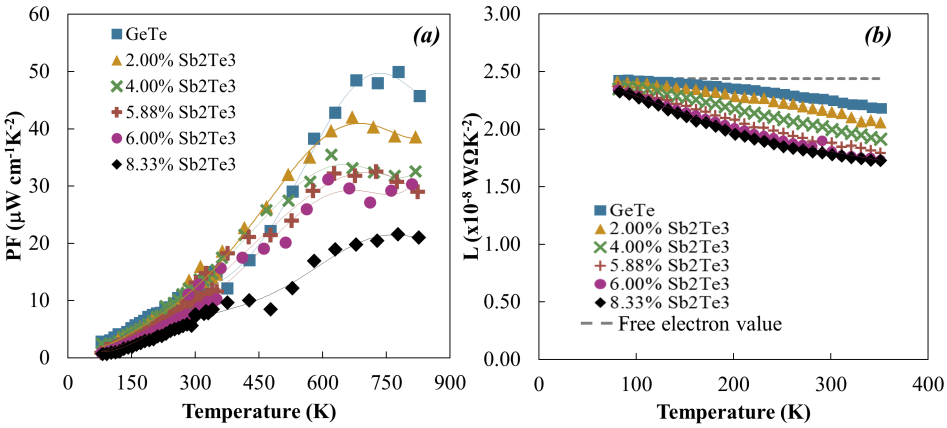

Figure 4.5: Power factor, (a) and calculated Lorenz number, (b) versus temperature for $(GeTe)_{1-x}(Sb_2Te_3)_x$, where x varies from 0%, 2%, 4%, 5.9%, 6%, and 8.3% Sb_2Te_3.

The linear behavior of the Seebeck coefficient below the phase transition temperature allows for a more accurate determination of the Lorenz number, which is in turn used to calculate the electronic thermal conductivity. Using a single parabolic band approximation,

the Seebeck coefficient was numerically fit and used to determine the reduced Fermi energy ($\eta = \frac{E_f}{k_B T}$) using equation (1.36). After calculating η, the Lorenz number was then calculated using equation (1.48). The calculated Lorenz number for $(GeTe)_{1-x}(Sb_2Te_3)_x$ significantly deviates from the free electron value, as can be seen in Figure 4.5(b). The thermal conductivity was decreased as the Sb_2Te_3 concentration was increased. This is due to the diminishing electronic and lattice contributions to thermal conductivity, as can be seen in Figure 4.6. It is believed that the vacancies introduced with Sb_2Te_3 substitution scatter phonons and caused the decrease in lattice thermal conductivity.

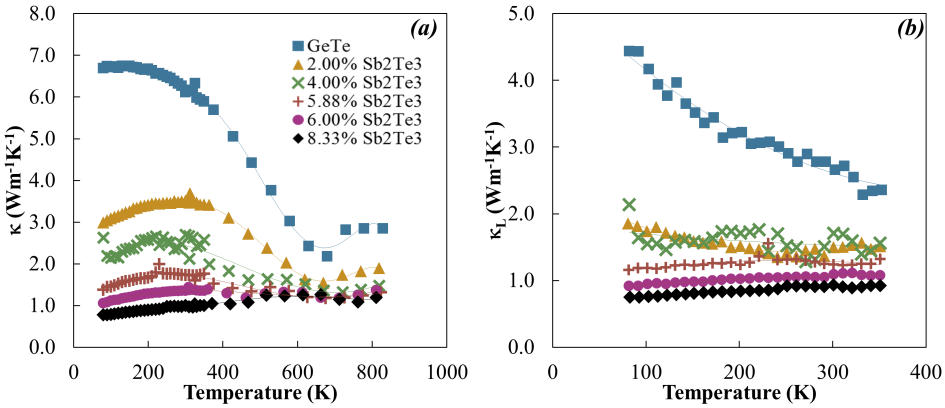

Figure 4.6: Thermal conductivity, (a), and lattice thermal conductivity, (b) versus temperature for $(GeTe)_{1-x}(Sb_2Te_3)_x$, where x varies from 0%, 2%, 4%, 5.9%, 6%, and 8.3% Sb_2Te_3.

By substituting Sb_2Te_3 for GeTe a 46% increase in ZT is achieved. The ZT value at 723K shows a turnover with increasing Sb_2Te_3 concentration, as can be seen in Figure 4.7, with the highest ZT being displayed in the 5.9% Sb_2Te_3 doped compound, otherwise written as $Ge_{17}Sb_2Te_{20}$. This large enhancement in ZT is explained primarily by the introduction of vacancies, which introduced new scattering sites. This resulted in a large increase in the electrical resistivity and Seebeck coefficient, but also allowed for a significant decrease in thermal conductivity.

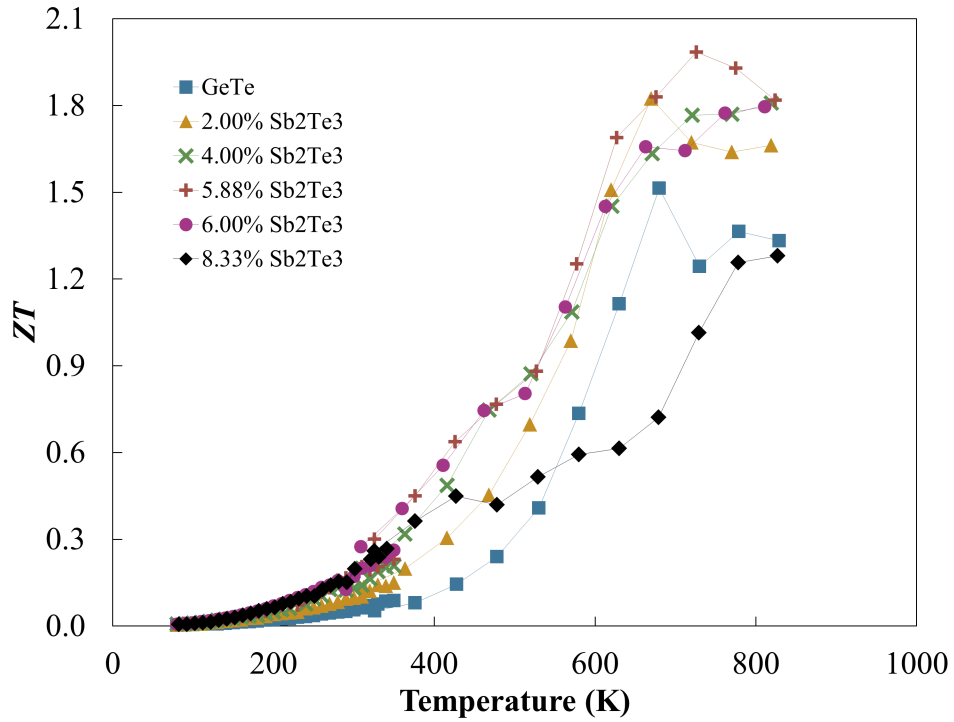

Figure 4.7: ZT versus temperature for $(GeTe)_{1-x}(Sb_2Te_3)_x$, where x varies from 0%, 2%, 4%, 5.9%, 6%, and 8.3% Sb_2Te_3.

4.3 Conclusion

From the ternary phase diagram of Ge, Sb, and Te, the psuedo-binary alloys of GeTe and Sb_2Te_3 yield known state of the art phase change materials for nonvolatile memory storage. From the work seen here, and others since the 1990s, it is clear that $(GeTe)_{1-x}(Sb_2Te_3)_x$ compounds additionally hold promise for thermoelectric power generation applications. It was found that increasing the Sb_2Te_3 content increased the concentration of vacancies within these compounds. ZT values greater than 1.5 were seen for a number of the GeTe rich alloys. The following chapters will outline the various chemical and materials techniques used to optimize the synthesis of Ge_4SbTe_5 and $Ge_{17}Sb_2Te_{20}$ and enhance the ZT, all while striving for a more fundamental understanding of the materials.

Chapter 5

Ge_4SbTe_5

Ge_4SbTe_5 is a phase change material which is located just off of the $GeTe-Sb_2Te_3$ tie-line. This compound is currently used for high-definition DVDs and Blu-ray devices, but unlike other phase change materials found on the aforementioned tie-line it contains no vacancies.[115] It exists in a metastable rocksalt ($Fm\bar{3}m$) phase at room temperature with Ge and Sb randomly assorted on the cation site and Te atoms occupying the anion site, as can be seen in Figure 5.1, which was created using VESTA.[91]

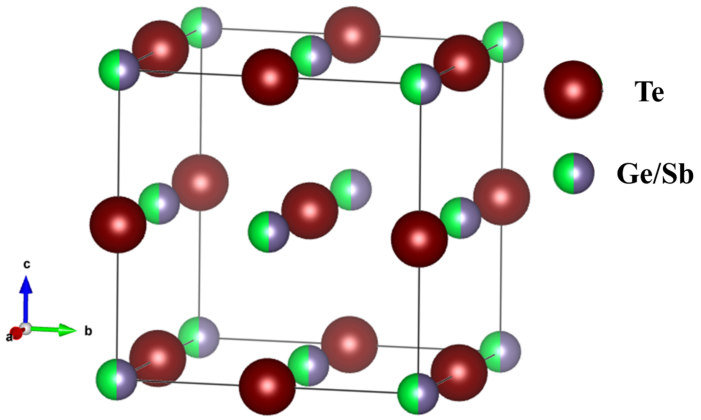

Figure 5.1: Rocksalt ($Fm\bar{3}m$) crystal structure of Ge_4SbTe_5, with Ge and Sb randomly occupying the cation site and Te on the anion site.

Unlike other state-of-the-art phase change materials Ge_4SbTe_5 contains no vacancies in the rocksalt unit cell, and with a band gap of approximately 0.7 eV, it was believed that it would exhibit interesting thermoelectric properties in the medium temperature regime (400-600K).[115] The following sections will outline the synthesis and various doping and substitutional approaches used to study this compound.

5.1 Synthesis and Crystal Structure

Samples of Ge_4SbTe_5 were synthesized by placing stoichiometric amounts of Ge (99.9999 %, Alfa Aesar, zone-refined ingot), Sb (99.999%, Alfa Aesar, shot 6mm and down) and Te (99.999+%, Alfa Aesar, lump) in silica ampoules. The ampoules were evacuated to approximately 10^{-5} Torr to prevent oxidation during synthesis. Samples were then melted by heating to 900°C at a heating rate of 2°C/min. The ingot obtained was then ballmilled for 5min in a stainless steel jar using a SPEX-5000 vibratory mill. The sample was densified using spark plasma sintering (SPS) at 400°C for 15min under 40MPa of uniaxial pressure. Volumetric density was measured using the Archimedes method. The sintered pellets, which had density greater than 95% theoretical density, were then cut for thermoelectric measurements and characterization.

Room temperature X-ray diffraction was used to verify the crystal structure of Ge_4SbTe_5. The lattice parameter was found by assigning the allowed diffraction planes to each peak in the pattern and calculating the interplanar spacing, which is related to the angle of diffraction by Bragg's law of diffraction: [108]

$$n\lambda = 2dsin\theta \tag{5.1}$$

where $\lambda = 1.5418$Å for CuKα radiation. The interplanar spacing is related to the unit cell parameter and Miller indices, for cubic crystal structures, via equation (2.4). The diffraction pattern with (hkl) peaks labeled can be seen in Figure 5.2. The calculated lattice parameter was 5.95 Å for Ge_4SbTe_5.

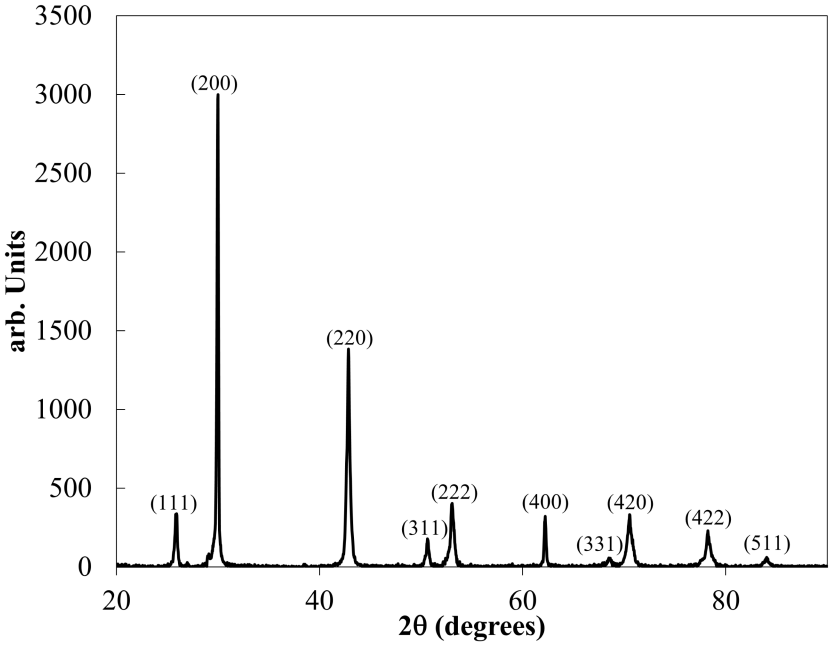

Figure 5.2: X-ray diffraction pattern of Ge_4SbTe_5 with peaks labeled by their respective miller indices.

This rocksalt phase, however is metastable and upon heating undergoes a phase transformation to a rhombohedral, or distorted cubic, structure. This high temperature phase belongs to the space group $R\bar{3}m$, also known as the tetradymite structure. Similar to the layered structures of Bi_2Te_3 and Sb_2Te_3 the high temperature phase of Ge_4SbTe_5 exists with alternating layers of Ge,Sb, and Te with inter-penetrating layers of vacancies. Temperature dependent X-ray diffraction of Ge_4SbTe_5 in the temperature range of $50°C - 450°C$ was performed at Oak Ridge National Laboratory, the result of which can be seen in Figure 5.3.

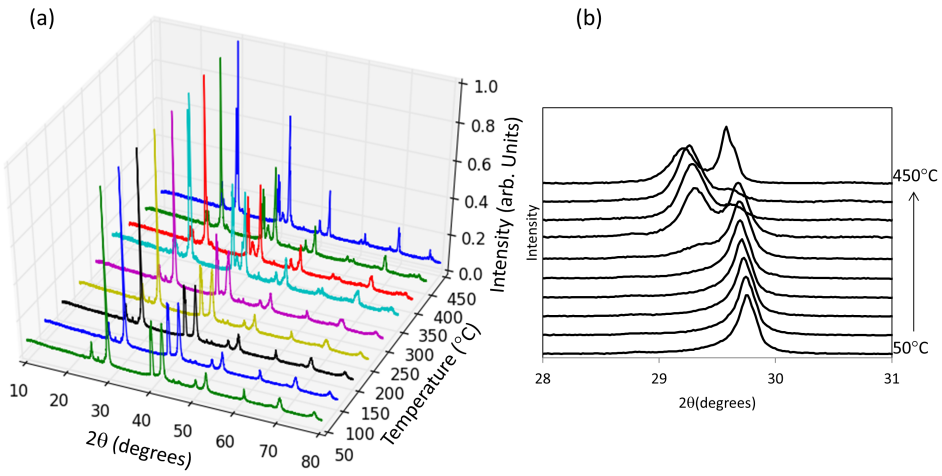

Figure 5.3: (a)Temperature dependent X-ray diffraction patterns for Ge_4SbTe_5. (b) shows the cubic *(111)* peak splitting at the phase transition temperature as the cubic crystal structure transforms to rhombohedral.

The phase transformation is structural in nature, but also corresponds to the Curie temperature of Ge_4SbTe_5. The ferroelectric nature of Ge_4SbTe_5, and other alloys of GeTe and Sb_2Te_3, which exists at low temperature, stems from the high levels of resonance bonding, as aforementioned. DSC measurements of Ge_4SbTe_5 as a function of temperature can be seen in Figure 6.1. An endothermic peak was observed in the heat capacity at 523K, which corresponds to the structural phase transition.

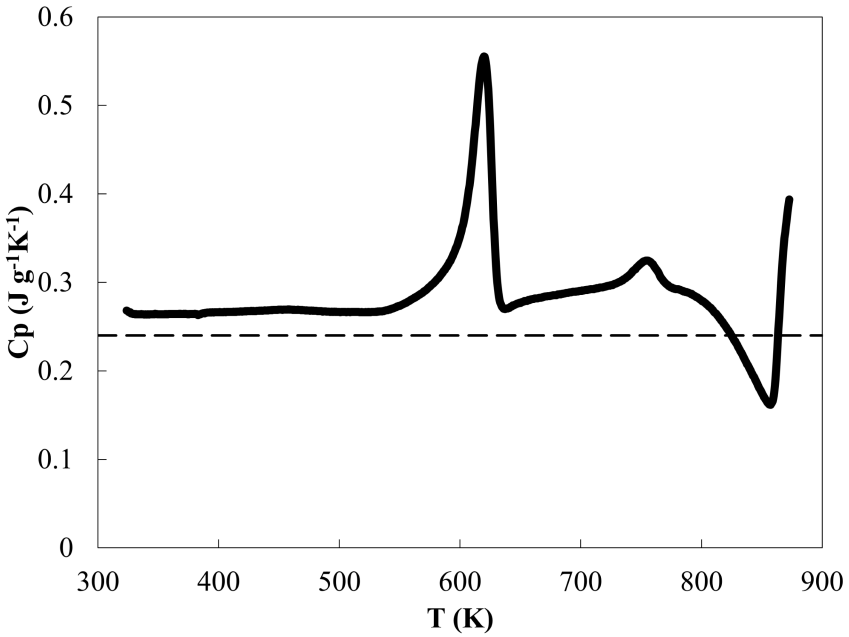

Figure 5.4: Specific heat, as determined by DSC, versus temperature for Ge_4SbTe_5, with the Dulong-Petit value represented by a dashed line.

The phase transformation is also considered an Anderson localization transition, in which a material goes from displaying semiconductor like carrier transport to metallic transport. The electrical resistivity reflects this behavior with a sharp decrease from approximately 8mΩ cm to 2mΩ cm at 523K, as can be seen in Figure 5.5(a). The Seebeck coefficient reflects similar behavior with a slight dip at the phase transition temperature, but continues to rise thereafter to values around 250μVK^{-1} (Figure 5.5(b)). The result of this electronic phase transition is an increase in power factor to values well above 20$\mu Wcm^{-1}K^{-2}$, which can be seen in Figure 5.5(c)

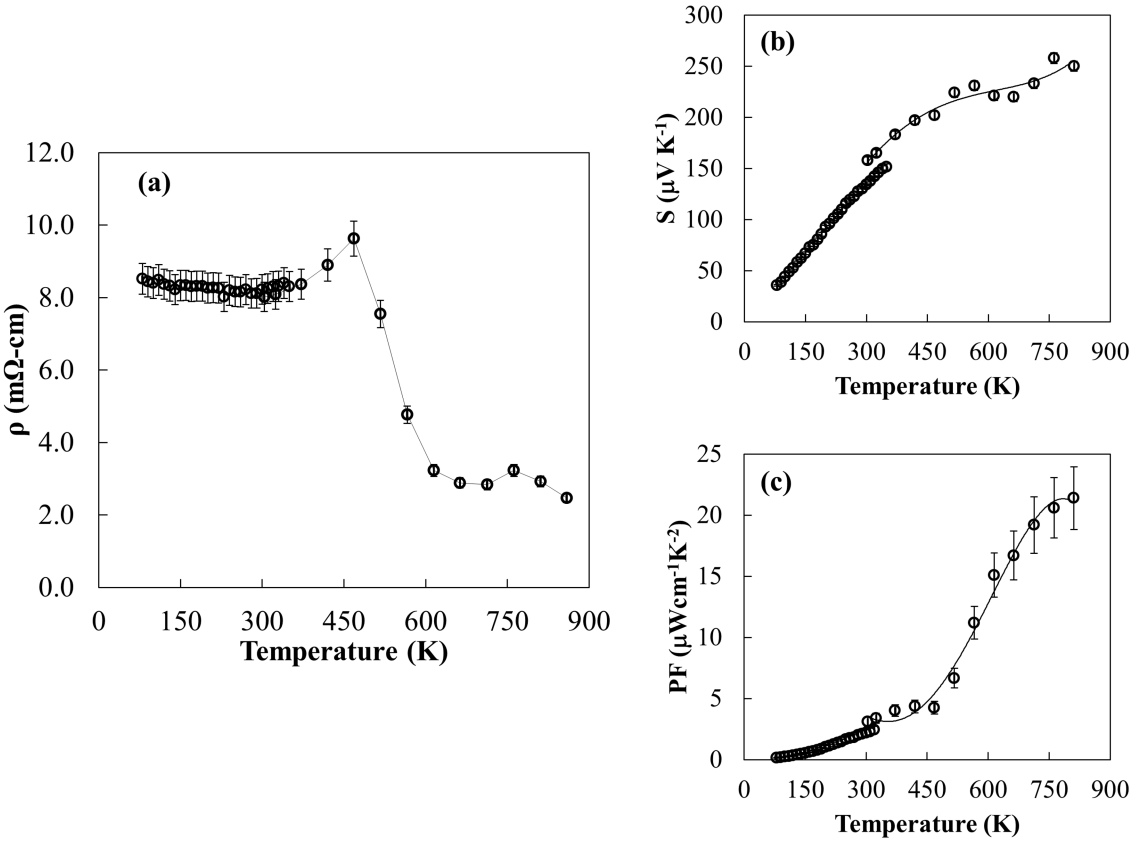

Figure 5.5: (a) Electrical resistivity versus temperature, (b) Seebeck coefficient versus temperature, and (d) Power factor versus temperature for Ge_4SbTe_5.

The thermal conductivity maintains values approximately equal to $1 \mathrm{Wm}^{-1}\mathrm{K}^{-1}$, except for an increase around the phase transition temperature due the spike in specific heat. The thermal conductivity as a function of temperature can be seen in Figure 5.6(a). Because of the large power factor values and low thermal conductivity the ZT displays values greater than unity, reaching 1.5 around 800K. As can be seen in Figure 5.6(b), the best thermoelectric performance is seen at temperatures above the phase transformation.

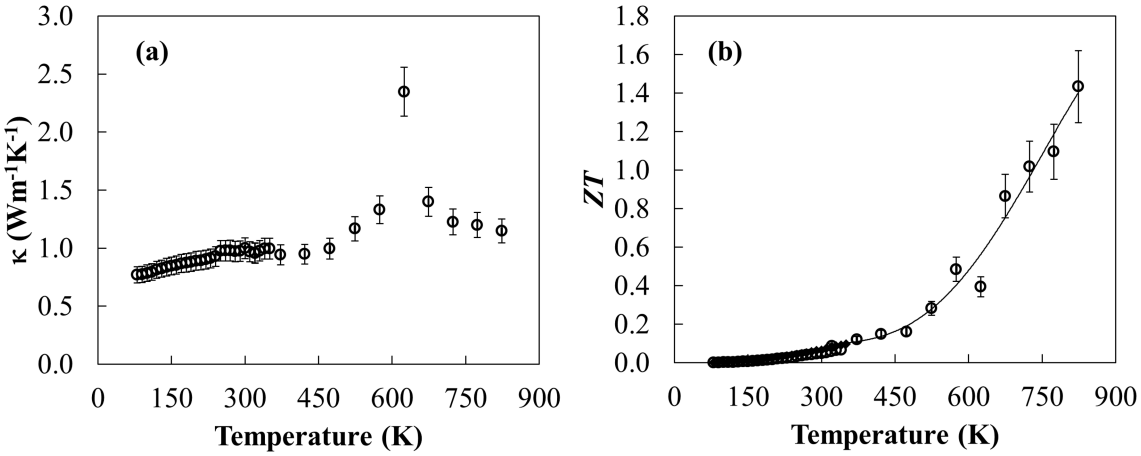

Figure 5.6: (a) Thermal conductivity versus temperature and (b) ZT versus temperature for Ge_4SbTe_5.

These values of ZT are competitive with state of the art thermoelectric materials, as can be seen in Figure 6.5.[116] Little research has been conducted on bulk Ge_4SbTe_5. With low thermal conductivity and high power factor it was believed that Ge_4SbTe_5 would be an ideal candidate for study. The following projects aimed to engineer the thermoelectric properties through various doping and substitutional techniques.

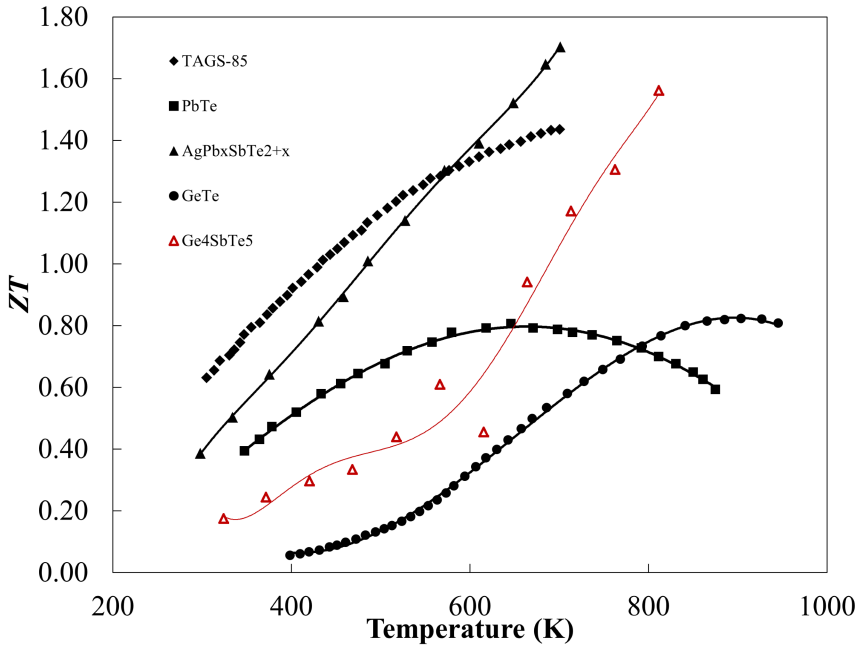

Figure 5.7: ZT versus temperature for a number of today's state of the art chalcogenide thermoelectric materials, with Ge_4SbTe_5 showing competitive values.[117, 118, 119]

5.2 Atomic Substitutions

Isovalent atomic substitutions are an effective way to improve the ZT of thermoelectric materials. As aforementioned, substituting atoms which have the same valency but different mass increases the scattering of heat-carrying phonons. This has been shown to be an effective way to lower the lattice component of thermal conductivity, and with a matching valence configuration, no change in the carrier concentration should be observed. It should be noted, however, that the mass and electronegativity difference of substituting isovalent atoms can induce additional scattering on the charge carriers, which would also lower charge carrier mobility. In the following sections the thermoelectric properties of two solid solutions on Ge_4SbTe_5 will be presented, namely $Ge_{4-x}Sn_xSbTe_5$ and $Ge_4Sb_{1-x}Bi_xTe_5$.

5.2.1 $Ge_{4-x}Sn_xSbTe_5$

Tin represented a logical choice as an atomic substitution for the Ge site in Ge_4SbTe_5. Sn is inexpensive, relatively abundant, and nontoxic to humans and the environment. Buller, *et al* recently studied the effects of Sn for Ge substitution and Se for Te substitution in thin-films of $Ge_8Sb_2Te_{11}$. They found that these substitutions affected the electronic bandgap and altered the overall electrical properties.[120] Welzmiller, *et al* studied $Ge_2Sb_2Te_5$ and the effects which Sn substitution had on the thermoelectric properties.[121] More recently Welzmiller studied Cd doping in $(GeTe)_m(Sb_2Te_3)$ alloys and $(SnTe)_m(Sb_2Te_3)$ alloys.[122] Additionally, the atomic mass of Sn is greater than that of Ge, so it was believed that this isovalent substitution would provide additional phonon scattering without a detrimental decrease to the impressive electrical properties of Ge_4SbTe_5.

5.2.1.1 Experimental

Samples of $Ge_{4-x}Sn_xSbTe_5$ were synthesized using the method described in earlier sections, where stoichiometric amounts of Ge, Sn, Sb, and Te were massed out and placed in 10mm silica ampoules. The ampoules were then evacuated to approximately $10^{-5}Torr$ and sealed. The samples were heated to 900°C at a rate of 2°C/min, held for 12 hours, and water quenched. Sn was substituted for Ge in 12.5mol % intervals, which for $Ge_{4-x}Sn_xSbTe_5$ corresponds to x=0, 0.5, 1.0, 1.5, 2.0, 2.5, 3.0, 3.5, and 4.0. X-ray diffraction was measured at room temperature on all samples, the patterns of which can be seen in Figure 5.8. As Sn was substituted some of the diffraction peaks either decreased or increased in intensity, which was explained by the difference in structure factor between Ge and Sn. The diffraction peaks showed a uniform shift to lower 2θ with increasing Sn substitution. This is consistent with an increase in the cubic lattice parameter of the unit cell. To calculate the lattice

parameter a Si standard was used during X-ray diffraction to correct for 2θ offset during the measurements. The calculated lattice parameter can be seen in Figure 5.9. There is a linear increase in the lattice parameter of the rocksalt unit cell with increasing Sn substitution concentration, which is in agreement with Vegard's law; essentially a rule of mixtures for the lattice parameter of a solid solution.[123]

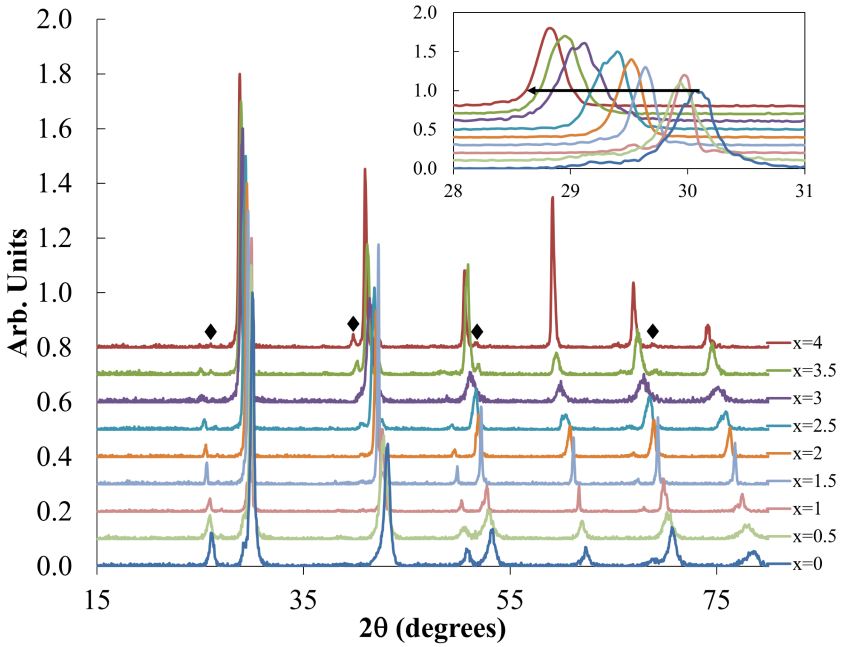

Figure 5.8: X-ray Diffraction pattern of $Ge_{4-x}Sn_xSbTe_5$, where x=0, 0.5, 1.0, 1.5, 2.0, 2.5, 3.0, 3.5, and 4.0. A shift in diffraction peaks to lower 2θ can be seen with increasing Sn substitution, which corresponds to an increase in lattice parameter. Impurity peaks, which were found to be elemental Sb, are marked by a diamond.

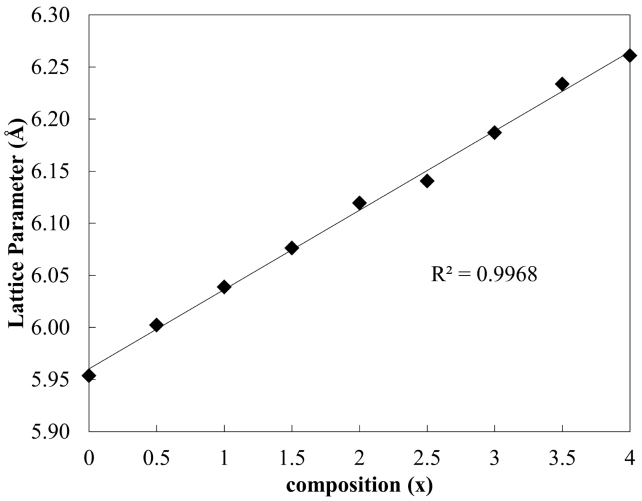

Figure 5.9: Lattice Parameter (Å) versus Sn concentration for $Ge_{4-x}Sn_xSbTe_5$. A least-squares method was used to apply the trendline. The linear behavior agrees with Vegard's law.

With the increase of Sn substitution, secondary phases of elemental Sb were observed in the X-ray diffraction patterns and SEM/EDS (PDF#98-000-0095). Despite the presence of these Sb impurities the rocksalt crystal structure was maintained. The stoichiometry was therefore verified using SEM/EDS, which can be seen in Table 5.1.

Table 5.1: Using SEM/EDS the actual composition of Sn substituted samples of Ge_4SbTe_5 were measured, seen here as atomic percent.

$Ge_{4-x}Sn_xSbTe_5$	Actual Composition (atomic %)			
	Ge	Sn	Sb	Te
x=0	41.0	-	10.5	48.6
x=1	29.8	10.6	10.7	48.9
x=2	19.6	21.4	10.4	48.6
x=3	10.3	31.3	10.4	47.9
x=4	-	41.8	10.3	47.9

All samples were ball-milled in a stainless steel ball mill jar for 5min and densified using SPS at 350°C for 15min under 40MPa of pressure. The sintering temperature was decreased

from previous samples of Ge_4SbTe_5 to account for substantial cracking observed in high Sn concentration substituted samples. The pellets were then polished and cut for thermoelectric measurements.

5.2.1.2 Results and Discussion

With successful substitution of Sn for Ge it was expected that the electrical resistivity would increase due to increased charge carrier scattering, however the electrical resistivity was decreased as a function of Sn concentration. This decrease in the electrical resistivity is indicative of a doping effect, as was reflected in the Seebeck coefficient. However, because Sn should substitute for Ge without a change in the valence configuration, it was hypothesized that the substitution caused a decrease in the band gap of Ge_4SbTe_5. The variation of bandgap with alloying in chalcogenide based compounds is a well known phenomenon. If, for instance, one was to alloy two binary compounds, AB and BC, the optical band gap should vary quadratically with composition, as can be seen in equation (5.2).[124]

$$E_g(x) = [x\epsilon_{AC} + (1-x)\epsilon_{BC}] - bx(1-x)] \tag{5.2}$$

where b is defined as the bowing parameter.[124, 125] The electrical resistivity versus temperature (*80K-823K*) and Seebeck coefficient versus temperature for all Sn substituted samples can be seen in Figure 5.10 and Figure 5.11, respectively. A decrease in electrical resistivity and Seebeck coefficient was observed, which in turn resulted in a decreased power factor. However, the original motivation for introducing the atomic substitutions was to induce additional phonon scattering and thereby decrease lattice thermal conductivity.

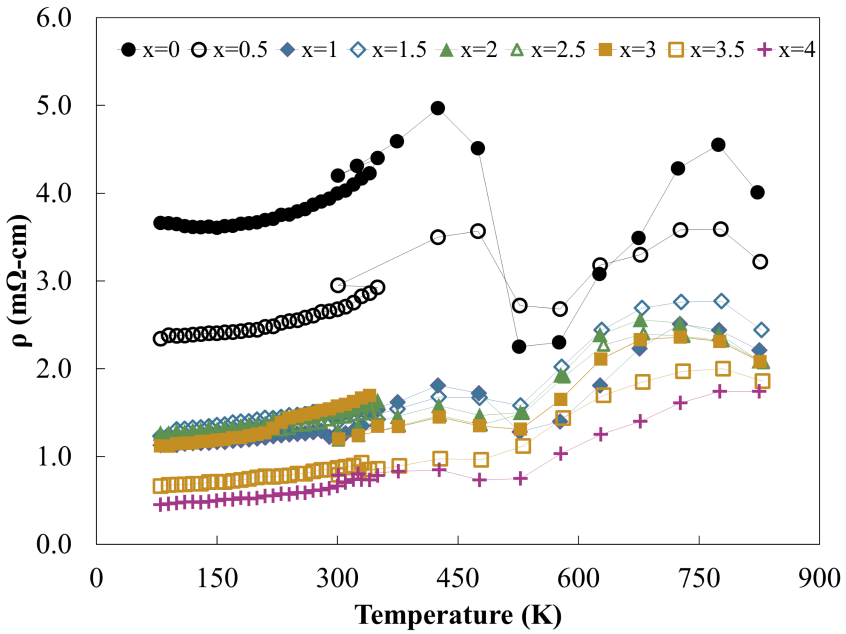

Figure 5.10: Electrical resistivity versus temperature for $Ge_{4-x}Sn_xSbTe_5$ where x=0, 0.5, 1, 1.5, 2, 2.5, 3, 3.5, and 4.

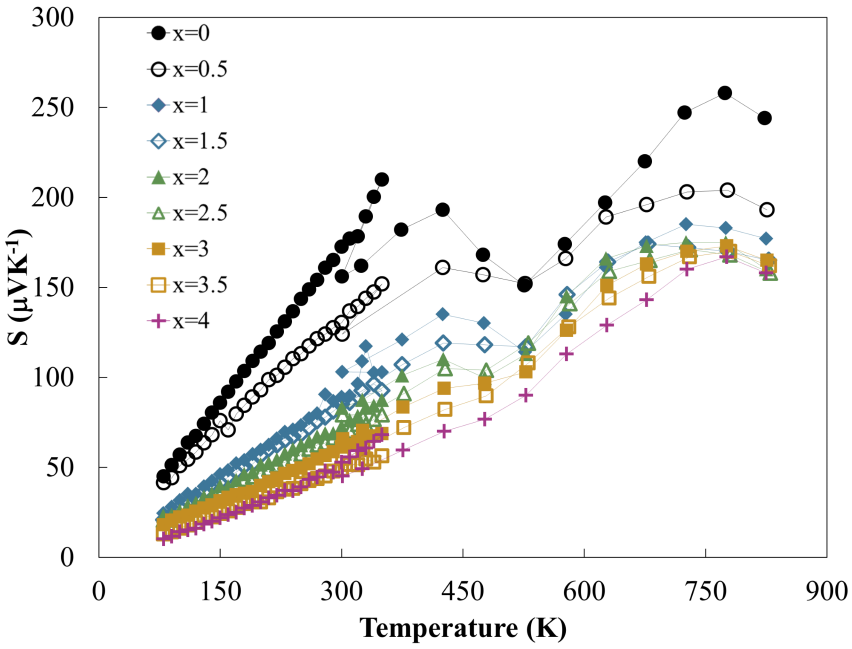

Figure 5.11: Seebeck coefficient versus temperature for $Ge_{4-x}Sn_xSbTe_5$ where x=0, 0.5, 1, 1.5, 2, 2.5, 3, 3.5, and 4.

A decrease in the lattice thermal conductivity at room temperature (300K) was observed,

while at high temperature (723K) little to no decrease in the lattice contribution to thermal conductivity was observed. A plot of the thermal conductivity at 300K and 723K versus % Sn substitution, thermal conductivity versus temperature, and a closer look at the high temperature thermal conductivity can be seen in Figure 5.12.

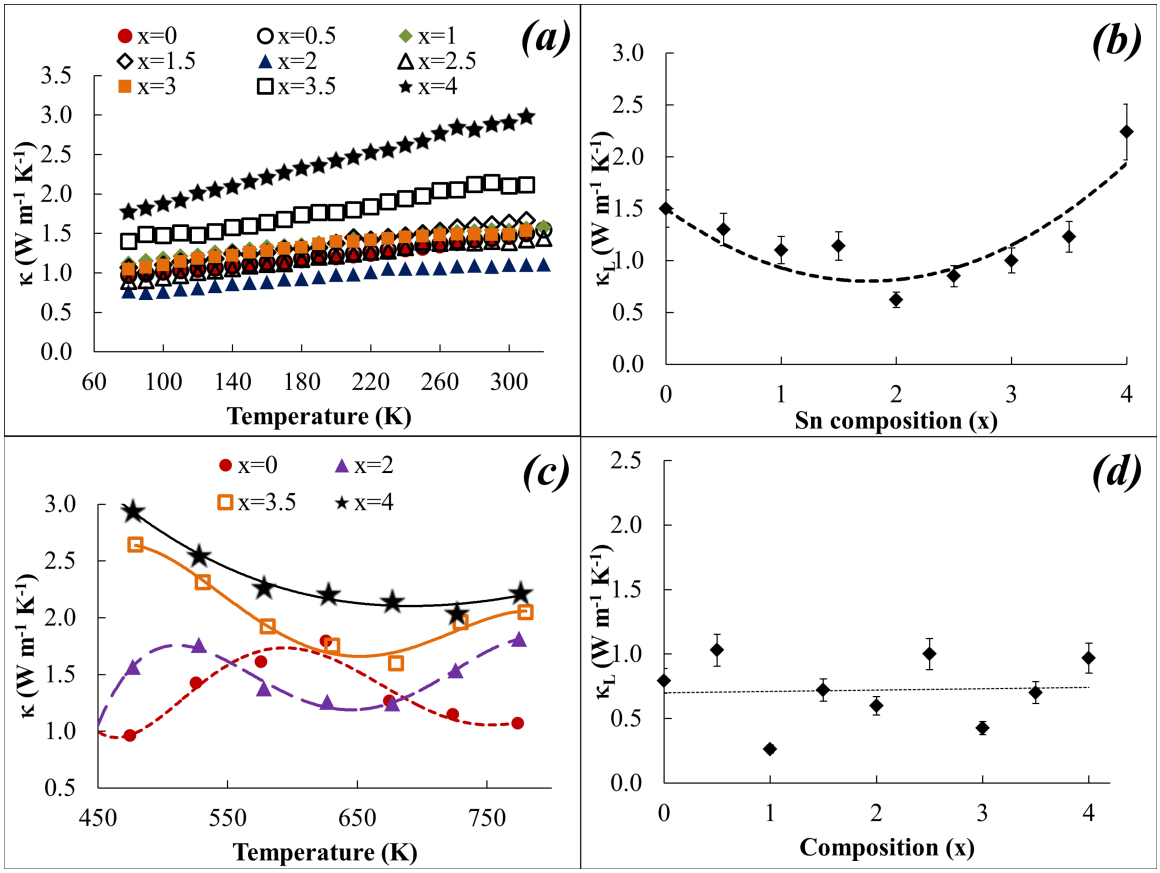

Figure 5.12: ***(a)*** Thermal conductivity versus temperature for all Sn substituted samples in the temperature range of 80K to 320K. ***(b)*** Lattice thermal conductivity at 300K versus stoichiometric amount of substituted Sn. ***(c)*** Thermal conductivity at 723K for $25\%, 50\%, 82.5\%, and 100\%$ Sn substitution. ***(d)*** Lattice thermal conductivity at 723K versus stoichiometric amount of substituted Sn.

For temperatures well above the Debye temperature for a given material the dominant scattering mechanism becomes phonon-phonon scattering, or Umklapp scattering, as was explained in Chapter 1. The Debye temperature of Ge_4SbTe_5 can be approximated using the relation developed by Slack, which states that for a given crystal structure the product

of the average atomic mass, $\bar{M}$, the average volume per atom, δ, and the Debye temperature, θ (equation (5.3)) is constant.[126]

$$\bar{M}\delta\theta^3 = constant \tag{5.3}$$

For the rocksalt crystal structure of Ge_4SbTe_5 the Debye temperature was found to be 126K. Therefore the lack of substantial reduction in lattice thermal conductivity at high temperature is consistent with the qualitative understanding that Umklapp scattering should be dominant. The lack of decrease in the lattice thermal conductivity at high temperature ultimately resulted in an increase in the total thermal conductivity because of the increasing electronic contribution, as can be seen in Figure 5.12.

5.2.1.3 Conclusion

The original motivation for this work was based on the premise that Sn substituted for Ge in Ge_4SbTe_5 would decrease thermal conductivity and increase the overall ZT. However it was observed that the Sn substitution led to a decrease in the electrical resistivity and Seebeck coefficient, which was believed to be due to the contracted bandgap. This change in bandgap also led to a substantial increase in the electronic contribution to thermal conductivity. The ZT was decreased for all samples with Sn substitution greater than 25%. This is mainly attributed to the increased thermal conductivity.

Though this study was not effective in enhancing the thermoelectric performance of Ge_4SbTe_5, a new understanding of the relation between group IV elemental substitutions and the electrical properties was achieved. In the following section a study on the thermoelectric properties of $Ge_4Sb_{1-x}Bi_xTe_5$, a solid solution on the Sb site, will be presented.

5.2.2 $Ge_4Sb_{1-x}Bi_xTe_5$

In 1999 Kuznetsov, *et al* studied $GeBi_4Te_7$ and found that stoichiometry was an important factor in altering the Seebeck coefficient and electrical resistivity of GeTe-Bi_2Te_3 compounds.[127] This was one of the first examples of studying the thermoelectric effects on Bi in GeTe phase change materials. Matsunaga, *et al* studied the stability and formation of GeTe-Bi_2Te_3 alloys.[128] Shelimova, *et al* studied these alloys and found that the charge carrier type varied based on the specific composition synthesized.[129] More recently Wu, *et al* found that small amounts of Bi_2Te_3 substitution in GeTe enhanced the ZT by more than 100%. The substitution of Bi for Sb, especially for Ge_4SbTe_5, has yet to be studied for thermoelectric applications although these compounds have been researched for various memory applications.[130] The following section is a description of the synthesis and thermoelectric characterization of bulk $Ge_4Sb_{1-x}Bi_xTe_5$.

5.2.2.1 Experimental

Stoichiometric amounts of Ge, Sb, Te, and Bi (99.999%, Alfa Aesar) were sealed in evacuated silica ampoules. The samples were melted at 900°C for 12h and water quenched. The resulting ingots were ball milled and sintered using SPS at 400°C for 15min under 40MPa of pressure. Samples were cut from the sintered pellets wich were then used for structural and thermoelectric characterization, the specific details of which were described in previous sections.

5.2.2.2 Results and Discussion

The X-ray diffraction patterns revealed a shift in the 2θ position of the *(hkl)* peaks. This shift in 2θ is indicative of a change in the lattice parameter. Substituting Sb with the larger

Bi atom resulted in an increase in the lattice parameter, as can be seen in Figure 5.13.

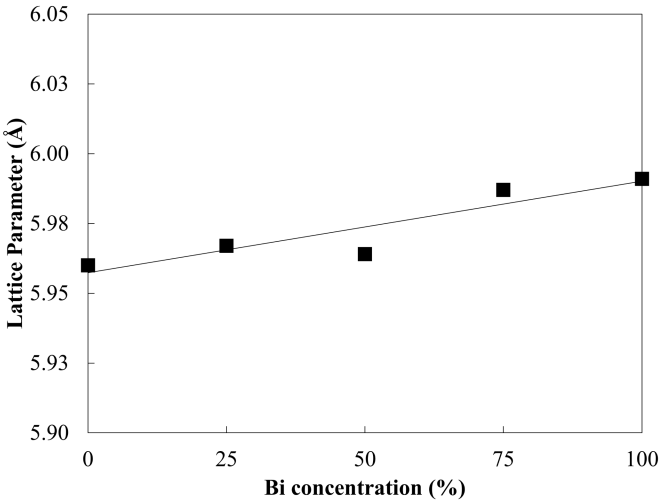

Figure 5.13: Lattice parameter versus Bi composition in $Ge_4Sb_{1-x}Bi_xTe_5$.

Differential scanning calorimetry (DSC) was performed to analyze the specific heat. With increasing Bi concentration the melting point was found to decrease to approximately 783K. The phase transition temperature also decreased from 620K for Ge_4SbTe_5 to 601K for Ge_4BiTe_5. The C_p versus temperature and phase transition temperature, T_C, versus Bi content can be seen in Figure 5.14.

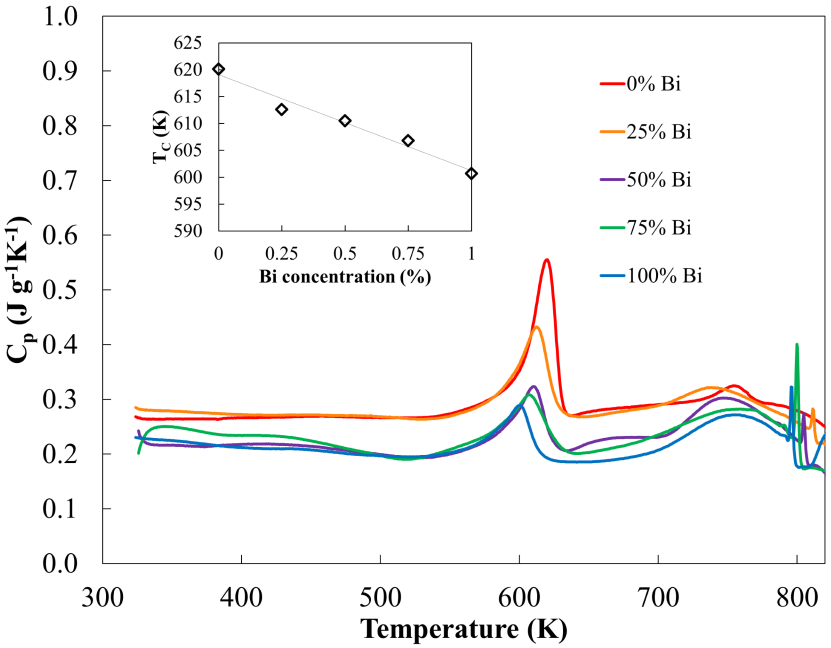

Figure 5.14: Specific heat versus temperature for $Ge_4Sb_{1-x}Bi_xTe_5$, where $x = 0, 0.25, 0.50, 0.75, 1.0$. Phase transition temperature versus percent Bi can be seen in the inset plot.

The primary goal of substituting Sb with Bi was to scatter heat-carrying phonons and lower the lattice contribution to thermal conductivity. The thermal conductivity, which was calculated using the volumetric density, specific heat, and thermal diffusivity shows a decreasing trend with increasing Bi concentration. The lattice thermal conductivity was estimated using the Weidemann-Franz law to calculate the electronic contribution and subtracting from the total thermal conductivity. The result of the Bi substitution was a general decrease in the lattice thermal conductivity and the total thermal conductivity, as can be seen in Figure 5.15.

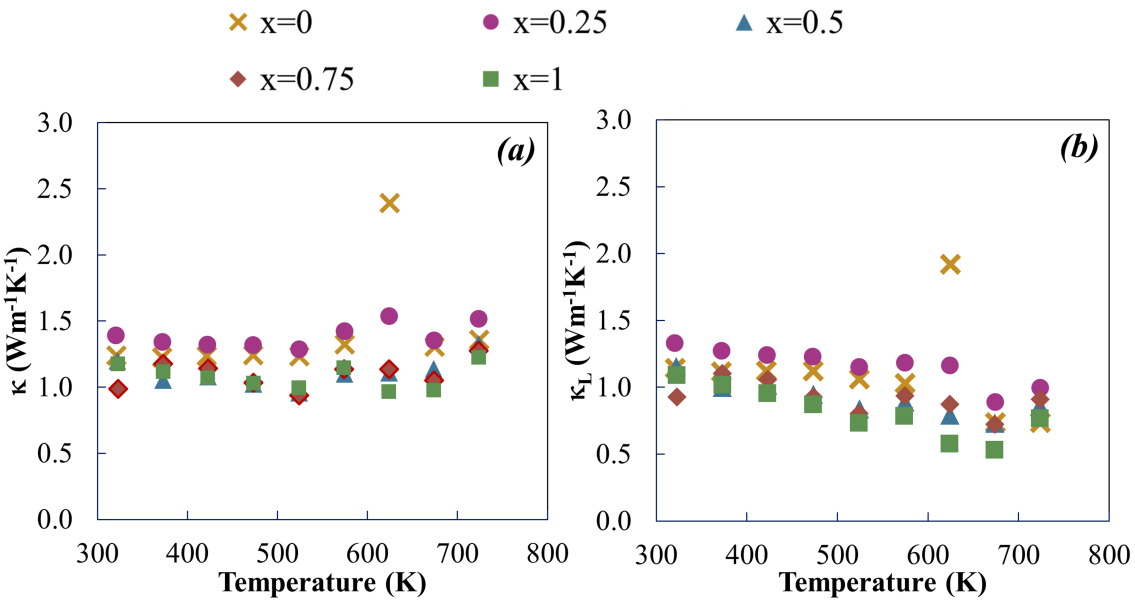

Figure 5.15: (a) Thermal conductivity versus temperature for $Ge_4Sb_{1-x}Bi_xTe_5$, where $x = 0, 0.25, 0.50, 0.75, 1.0$. (b) Lattice thermal conductivity versus temperature, dashed line marking the $1/T$ temperature dependence of Umklapp scattering.

As was noticed with $Ge_{4-x}Sn_xSbTe_5$, the Seebeck coefficient decreased with increased Bi substitution, as can be seen in Figure 5.16. The decrease in Seebeck coefficient is most likely due to a narrowing of the electronic bandgap, which would shift the Fermi energy and yield higher charge carrier concentrations.

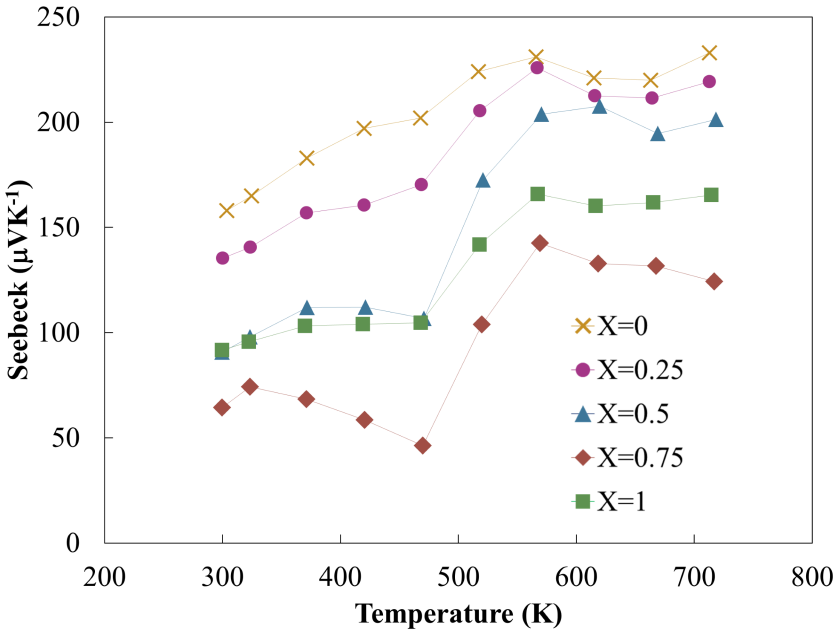

Figure 5.16: Seebeck coefficient versus temperature for $Ge_4Sb_{1-x}Bi_xTe_5$, where $x = 0, 0.25, 0.50, 0.75, 1.0$.

Unlike in the case of $Ge_{4-x}Sn_xSbTe_5$, the electrical resistivity was not decreased with the substitution of Bi. At temperatures below the phase transition the electrical resistivity is increased to 17mΩ cm for 50% Bi substitution and decreased with further substitution to values approximately equal to 13mΩ cm for Ge_4BiTe_5. The electrical resistivity versus temperature can be seen in Figure 5.17.

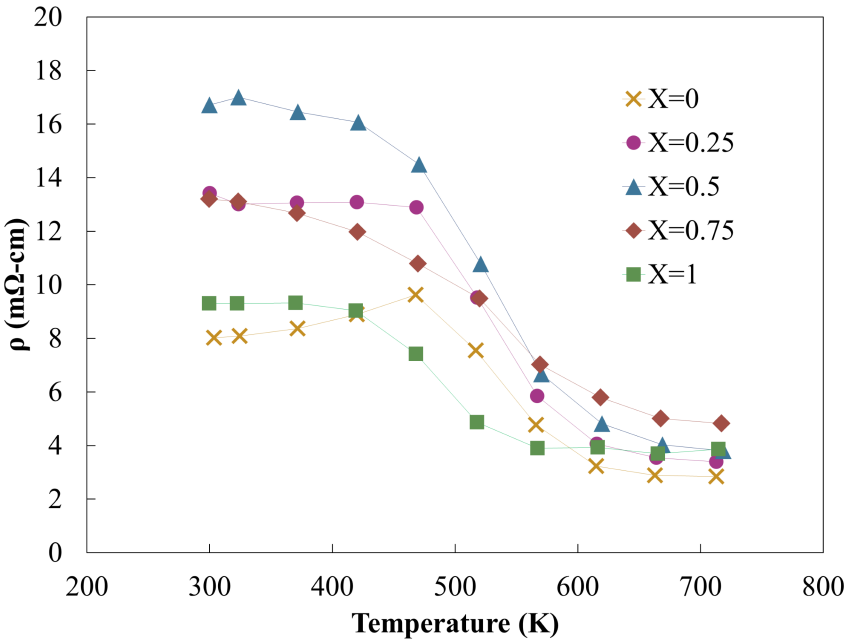

Figure 5.17: Electrical resistivity versus temperature for $Ge_4Sb_{1-x}Bi_xTe_5$, where $x = 0, 0.25, 0.50, 0.75, 1.0$.

The electrical resistivity follows a trend that is consistent with traditional alloys. As a solid solution is formed the solute atoms scatter charge carriers. Recall that according to Matthiesen's rule the scattering relaxation rates for the various processes which contribute to the electrical resistivity sum as:

$$\tau^{-1} = \tau_T^{-1} + \tau_I^{-1} + ... \tag{5.4}$$

τ_T is the relaxation time associated with scattering from thermal vibrations, and τ_I is the relaxation time associated with scattering from positively charged ions in the crystal lattice. The scattering relaxation time which is shortest contributes the most. As more disorder is introduced into the system by means of randomly distributed solute atoms the scattering relaxation time associated with ions will decrease, thereby becoming more prominent in affecting electronic transport. Nordheim's rule relates the resistivity associated with

impurity atoms to the atomic fraction X of the solute atoms and the Nordheim coefficient, C. When Matthiesen's rule and Nordheim's rule are combined the resistivity of an alloy can be estimated with knowledge of the matrix resistivity ρ_{matrix} and the Nordheim coefficient according to equation (5.5).[12]

$$\rho = \rho_{matrix} + CX(1 - X) \tag{5.5}$$

The electrical resistivity of $Ge_4Sb_{1-x}Bi_xTe_5$ displays this quadratic behavior, as can be seen in Figure 5.18.

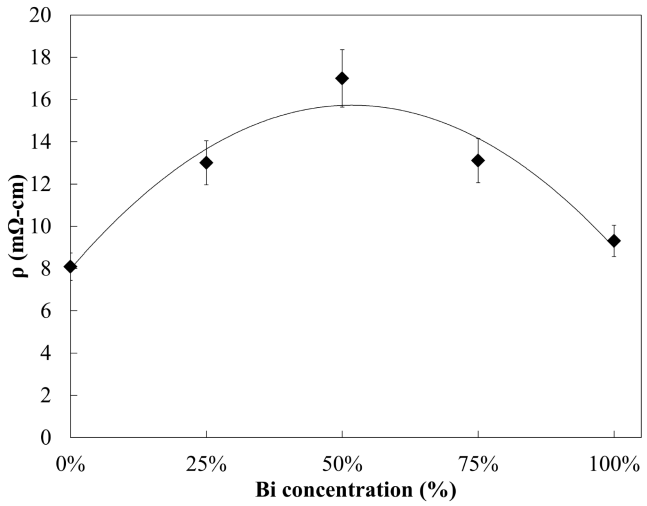

Figure 5.18: Room temperature (300K) electrical resistivity versus %Bi substituted with 8%. The parabolic nature is indicative of alloy scattering, as explained by Nordheim's rule. The trendline was generated using a least squares fit without knowledge of the Nordheim coefficient of Ge_4SbTe_5.

5.2.2.3 Conclusion

Because of the increase in electrical resistivity and decrease in Seebeck coefficient the power factor was decreased to values below 5µWcm^{-1}K^{-2} above the phase transition temperature. Despite a decrease in thermal conductivity, the overall ZT was decreased across the entire temperature range of measurement. Both Sn and Bi were shown to worsen the thermoelec-

tric properties of Ge_4SbTe_5. These decreases in thermoelectric performance were attributed primarily to changes in the band gap, which arose from the substitution of group IV and V elements. Future work on lowering the thermal conductivity using other isovalent substitutions such as Si, Se, or S should be investigated. In the sections to follow a description of the work on impurity doping in Ge_4SbTe_5 will be presented.

5.3 Electronic Doping

Doping foreign atoms which either introduce a donor or acceptor into a crystal lattice is one of the most effective methods of tuning carrier concentration, and can therefore lead to increases in the ZT of thermoelectric materials. Welzmiller, *et al* studied Mn doping in $Ge_4Sb_2Te_7$, which resulted in a ZT enhancement as well as the introduction of a ferromagnetic phase from the Mn ions.[131] Welzmiller, *et al* also observed a nearly three-fold increase in ZT by doping Cr on the Ge site in $GeSb_2Te_4$.[132] In 2015 Welzmiller, *et al* studied the effects of Cd doping on $(GeTe)_nSb_2Te_3$ and $(SnTe)_nSb_2Te_3$ compounds and found that the Cd increased the density of states effective mass and led to an increase in the Seebeck coefficient, which allowed for slight increases in the power factor, and ZT overall.[122] In the following sections the work done on doping Ge_4SbTe_5 with Na and Ga will be presented.

5.3.1 $Ge_{4-x}Na_xSbTe_5$

Alkali metals are monovalent with one valence electron filling the s-shell. Ge is nominally divalent, and if substituted by an alkali metal such as Na or Li, could in principle be doped p-type. Similar chalcogenide materials, such as PbTe and $AgSbSe_2$ have exhibited increased ZT by Na doping.[133, 134] The Na doping in these compounds allowed for an optimization

of the carrier concentration, but also, because of the difference in mass and atom size between Na and the host atom, displayed a decrease in thermal conductivity. Schroder, *et al* studied the effects which Li doping has on the thermoelectric properties of GeTe-Sb_2Te_3 alloys, but the effects of Na doping on the Ge site in GeTe-Sb_2Te_3 compounds has yet to be studied for thermoelectric applications.[135]

5.3.1.1 Experimental

Samples of 0.5%, 1.0%, and 1.5% Na doped Ge_4SbTe_5, which corresponds to $Ge_{3.98}Na_{0.02}SbTe_5$, $Ge_{3.96}Na_{0.04}SbTe_5$, and $Ge_{3.94}Na_{0.06}SbTe_5$, respectively, were synthesized by placing stoichiometric amounts of Ge, Sb, Te, and Na_2Te (99.9%, 60 mesh) in evacuated silica ampoules. Because of the volatility of Na, the ampoules were first coated with a layer of carbon. The samples were melted for 12h and quenched in water. The purity of the synthesized compounds was verified using room temperature X-ray diffraction. All diffraction patterns were single phase and showed no changes in d-spacing or intensity, implying the successful incorporation of Na atoms on the Ge site.

5.3.1.2 Results and Discussion

Increasing the concentration of Na doped for Ge caused a decrease in electrical resistivity and Seebeck coefficient, which is consistent with an increase in the hole concentration. The electrical resistivity can be seen in Figure 5.19 and the Seebeck coefficient can be seen in Figure 5.20.

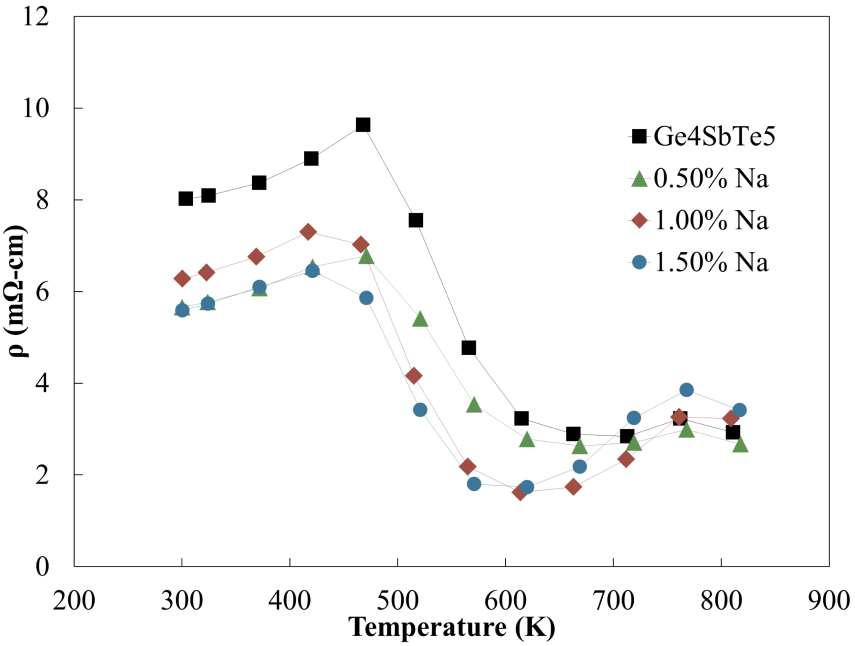

Figure 5.19: Electrical resistivity versus temperature for 0.5%, 1.0%, and 1.5% Na-doped Ge_4SbTe_5.

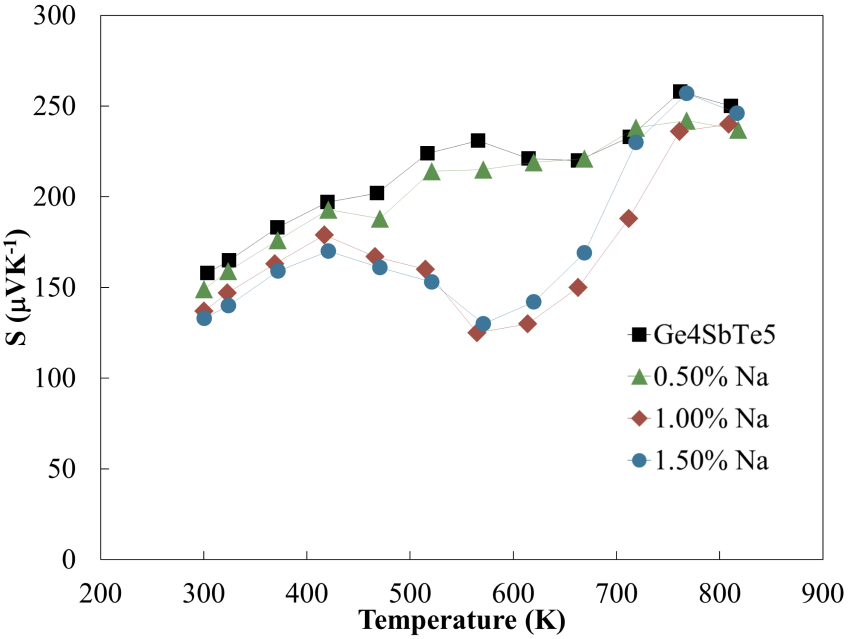

Figure 5.20: Seebeck coefficient versus temperature for 0.5%, 1.0%, and 1.5% Na-doped Ge_4SbTe_5.

High temperature Hall measurements were performed at the University of Michigan by

Alexander Page under the supervision of Dr. Ctirad Uher on Ge_4SbTe_5 and 1.50% Na doped Ge_4SbTe_5. No change in the hole concentration was observed below the phase transition, but at temperatures above the phase transition the hole concentration was increased approximately 80%. The hole concentration and hole mobility (calculated from the one carrier approximation for electrical conductivity $\sigma = pe\mu_h$) can be seen in Figure 5.21(a) and (b), respectively.

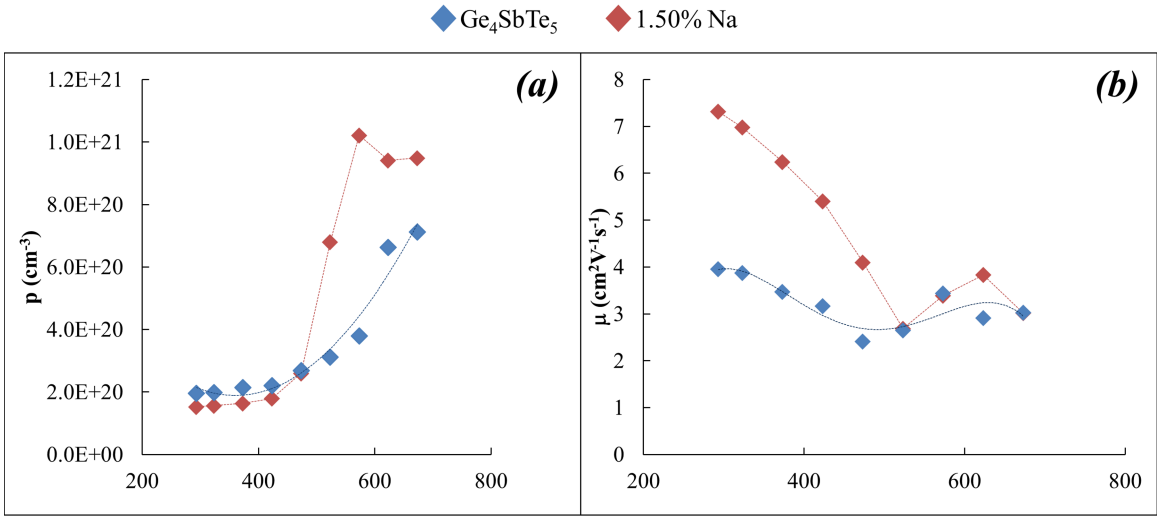

Figure 5.21: ***(a)*** Hole concentration versus temperature for Ge_4SbTe_5 and 1.5% Na doped. ***(b)*** Hole Mobility versus Temperature for Ge_4SbTe_5 and 1.5%.

The power factor experienced a slight increase with 0.5% Na, however the increase is well within the measurement uncertainty of ±12%. The higher doping amounts of 1.0% Na and 1.5% Na yielded decreases in the power factor to values significantly below $20\mu Wcm^{-1}K^{-2}$. The power factor versus temperature for Ge_4SbTe_5, 0.5% Na, 1.0% Na, and 1.5% Na doped Ge_4SbTe_5 can be seen in Figure 5.22.

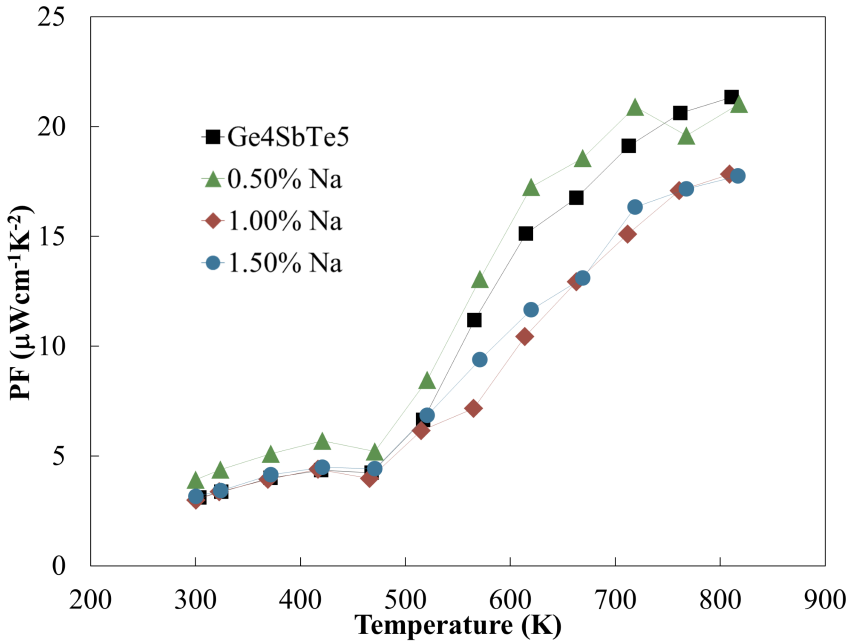

Figure 5.22: Power Factor versus Temperature for 0.5%, 1.0%, and 1.5% Na-doped Ge_4SbTe_5.

In compounds such as PbTe, as was aforementioned, Na doping is a means to tune the charge carrier concentration, but also has also been shown to decrease the thermal conductivity. As can be seen in Figure 5.23, the thermal conductivity near room temperature experienced no change. For 1.50% Na doped the thermal conductivity was decreased from values around $1.5 Wm^{-1}K^{-1}$ to $1.0 Wm^{-1}K^{-1}$ at temperatures above the phase transition temperature. This decrease could be due to the scattering of phonons from the mass difference between Ge and Na.

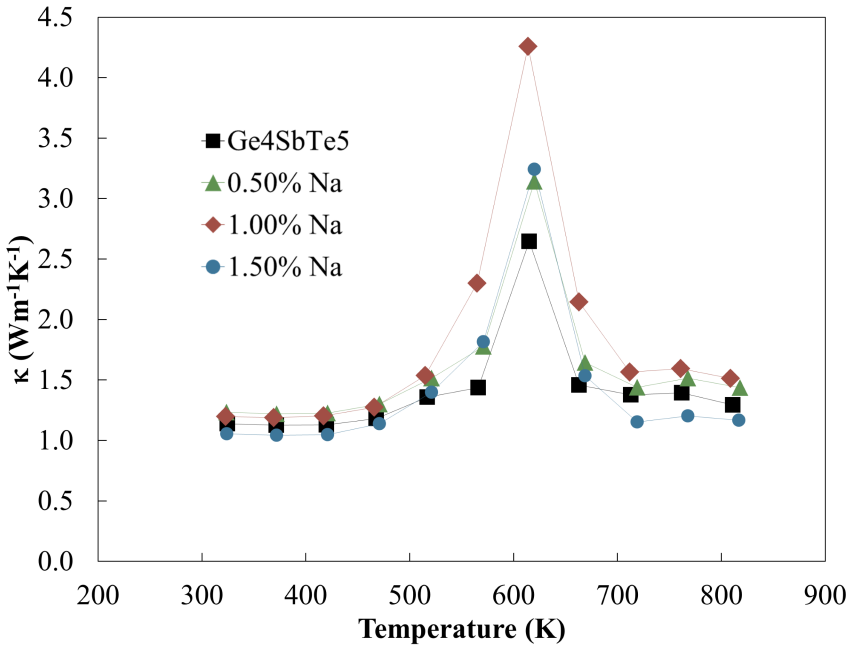

Figure 5.23: Thermal conductivity versus temperature for 0.5%, 1.0%, and 1.5% Na-doped Ge_4SbTe_5.

5.3.1.3 Conclusion

The small decrease in thermal conductivity and the decrease in power factor resulted in a non-neglible decrease in the ZT of Na-doped Ge_4SbTe_5. ZT versus temperature for Ge_4SbTe_5 and the Na-doped samples can be seen in Figure 5.24. This decrease in ZT stems from essentially over-doping. As was mentioned in the introduction, the thermoelectric power factor and ZT of a given material is optimized as a function of carrier concentration. Based on the results for Na doping it would seem that the maximum in power factor and ZT should be at, or below, the carrier concentration of undoped Ge_4SbTe_5.

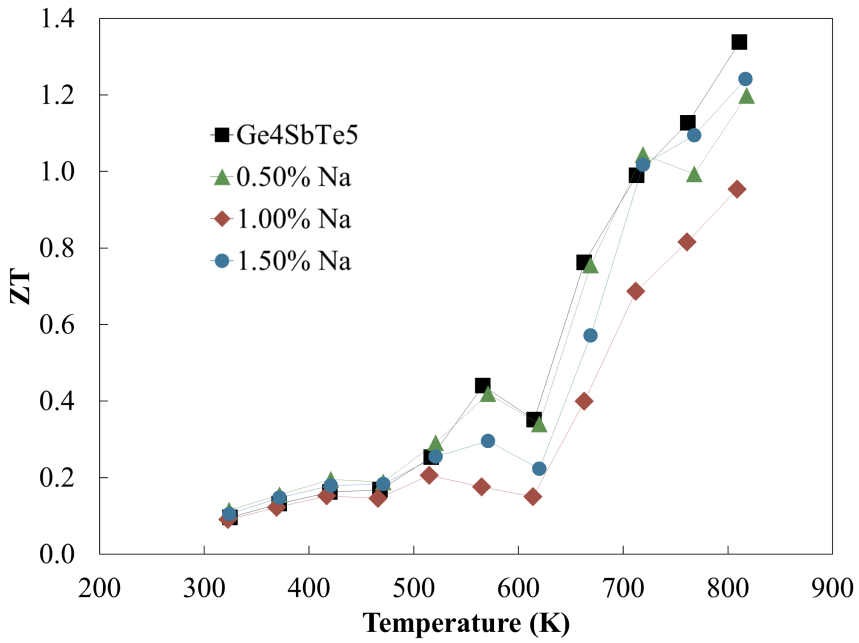

Figure 5.24: ZT versus Temperature for 0.5%, 1.0%, and 1.5% Na-doped Ge_4SbTe_5.

5.3.2 $Ge_{4-x}Ga_xSbTe_5$

The element Ga is found in the group III column of the periodic table and has the the electronic configuration of $[Ar]3d^{10}4s^24p^1$, which has one less valence electron in the p-shell than Ge. Ga as a dopant for Ge would therefore introduce one acceptor per dopant atom. In this study Ga was used as a dopant for Ge in an attempt to increase the hole concentration, which would lower the electrical resistivity and Seebeck coefficient and allow for an optimization of ZT.

5.3.2.1 Experimental

Stoichiometric amounts of Ge, Sb, Te, and Ga (Alfa Aesar, 6mm diameter pellets, 99.9999%) were placed in silica ampoules and evacuated. The tubes were then sealed and thermally treated as was mentioned for Ge_4SbTe_5 in previous sections. Phase purity was confirmed

using room temperature X-ray diffraction. All samples were ball milled for 5 minutes and densified using spark plasma sintering for 15min at 400°C under 40MPa of pressure. Volumetric density was measured using an ethanol based Archimedes method. The resulting pellet was then cut for thermoelectric characterization measurements at both cryogenic temperatures and high temperatures. The specific samples synthesized were $Ge_{3.96}Ga_{0.04}SbTe_5$, $Ge_{3.8}Ga_{0.2}SbTe_5$, and $Ge_{3.6}Ga_{0.4}SbTe_5$, which correspond to Ga concentrations of 1%, 5%, and 10%, respectively.

5.3.2.2 Results and Discussion

Because of the small atomic size difference between Ga and Ge there was a negligible shift in the d-spacing of the X-ray diffraction patterns between samples, as can be seen in Figure 5.25. For 5% and 10% Ga doped, the secondary phase Ga_2Te_3 was formed and observed in the X-ray diffraction pattern (PDF#00-035-1490). It is conjectured that the Ga_2Te_3 secondary phase was not observed in the X-ray pattern of the 1% Ga doped sample due to the low concentration of Ga_2Te_3 present.

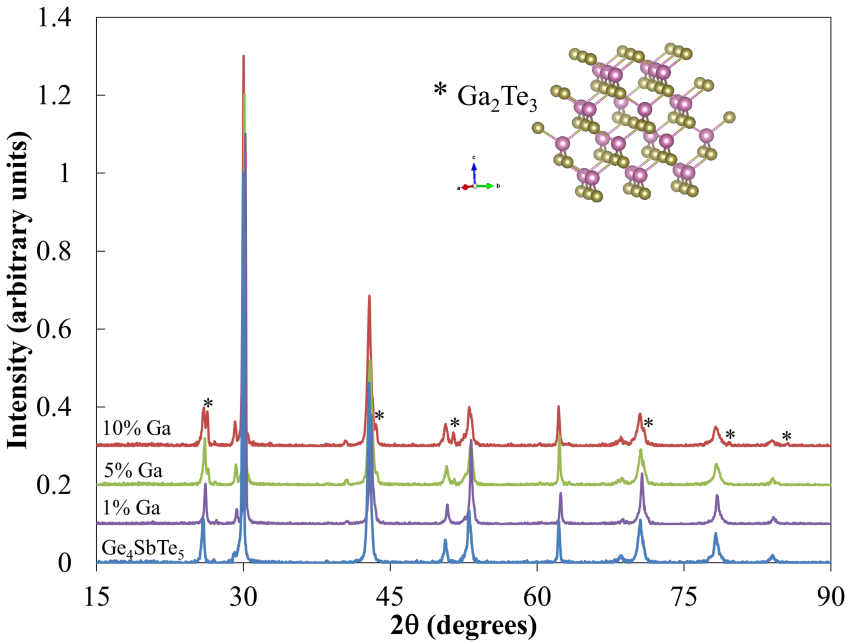

Figure 5.25: X-ray diffraction patterns for $Ge_{4-x}Ga_xSbTe_5$, 1%, 5%, and 10% Ga.

Ga_2Te_3 forms a defect zinc-blende crystal structure, space group $F\bar{4}3m$. An example of the crystal structure, which was generated using Vesta software from JP-Minerals, can be seen in Figure 5.25.[91] Ga_2Te_3 contains a high concentration of vacancies with $\frac{1}{3}$ of all anion sites being an empty atomic site. The compound therefore exhibits an interesting number of physical properties, such as a naturally occurring superstructure from the ordered vacancy planes which lend to unusually low thermal conductivity.[136] Ga_2Te_3 has a bandgap of approximately 1.1eV at room temperature, and, with the high vacancy concentration, lends to a large electrical resistivity and p-type Seebeck coefficient.[137] Additionally, the compound has been investigated for use in phase change memory applications.[138]

Most often, secondary phases are considered undesirable for studies in thermoelectrics research, in part because of the work by Bergman and Levy, which found that under idealistic assumptions the ZT of a composite could never exceed that of the highest ZT of the comprising materials.[139] The compounds of Ga doped Ge_4SbTe_5 were nonetheless fully

characterized. The electrical resistivity, Figure 5.26, began to exhibit insulating behavior at temperatures below the phase transition temperature, with increases from approximately 8mΩ cm to greater than 50mΩ cm for 10% Ga doped Ge_4SbTe_5. This is in-line with the observance of an increasing amount of Ga_2Te_3 secondary phase. The Seebeck coefficient showed a marginal increase, despite the increased electrical resistivity, as can be seen in Figure 5.27. The small increase in Seebeck coefficient could be explained by the thermal excitation of carriers from Ga_2Te_3, which would produce competing carriers and thereby offset any contribution to Seebeck coefficient.

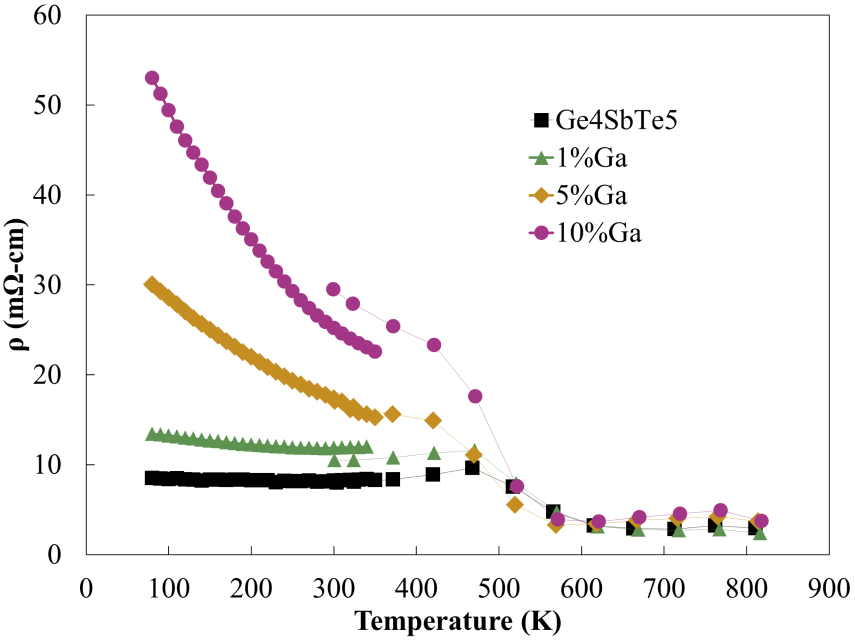

Figure 5.26: Electrical resistivity versus temperature for 1%, 5%, and 10% Ga doped Ge_4SbTe_5.

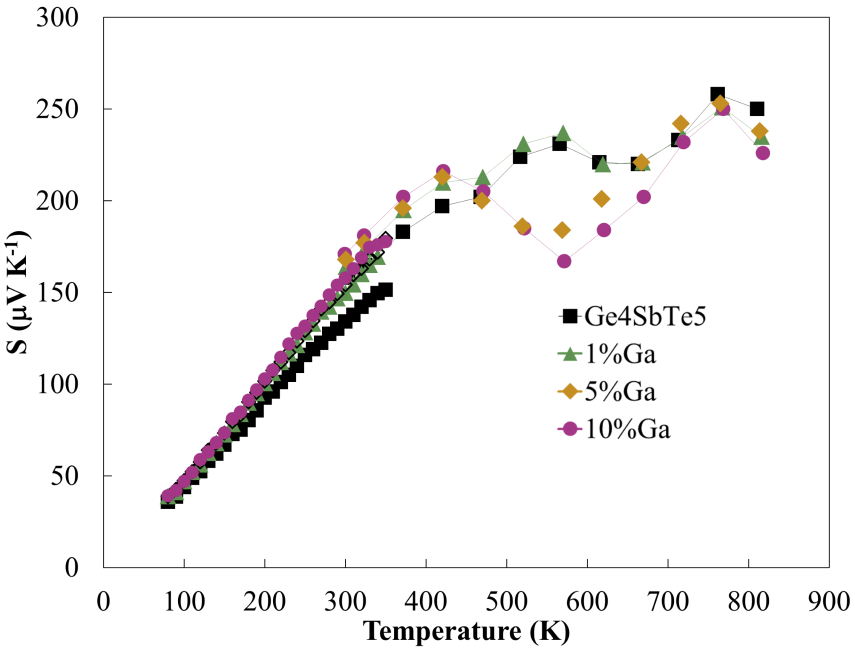

Figure 5.27: Seebeck coefficient versus temperature for 1%, 5%, and 10% Ga doped Ge_4SbTe_5.

Despite the high electrical resistivity, the small enhancements in Seebeck coefficient resulted in an increased power factor, to values as high as 23.1μWcm^{-1}K^{-2}. The presence of these secondary phases also decreased the thermal conductivity across the entire temperature range. The power factor and thermal conductivity versus temperature can be seen in Figure 5.28(a) and (b), respectively.

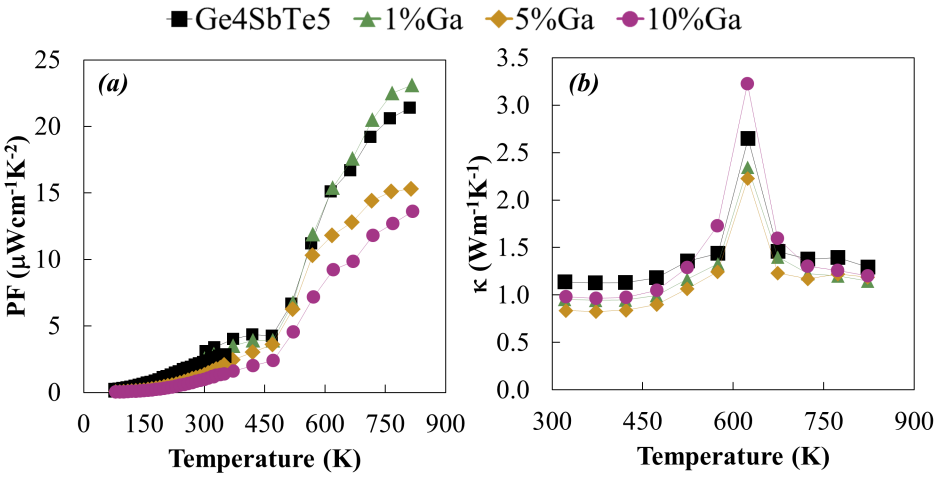

Figure 5.28: (a) Power factor versus temperature for 1%, 5%, and 10% Ga doped Ge_4SbTe_5. (b) Thermal conductivity versus temperature for Ga-doped Ge_4SbTe_5.

The ZT versus temperature for $Ge_{4-x}Ga_xSbTe_5$ can be seen Figure 5.29. For the higher Ga concentrations, namely 5% and 10%, the ZT was decreased, but, surprisingly, for 1% Ga-doped Ge_4SbTe_5 there was a significant increase in ZT, with a peak at 823K greater than 1.6. Though the ZT appears to continue rising, the temperature was kept in a range of stability for Ge_4SbTe_5 (< 900K).

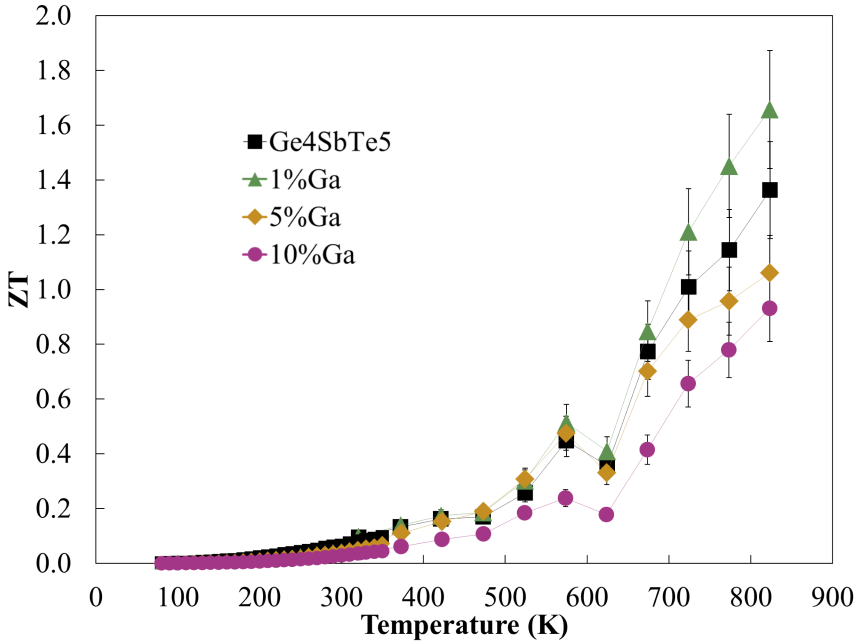

Figure 5.29: ZT versus temperature for 1%, 5%, and 10% Ga doped Ge_4SbTe_5.

5.3.2.3 Conclusion

The increase in ZT despite the existence of secondary phases contradicts the theoretical work of Bergman and Levy, but is not uncommon in thermoelectrics research. Using secondary phases to tune the power factor while simultaneously maintaining a low thermal conductivity has been used in materials such as $CoSb_3$ and PbTe to achieve some of the highest ZT values to date.[140, 67] Using secondary phases to enhance the thermoelectric performance becomes an important concept in the remainder of this work.

5.4 Summary and Future Work

Ge_4SbTe_5 is a phase change memory material which does not lie on the GeTe-Sb_2Te_3 pseudo-binary tie-line. The compound exists in a metastable rocksalt crystal structure upon rapid quenching from the melt. In this rocksalt crystal structure the Ge and Sb atoms are ran-

domly distributed on the cation site with the Te atoms occupying the anion sublattice. Upon heating this metastable rocksalt phase undergoes an ordering transition to the stable rhombohedral phase. This phase transition is accompanied by a drop in electrical resistivity. Despite the decrease in electrical resistivity the Seebeck coefficient continues to increase while the thermal conductivity stays relatively temperature independent. The ZT reaches values well above unity, which are comparable to state-of-art PbTe.

It was shown that both $Ge_{4-x}Sn_xSbTe_5$ and $Ge_4Sb_{1-x}Bi_xTe_5$, which were isovalent atomic substitutions intended to lower the lattice contribution to thermal conductivity, actually decreased the thermoelectric performance. From the decreased trend of the Seebeck coefficient, it is believed that the substitutions caused a change in the band gap of Ge_4SbTe_5. Future work could include the study of other substitutions such as Si on the Ge atomic site or Se on the Te atomic site.

Na, which is predominately monovalent, was substituted for Ge. This was done to increase the hole concentration, as Na would introduce an acceptor for each atom substituted. Samples with 0.5, 1.0, and 1.5% Na in Ge_4SbTe_5 were synthesized and shown to decrease the electrical resistivity and Seebeck coefficient. Unfortunately the power factor and ZT were decreased, implying the carrier concentration was too high for the optimization of ZT. Ga was doped for Ge, which also should have acted as a p-type dopant. The Ga was not successfully substituted for Ge, but rather formed the impurity phase Ga_2Te_3. Despite the existence of this secondary phase the power factor was increased, thermal conductivity was decreased, and the ZT was increased at temperatures above 600K for 1% Ga doped Ge_4SbTe_5. A more controlled study of the thermoelectric properties of Ge_4SbTe_5-Ga_2Te_3 composites should be conducted so as to properly understand the mechanism of power factor and ZT enhancements. Future dopants could include In, Zn, transition metals, or rare-earth

elements, which could introduce a magetic moment and enhance the Seebeck coefficient.

Chapter 6

$Ge_{17}Sb_2Te_{20}$

$Ge_{17}Sb_2Te_{20}$ rests on the GeTe-rich side of the GeTe-Sb_2Te_3 binary tie-line. The formula can be alternatively written as $(GeTe)_{17}Sb_2Te_3$, where Sb_2Te_3 represents a roughly 5.9% substitution in GeTe. Few studies, other than for bulk thermoelectrics have been conducted on this specific composition. It displays degenerate p-type semiconducting nature and has a melting point of approximately 670°C.[141]

The stable crystal structure for $Ge_{17}Sb_2Te_{20}$ is the rhombohedral phase, $R\bar{3}m$. This phase as aforementioned, has alternating layers of Ge, Sb, and Te atoms, with inter-penetrating vacancy layers between van der Waals bonded Te layers. A metastable rocksalt phase exists when synthesized under non-equilibrium conditions, such as chemical vapor deposition or rapid quenching. This rocksalt phase, upon heating, transitions to the stable rhombohedral crystal structure at approximately 500K. A second phase transition occurs at temperatures just below 600K from the rhombohedral phase to a rocksalt phase. The high temperature rocksalt phase, similar to GeTe, exists only at elevated temperature and corresponds to the temperature at which the ferroelectric state transitions to a paraelectric state. These phase transitions can be observed in the specific heat versus temperature for $Ge_{17}Sb_2Te_{20}$, which can be seen in Figure 6.1.

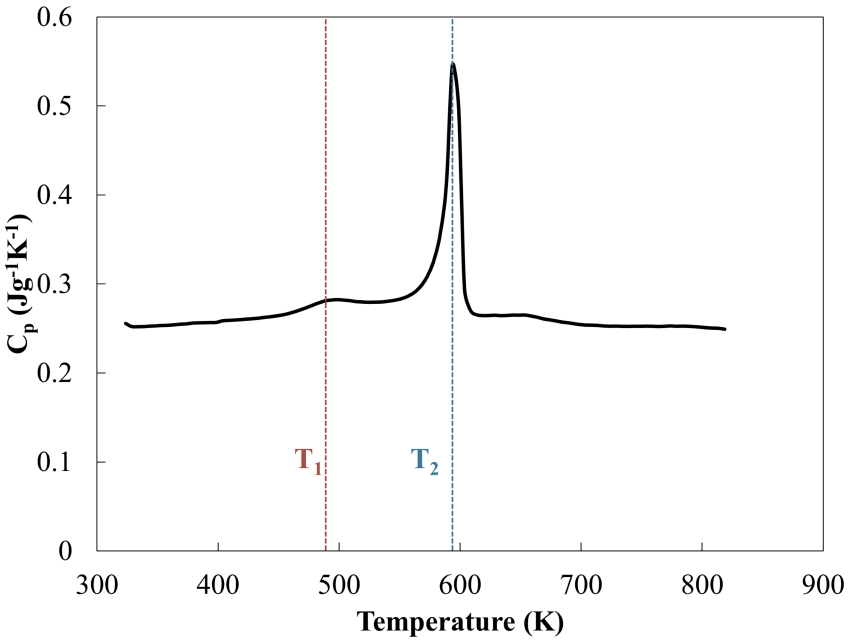

Figure 6.1: Specific heat versus temperature, measured by DSC, for $Ge_{17}Sb_2Te_{20}$. The phase transitions can be seen as endothermic peaks at T_1, the transition from metastable rocksalt to rhombohedral, and T_2, the phase transition from the stable rhombohedral phase to the stable rocksalt phase.

The temperature dependent X-ray diffraction patterns can be seen in Figure 6.2 and Figure 6.3 for the warming and cooling trends, respectively. Upon warming the first phase transition from metastable rocksalt to rhombohedral is not clearly discernible. It is believed that because the transition is an order-disorder transition and is therefore diffusion-limited there has not been substantial time for the full transition to take place. Upon further warming the high temperature rocksalt phase can be seen above 623K. Upon cooling, the stable rhombohedral phase can be discerned, and begins to form around 571K.

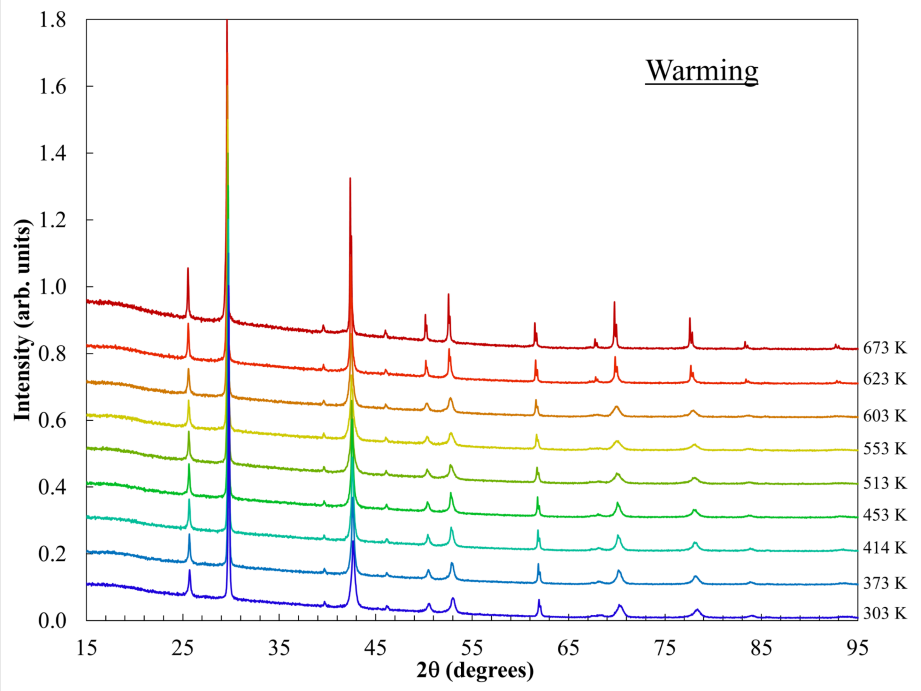

Figure 6.2: X-ray diffraction patterns for $Ge_{17}Sb_2Te_{20}$ upon heating from room temperature. The first transition from metastable rocksalt to rhombohedral is not discernible, but the high temperature rocksalt phase can be seen at approximately 623K.

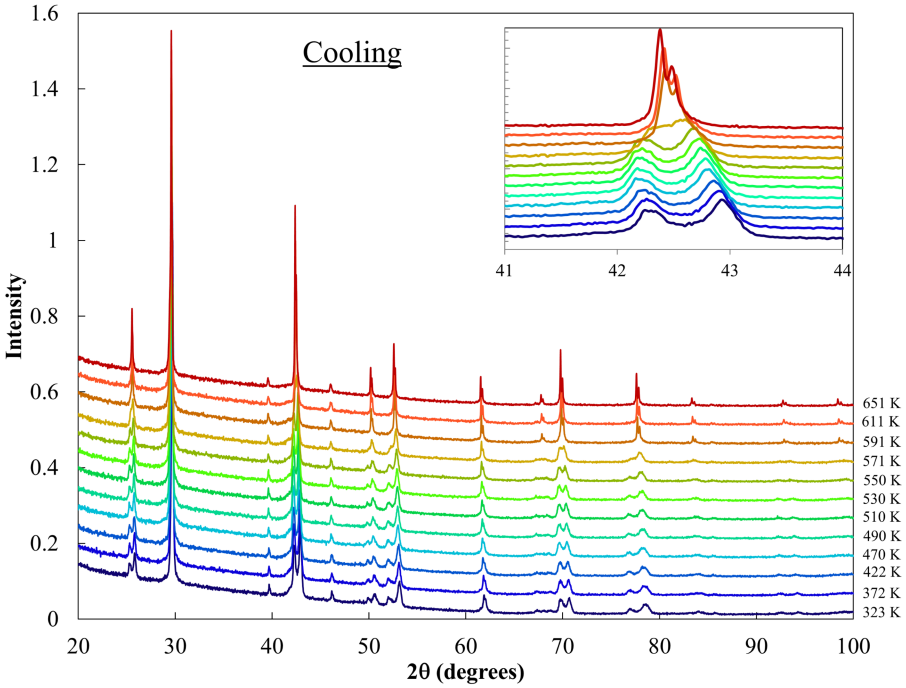

Figure 6.3: X-ray diffraction patterns for $Ge_{17}Sb_2Te_{20}$ upon cooling. The stable rhombohedral phase is discernible below 570K.

In the following work stoichiometric amounts of Ge, Sb, and Te were placed in evacuated silica ampoules and melted at 1173K for 12 hours. The samples were then water quenched to room temperature. Additional annealing was performed at 863K, above the second phase transition temperature, for 24h and again water quenched. X-ray diffraction was performed on all ingots obtained. The samples were ball-milled for 5min in a stainless steel jar with stainless steel balls. The ball-milled powder was then sintered using SPS at 673K, for 5min, under 40MPa of uniaxial pressure. The sintered pellets were accordingly cut using a diamond saw for thermoelectric characterization, thermal characterization, and X-ray diffraction.

The X-ray diffraction patterns of $Ge_{17}Sb_2Te_{20}$ quenched from the melt and annealed are displayed in Figure 6.4. When quenched from the melt $Ge_{17}Sb_2Te_{20}$ forms in the rhombohedral crystal structure ($R\bar{3}m$). When further annealed at 590°C, $Ge_{17}Sb_2Te_{20}$ forms in the rocksalt crystal structure($Fm\bar{3}m$). For the annealed sample the peaks in the pattern are quite broad which could be due to large amounts of strain in the system from the quenching process. By assigning the allowed Miller indices for the diffraction peaks of the rocksalt phase, the lattice parameter was calculated to be 5.92Å, which yields a theoretical density of $6.256 g\text{cm}^{-3}$. The X-ray diffraction pattern of melt-quenched $Ge_{17}Sb_2Te_2$ reveals impurities of elemental Ge and Sb, as can be seen in Figure 6.4. The rhombohedral phase has a calculated lattice parameter of 4.24Å with a rhombohedral angle of 58.24°.

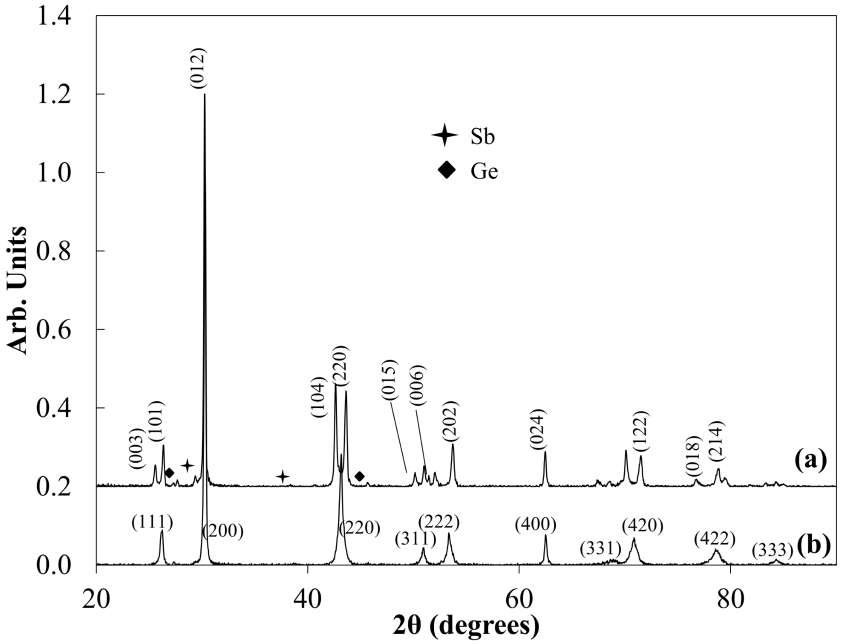

Figure 6.4: (a) X-ray diffraction pattern of $Ge_{17}Sb_2Te_{20}$ quenched from 1173K, seen here with Sb and Ge impurities labeled. Quenching from the melt yields a rhombohedral crystal structure. (b) X-ray diffraction pattern of $Ge_{17}Sb_2Te_{20}$ quenched from the melt and annealed for an additional 24h at 863K. This method produces an impurity free rocksalt phase.

Despite having secondary phases in the quenched sample, both the quenched and annealed $Ge_{17}Sb_2Te_{20}$ samples were characterized. The thermoelectric properties of both compounds were found to be nearly the same, aside from a slightly higher ZT for the quenched compound, as can be seen in Figure 6.5.

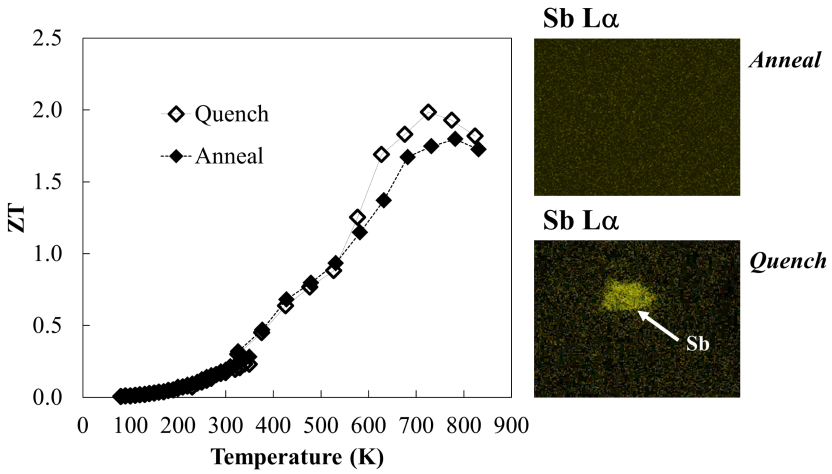

Figure 6.5: ZT versus temperature for $Ge_{17}Sb_2Te_{20}$ prepared by quenching from the melt and subsequently annealing. The SEM/EDS elemental maps show the presence of Sb precipitates.

The performance of the quenched compound with the secondary phases contradicts the theoretical work of Bergman and Levy from 1991.[139] Their work aimed to determine the validity of making composites which could overrcome the contraindicated properties of ZT. Unfortunately it was found that under ideal conditions, the ZT of a composite could not exceed the highest ZT of any one of the constituents which comprise the composite. As a preliminary means of gauging the role and validity of enhancing the ZT of $Ge_{17}Sb_2Te_{20}$ with secondary phases, the stoichiometric amount of Sb was varied. Specifically, the following compounds were quenched from 1173K and synthesized using the aforementioned synthesis parameters: $Ge_{17}Sb_{1.90}Te_{20}$, $Ge_{17}Sb_{1.95}Te_{20}$, $Ge_{17}Sb_2Te_{20}$, $Ge_{17}Sb_{2.10}Te_{20}$, and $Ge_{17}Sb_{2.20}Te_{20}$.

The electrical resistivity and Seebeck coefficient increased with increasing Sb content, as can be seen in Figure 6.6(a) and (b), respectively. This behavior would indicate a dependence of the charge carrier concentration on the amount of Sb impurity phase. It was therefore believed that the Sb, which is defined as a semimetal was decreasing the hole con-

centration. The ZT showed a dependence on the Sb content, with a peak value above 2.0 for $Ge_{17}Sb_{2.1}Te_{20}$, as can be seen in Figure 6.6(c) and (d).

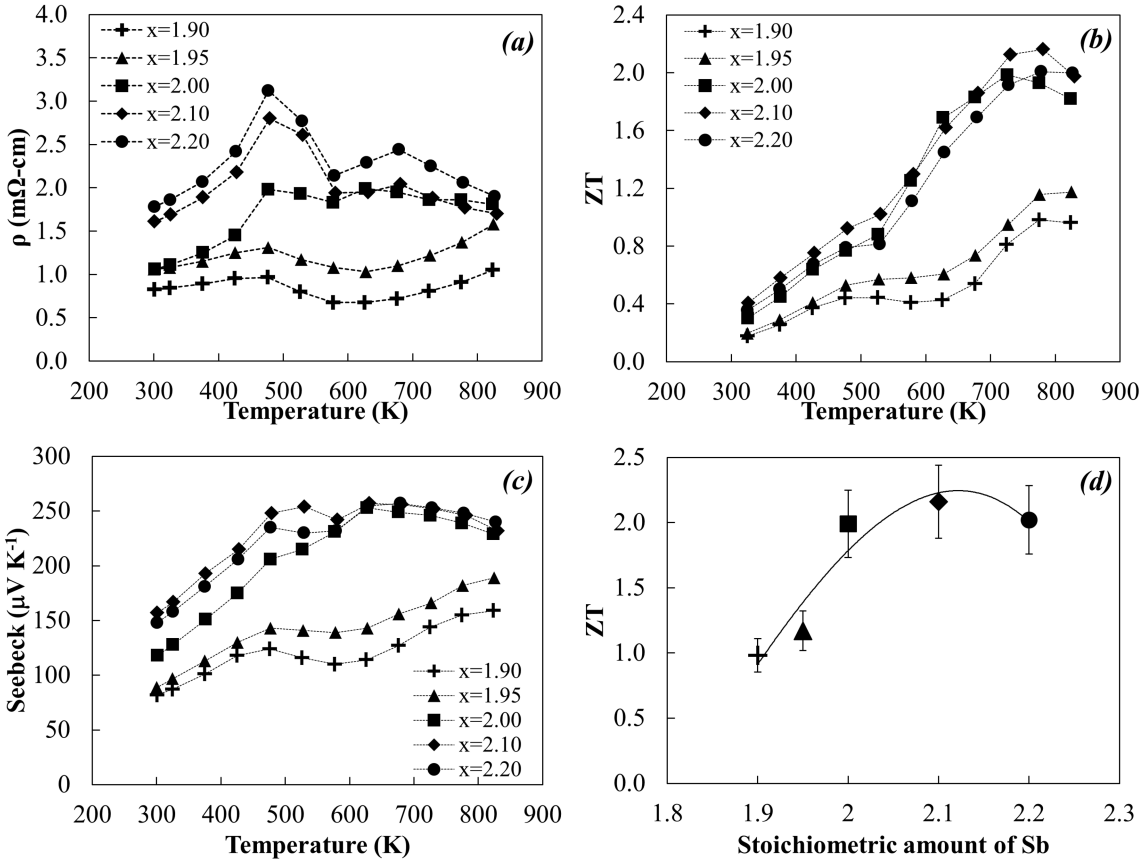

Figure 6.6: (a)The electrical resistivity, (b) ZT, and (c) Seebeck coefficient for $Ge_{17}Sb_xTe_{20}$. By altering the stoichiometry of Sb, and therefore the concentration of Sb secondary phase, the properties can be tuned. (d) Shows ZT at 773K versus x, the stoichiometric amount of Sb.

These results are exciting, but lack the proper scientific quality to be deemed valid. Both Sb and Ge impurities exist in the compound, but also, the existence of these secondary phases upon quenching implies that $Ge_{17}Sb_2Te_{20}$ is not stoichiometric since additional time is necessary to allow all of the Sb and Ge to diffuse onto their respective lattice sites. Based on the findings above the following hypothesis was formed:

Seconday phases of elemental Sb and/or Ge provide a route for tuning the electrical and

thermal properties of $Ge_{17}Sb_2Te_{20}$, which in turn could be used to optimize the thermoelectric performance.

To experimentally investigate this hypothesis two separate studies on the effects of elemental Sb and Ge as a secondary phase in $Ge_{17}Sb_2Te_{20}$ were conducted. The following sections will describe in greater detail the results of these projects.

6.1 Probing the Role of Sb Impurities

The goal of this specific project was to understand the mechanisms, if any, Sb impurities play in affecting the thermoelectric performance of $Ge_{17}Sb_2Te_{20}$. To probe this experimentally, pristine $Ge_{17}Sb_2Te_{20}$ was synthesized and characterized. Additional samples were then made with controlled amounts of elemental Sb as an impurity. Below are the experimental procedures, results and discussion, and conclusions from this work.

6.1.1 Synthesis Procedures

To synthesize single phase $Ge_{17}Sb_2Te_{20}$ stoichiometric amounts of Ge (Alfa Aesar, zone-refined ingot, 99.9999%), Sb (Alfa Aesar, 6mm shot, 99.999%), and Te (Alfa Aesar, chunck, 99.999%) were sealed in silica ampoules which were evacuated to approximately $10^{-5}Torr$. The samples were then melted at 1173K for 12h and water quenched. Additional annealing was done at 863K for 24h and again water quenched. Additional Sb (Alfa Aesar, 6mm shot, 99.999%) was added to the materials before powder processing. The resulting ingots and added Sb were then ball-milled in a SPEX vibratory mill for 5min using a stainless steel jar and stainless steel media. The powder was densified using SPS at 673K for 10min under

40MPa of uniaxial pressure. The phase purity and crystal structure was verified using room temperature X-ray diffraction and SEM/EDS in the Center for Advanced Microscopy.

6.1.2 Results and discussion

For $Ge_{17}Sb_2Te_{20}$+Sb_x, x was set equal to 0.0975, 0.195, 0.39, 0.78 which correspond to 0.25, 0.50, 1.0, and 2.0 mol% added Sb, respectively. The X-ray diffraction patterns revealed no change in the crystal structure of $Ge_{17}Sb_2Te_{20}$, as seen from Figure 6.7. As the amount of additional Sb reached 0.50% and higher the diffraction peaks associated with elemental Sb could be distinguished.

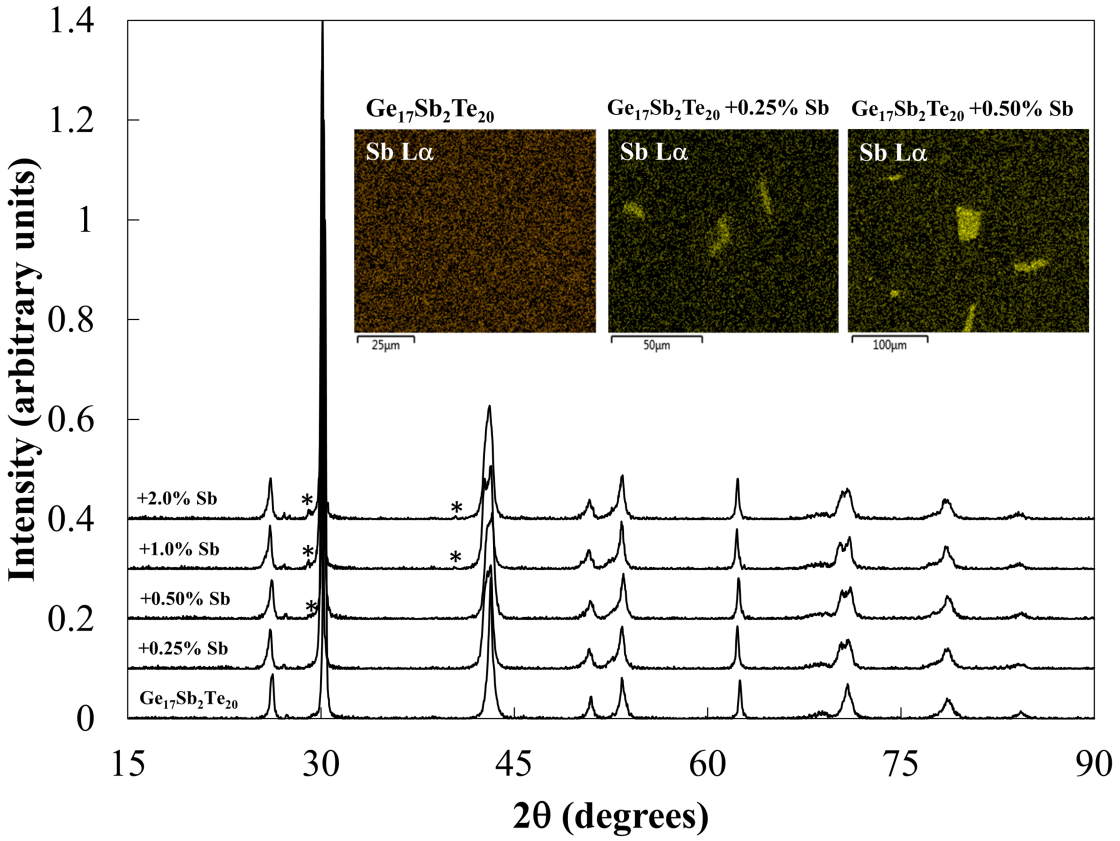

Figure 6.7: X-ray diffraction patterns for $Ge_{17}Sb_2Te_{20}$, with 0.25, 0.50, 1.0, and 2.0% added Sb. The star marks the diffraction peaks which indicate the presence of elemental Sb as a secondary phase(PDF#98-000-0095). The EDS maps clearly show the presence of Sb microstructures in $Ge_{17}Sb_2Te_{20}$.

To further verify the existence of Sb as a secondary phase and probe the general size of the Sb agglomerates SEM/EDS was performed, which can also be seen in Figure 6.7. Sb can be clearly distinguished as a secondary phase in $Ge_{17}Sb_2Te_{20}$. The general size of the Sb clumps range from approximately 1µm to 50µm. The size of the impurities puts the possibility of nanostructured quantum effects out of the question. It should also be noted that the impurities show no regular geometry or pattern, they are essentially randomly oriented and irregularly shaped.

The electrical resistivity for the samples can be seen in Figure 6.8(a). As the Sb content is increased the electrical resistivity across all temperatures was increased. The Seebeck coefficient is also increased with increased Sb content (Figure 6.8(b)).

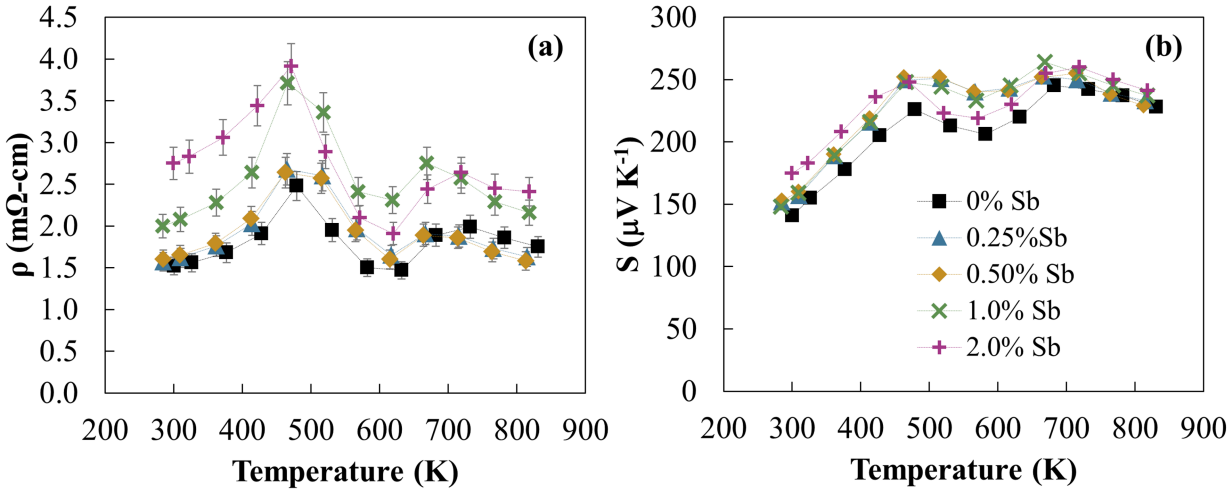

Figure 6.8: (a)Electrical resistivity versus temperature, seen here with ±8% error bars and (b)Seebeck coefficient versus temperature for $Ge_{17}Sb_2Te_{20}$ with 0.25, 0.50, 1.0, and 2.0% added Sb, in this figure the uncertainty of ±2% associated with measuring the Seebeck coefficient is smaller than the markers.

Because of the increased Seebeck coefficient and electrical resistivity it was initially believed that the Sb impurities were decreasing the hole concentration. To verify this hypothesis Hall measurements were performed at room temperature. The measurements showed no significant change in the hole concentration with increased Sb content. Rather, there was a

sharp decrease in the hole mobility with the addition of Sb secondary phase. The electrical resistivity, Seebeck coefficient, hole concentration, and hole mobility at 300K as a function of Sb content can be seen in Table 6.1.

Table 6.1: Electrical resistivity, Seebeck coefficient, carrier concentration, and hole mobility at 300K for $Ge_{17}Sb_2Te_{20}+Sb_x$.

Electrical resistivity, Seebeck coefficient, carrier concentration, and hole mobility at 300K				
$Ge_{17}Sb_2Te_{20}+Sb_x$	ρ (mΩ-cm)	S (μVK^{-1})	p ($x10^{20}$ cm^{-3})	μ_h ($cm^2V^{-1}s^{-1}$)
x=0	1.68	120	0.575	87.8
x=0.0975	2.19	150	1.05	30.2
x=0.195	3.06	186	1.33	20.5
x=0.39	4.87	183	1.60	10.5
x=0.78	6.55	188	1.35	7.09

Because of the increased Seebeck coefficient, the power factor was increased to values well above $30\mu Wcm^{-1}K^{-2}$ for 0.25% and 0.50% added Sb. For higher concentrations of added Sb the hole mobility was decreased too far and resulted in a decrease in power factor as can be seen in Figure 6.9(a). The complement between decreased hole mobility and increased Seebeck coefficient can be seen in Figure 6.9(b).

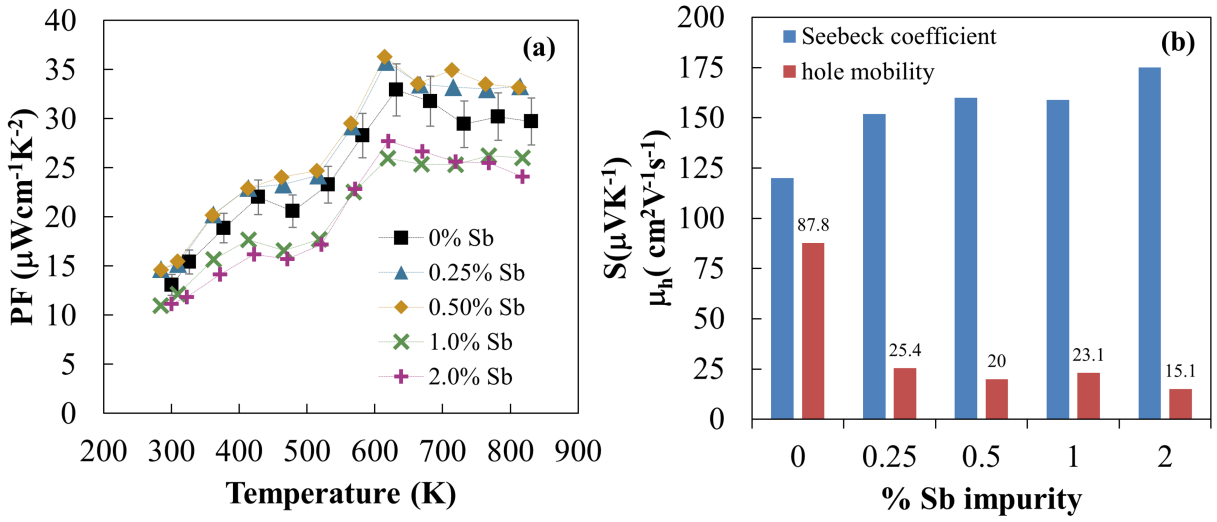

Figure 6.9: (a) Power Factor versus temperature for $Ge_{17}Sb_2Te_{20}$+Sb_x, seen here with ±8% error bars. (b) Seebeck coefficient and hole mobility at 300K as a function of %Sb as an impurity. A clear compliment can be seen between the two properties, which is indicative of a change in the scattering relaxation time.

Similar results in Pb-precipitated PbTe were observed by Heremans, *et al.*[142] They found that the secondary phases of Pb acted as additional scattering sites in the PbTe matrix. The Pb precipitates did not change the charge carrier concentration but lowered the charge carrier mobility, which in turn resulted in an increased Seebeck coefficient by changing the energy dependence of the scattering relaxation time.

Recall from chapter 1 that for metals and degenerately doped semiconductors the Mott relation expresses the Seebeck coefficient as a function of the energy dependent electrical conductivity, equation (1.60). The electrical conductivity is typically equated to the product of e, the electron charge, $n(E)$ the energy dependent charge carrier concentration, and $\mu(E)$, the energy dependent charge carrier mobility. The mobility can be further expressed as the ratio of $\tau(E)$, the energy dependent relaxation time, and $m*$, the effective mass of the charge carriers, equation (1.24). The scattering relaxation time can be approximated with a power-law dependence for semiconductors with parabolic bands, equation (1.28):

Because the host matrix of $Ge_{17}Sb_2Te_{20}$ was not changed chemically, it is believed that the effective mass is not altered, but rather the energy dependence of $\tau(E)$ was increased, which resulted in a decrease in mobility and an increase in the Seebeck coefficient. To further verify and quantify the changing energy landscape of $\tau(E)$ the Nernst effect should be measured.[143]

The thermal conductivity was also decreased with the increasing presence of Sb impurities, which can be seen in Figure 6.10(a). To estimate the electronic contribution to thermal conductivity the Lorenz number was calculated using a single parabolic band approximation to fit the Seebeck coefficient below the phase transition temperature, determining the reduced Fermi energy, and calculating the Lorenz number accordingly. The Lorenz number versus temperature can be seen in Figure 6.10(c), with the free electron value of $2.44x10^{-8}W\Omega^{-1}K^{-2}$ marked by the dotted line. By subtracting the calculated electronic contribution from the total thermal conductivity the lattice contribution was determined. As can be seen in Figure 6.10(b) the lattice contribution to thermal conductivity was significantly decreased with an increasing presence of Sb secondary phase. This decrease in thermal conductivity is further justification that the Sb impurities act as scattering sites for both electrons and phonons in $Ge_{17}Sb_2Te_{20}$.

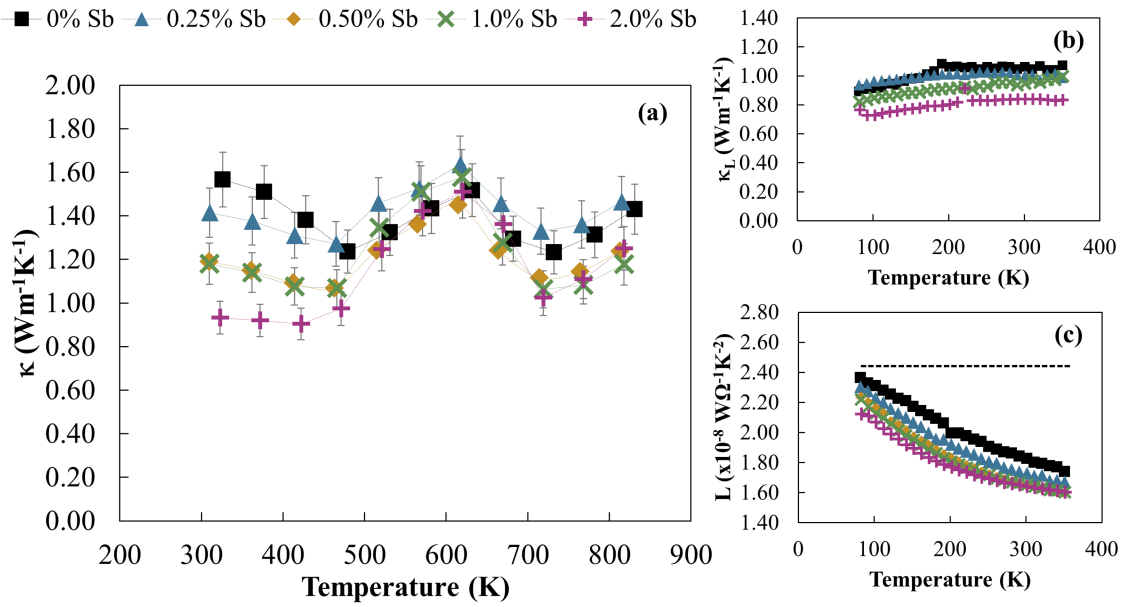

Figure 6.10: (a)Thermal conductivity versus temperature for $Ge_{17}Sb_2Te_{20}$ with 0.25, 0.50, 1.0, and 2.0% added Sb. (b)The lattice contribution to thermal conductivity versus temperature. (c)Lorenz number versus temperature, which was determined from a single parabolic band fit of the Seebeck coefficient.

With a decreased thermal conductivity and optimized power factor the calculated ZT was increased to values well above 2; seen in Figure 6.11. The largest increase in ZT was seen for 0.5% added Sb, which represents an average increase of approximately 20% at peak values. The ZT_{avg} was also increased to approximately 1.4.[144]

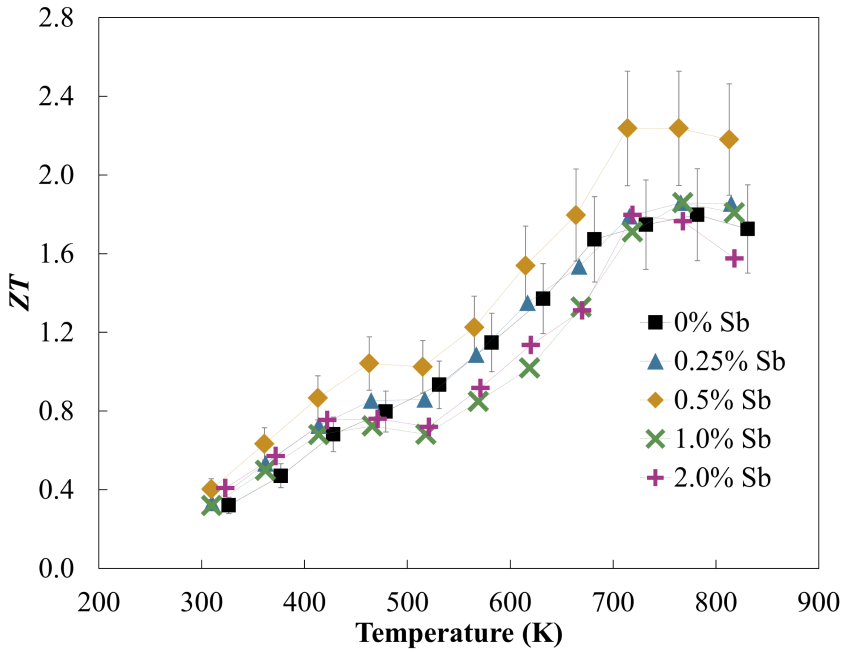

Figure 6.11: ZT versus temperature for $Ge_{17}Sb_2Te_{20}$ with 0.25, 0.50, 1.0, and 2.0% added Sb, seen here with ±13% on $Ge_{17}Sb_2Te_{20}$ and $Ge_{17}Sb_2Te_{20}$ + $Sb_{0.195}$. A large enhancement was observed for $Ge_{17}Sb_2Te_{20}$ with 0.5%Sb secondary phase.

6.1.3 Conclusion

This study aimed to understand the reason for why impurities of Sb in $Ge_{17}Sb_2Te_{20}$ lead to increased thermoelectric performance. It was found that power factor was enhanced because of an increase in electrical resistivity and Seebeck coefficient. Hall measurements revealed that the secondary phase of Sb did not change the hole concentration, but rather decreased hole mobility because of the increased scattering on the charge carriers in $Ge_{17}Sb_2Te_{20}$. The thermal conductivity was also decreased because of the ability of the Sb impurities to scatter heat carrying phonons. The result of these changes in the electrical and thermal properties was a significant enhancement in the ZT of $Ge_{17}Sb_2Te_{20}$ to values well above 2.0. In the future, studies on the geometry and particle size of the Sb precipitates should be conducted. Also, the effects of the precipitates on the mechanical properties would be of interest.

6.2 Probing the Role of Ge Impurities

Composites of $Ge_{17}Sb_2Te_{20}$ and Sb were shown to enhance the thermoelectric performance of pristine $Ge_{17}Sb_2Te_{20}$. The initial motivation for the project was to investigate the fundamental mechanisms behind the ZT enhancements caused by the secondary phases present in quenched $Ge_{17}Sb_2Te_{20}$, where both Ge and Sb impurities were present. The following study is an attempt to understand, if at all different from the case of Sb, what role the Ge secondary phases play in affecting the thermoelectric properties of $Ge_{17}Sb_2Te_{20}$.

6.2.1 Synthesis Procedures

Single phase rocksalt $Ge_{17}Sb_2Te_{20}$ was synthesized using the parameters aforementioned. 0.25%, 0.50%, 1.0%, and 2.0% added Ge was ball milled with single phase $Ge_{17}Sb_2Te_{20}$ for 5min in a stainless steel jar and under argon atmosphere. The resulting powder was densified using the same SPS parameters aforementioned for $Ge_{17}Sb_2Te_{20}$+Sb_x. Density of the sintered pellets was measured using the Archimedes method. All densities were $\geq 95\%$ theoretical density.

6.2.2 Results and Discussion

The X-ray diffraction patterns for $Ge_{17}Sb_2Te_{20}$+Ge_x revealed secondary phases of elemental Ge with concentrations greater than 1.0% Ge (PDF#01-073-7012). Overall the rocksalt crystal structure was maintained aside from some peak splitting around $70°2\theta$. This double peak could be a slight distortion along the [111] direction of the rocksalt crystal structure of $Ge_{17}Sb_2Te_{20}$. The presence of Ge secondary phases for 0.25% and 0.50%Ge added samples could not be verified using X-ray diffraction due to the low concentrations of the Ge. To

verify the existence of the Ge impurities SEM/EDS was conducted. The results of the EDS maps can be seen in Figure 6.12.

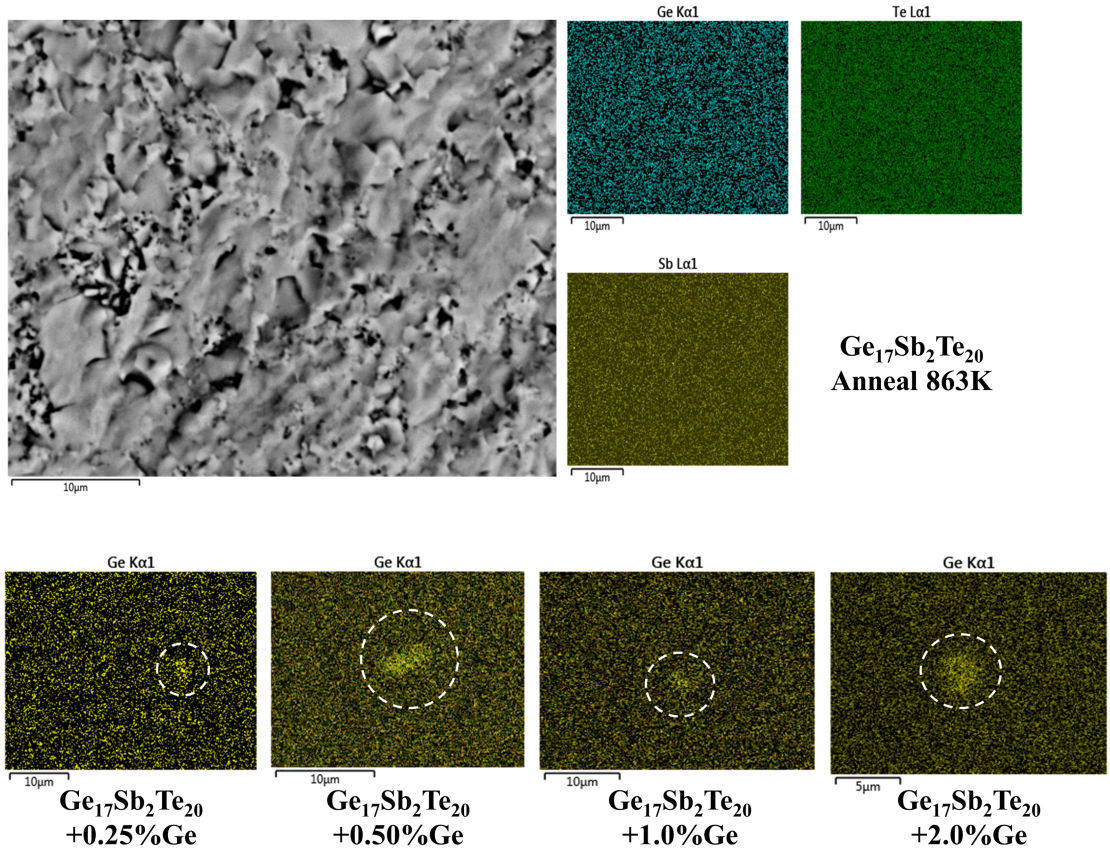

Figure 6.12: EDS elemental maps showcasing the presence of Ge impurities in $Ge_{17}Sb_2Te_{20}$+Ge_x samples.

Finding and identifying the Ge impurities proved to be difficult for two reasons: (1) The high atomic concentration of Ge in $Ge_{17}Sb_2Te_{20}$ produces a dense Ge background during the EDS elemental analysis, and (2) the size of the Ge agglomerates were typically $\leq 10\mu m$. However the Ge secondary phases were positively identified and can be seen in Figure 6.12, with dashed circles outlining the Ge impurities.

The electrical resistivity was increased as the amount of Ge secondary phase was increased. At 300K the electrical resistivity was increased from approximately $1.5 m\Omega\,cm$ to $1.8 m\Omega\,cm$ for $Ge_{17}Sb_2Te_{20}$+2.0%Ge, which is well beyond the $\pm 8\%$ uncertainty associated

with measuring electrical resistivity. The Seebeck coefficient was also increased as the concentration of Ge was increased. The highest increase in Seebeck coefficient occurred for $Ge_{17}Sb_2Te_{20}$+0.50%Ge. Unlike in the case of using Sb impurities the Seebeck coefficient decreased for the higher concentrations of 1.0%Ge and 2.0%Ge. The electrical resistivity and Seebeck coefficient can be seen in Figure 6.13(a) and (b), respectively.

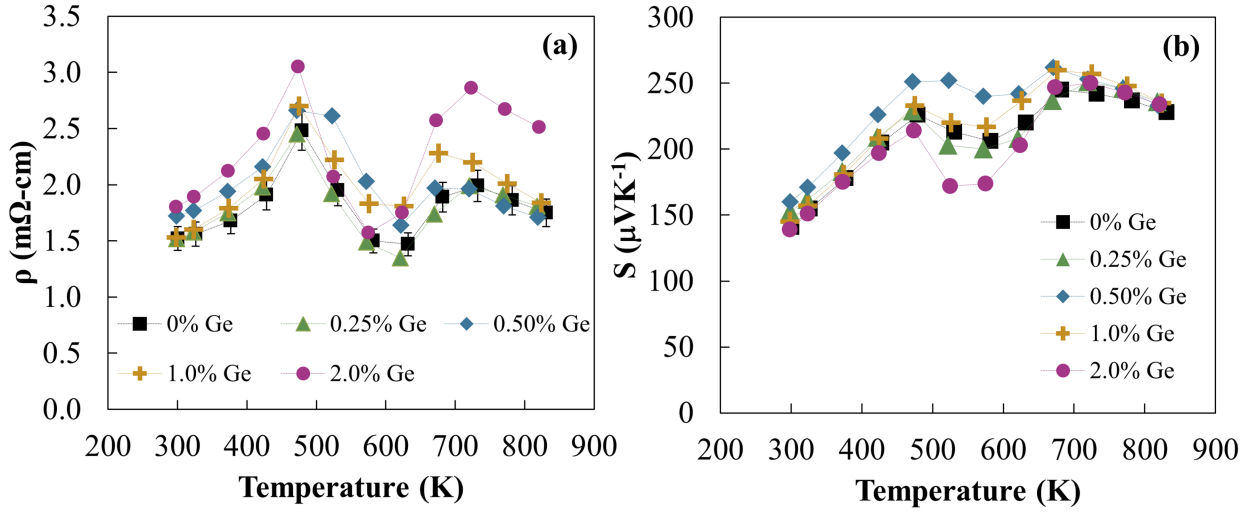

Figure 6.13: (a) Electrical resistivity versus temperature for $Ge_{17}Sb_2Te_{20}$+Ge_x, seen here with ±8% error bars on $Ge_{17}Sb_2Te_{20}$. (b) Seebeck coefficient versus temperature for $Ge_{17}Sb_2Te_{20}$+Ge_x.

By increasing the Ge impurity concentration an optimization in the power factor was achieved. Specifically the power factor was increased across all temperatures, with peak values around 35μWcm^{-1}K^{-2}. The power factor versus temperature can be seen in Figure 6.14(a). Hall measurements revealed that the Ge impurities act as scattering sites for the holes and lowered the hole mobility to less than 20cm^{2}V^{-1}s^{-1}. As can be seen in Figure 6.14(b) the decrease in hole mobility coincides with an optimization of the power factor.

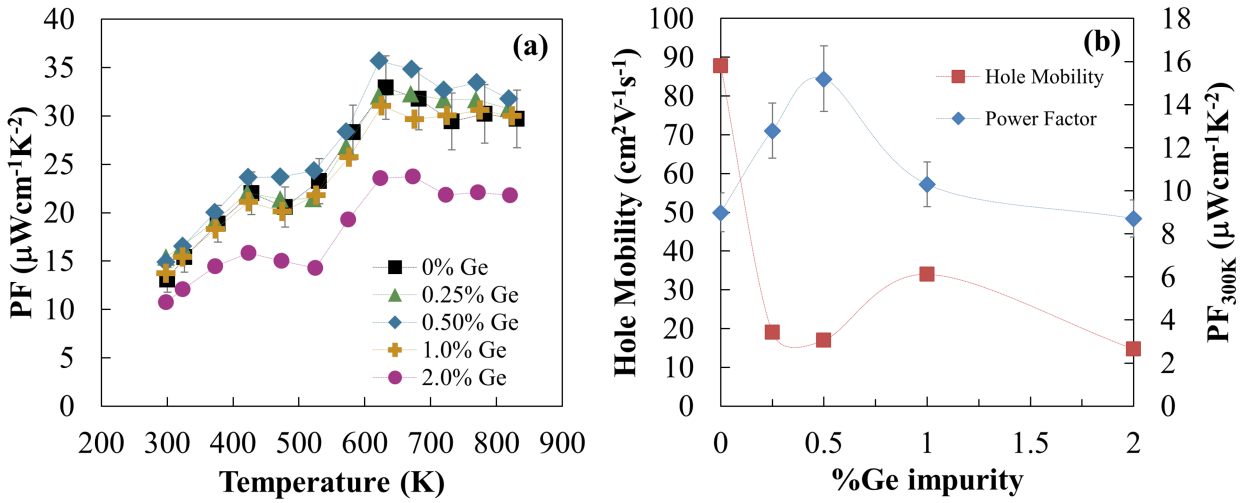

Figure 6.14: (a) Power factor as a function of temperature for $Ge_{17}Sb_2Te_{20}$+Ge_x, with $8 \pm \%$ error bars on $Ge_{17}Sb_2Te_{20}$. (b) Hole mobility and room temperature power factor as a function of %Ge secondary phase. A clear complement can be discerned.

The increase of the Seebeck coefficient, electrical resistivity, and ultimately power factor, can be explained by a change in the energy landscape of the scattering relaxation time, $\tau(E)$. This phenomenon was explained in greater mathematical detail in the previous section on $Ge_{17}Sb_2Te_{20}$+Sb_x. In addition to scattering the charge carriers to increase the resistive nature of the electrical transport in $Ge_{17}Sb_2Te_{20}$ the Ge impurities scatter phonons to decrease the lattice thermal conductivity. The thermal conductivity versus temperature for $Ge_{17}Sb_2Te_{20}$+Ge_x can be seen in Figure 6.15.

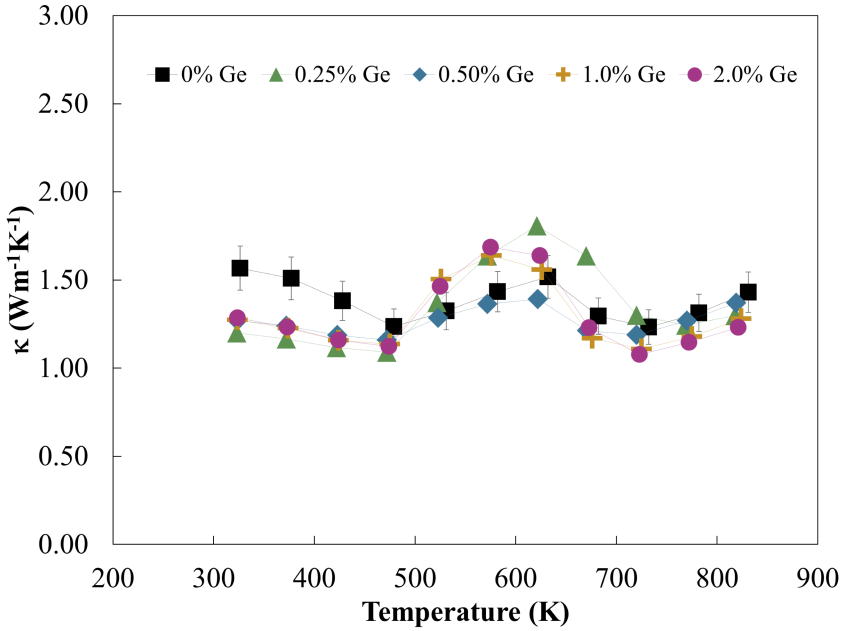

Figure 6.15: Thermal conductivity versus temperature for $Ge_{17}Sb_2Te_{20}$+Ge_x, seen here with ±8% error bars on $Ge_{17}Sb_2Te_{20}$, which was calculated from the measurement techniques used.

The Ge impurities led to a decreased thermal conductivity and increased power factor, which led to an overall increase in the ZT for 0.25% and 0.50% added Ge. The ZT versus temperature and ZT versus %Ge impurity can be seen in Figure 6.16.

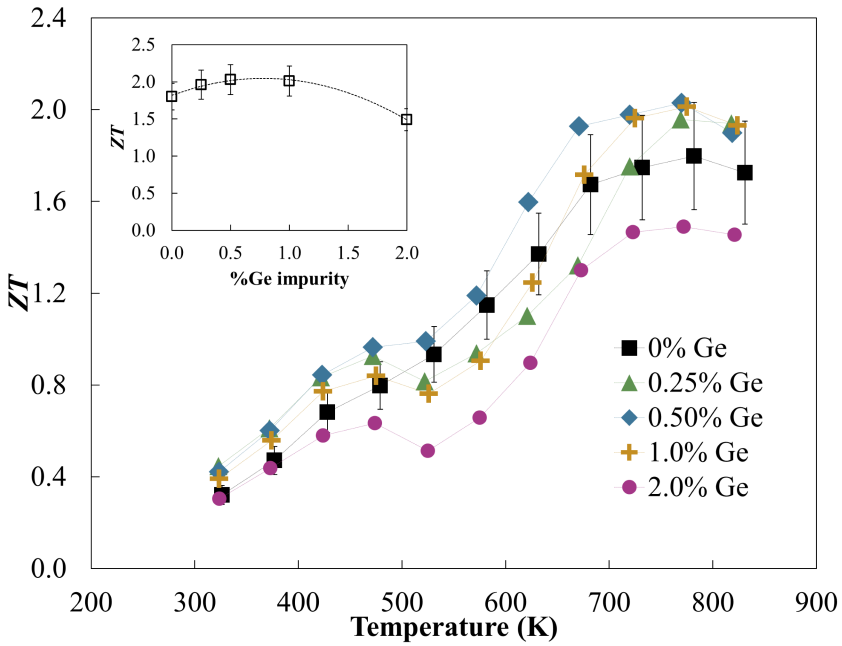

Figure 6.16: ZT versus temperature for $Ge_{17}Sb_2Te_{20}$ with 0.25, 0.50, 1.0, and 2.0% added Ge, seen here with ±13% error bars on $Ge_{17}Sb_2Te_{20}$. A large enhancement was observed for $Ge_{17}Sb_2Te_{20}$ with 0.5%Ge impurity.

6.2.3 Conclusion

In this study Ge was added to the pristine phase of $Ge_{17}Sb_2Te_{20}$ in controlled amounts of 0.25, 0.50, 1.0, and 2.0 atomic percent. Similar to the results of $Ge_{17}Sb_2Te_{20}$+Sb_x, it was found that the Ge impurities were approximately a few microns in size and caused an increase in the electrical resistivity and Seebeck coefficient. The power factor was enhanced significantly and the thermal conductivity was decreased. Hall measurements showed no significant change in the hole concentration, rather the hole mobility was decreased with the introduction of Ge impurities. This was explained by a changing of the scattering relaxation time as the secondary phase of Ge acted as a scattering site for both charge carriers and heat carrying phonons. The ZT of $Ge_{17}Sb_2Te_{20}$ with the presence of Ge impurities increased for 0.25 and 0.50% added Ge. The results of the two studies, $Ge_{17}Sb_2Te_{20}$+Sb_x

and $Ge_{17}Sb_2Te_{20}$+Ge_x, revealed a promising avenue for engineering new high-ZT materials. However a more comprehensive understanding of why the enhancements from secondary phases is possible is necessary and will be presented in the next section.

6.3 Enhancing ZT Using Composites

In 1991 Bergman and Levy published work to examine the thermoelectric properties of composites in hopes of finding a new way to enhance the ZT of materials. To begin, the basic macroscopic equation for a thermoelectric material is defined concisely as:

$$\mathbf{J} = \widehat{Q}\nabla\psi \tag{6.1}$$

where

$$\mathbf{J} \equiv \begin{pmatrix} -\mathbf{J}_E/e \\ -\mathbf{J}_S/k \end{pmatrix} \tag{6.2}$$

$$\nabla\psi \equiv \begin{pmatrix} \nabla(e\phi) \\ \nabla(kT) \end{pmatrix} \tag{6.3}$$

$$\widehat{Q} \equiv \begin{pmatrix} Q_{11} & Q_{12} \\ Q_{21} & Q_{22} \end{pmatrix} \equiv \begin{pmatrix} \sigma/e^2 & \sigma S/ek \\ \sigma S/ek & \gamma/k^2T \end{pmatrix} \tag{6.4}$$

$\mathbf{J}_E$ is the electrical current density, defined as $\mathbf{J}_E = \sigma\mathbf{E}$, where $\mathbf{E}$ is the electric field and σ is the electrical conductivity. $\mathbf{J}_S$ is the heat flux given as $T\mathbf{J}_S = -\gamma\nabla T$, where γ is the coefficient of thermal conductivity. The usual thermal conductivity under zero electric current, κ, can be defined in terms of gamma as $\kappa = \gamma - T\sigma S^2$. The quantity S is the

thermoelectric coefficient, or the absolute Seebeck coefficient, and ϕ is the voltage. The thermoelectric figure of merit can therefore be defined in terms of the determinant of $\widehat{Q}$ as follows:

$$ZT = \frac{Q_{12}^2}{det\widehat{Q}} = \left(\frac{Q_{11}Q_{22}}{Q_{12}^2} - 1\right)^{-1} \tag{6.5}$$

For composite media a volumed averaged value for the effective transport is defined in terms of the macroscopic field $E^{(1)} = (\mathbf{E}_1^{(1)}, \mathbf{E}_2^{(2)})$ and $E^{(2)} = (\mathbf{E}_1^{(2)}, \mathbf{E}_2^{(2)})$. The components of the volume-averaged effective transport matrix, $\widehat{Q}_e$ then become defined as seen below.

$$Q_{e11} = \frac{1}{V}\int dV(Q_{11}{E_1^{(1)}}^2 - Q_{22}{E_2^{(1)}}^2) \tag{6.6}$$

$$Q_{e22} = \frac{1}{V}\int dV(Q_{22}{E_2^{(2)}}^2 - Q_{11}{E_1^{(2)}}^2) \tag{6.7}$$

$$Q_{e12} = \frac{1}{V}\int dV(Q_{12}(\mathbf{E}_1^{(1)} \cdot \mathbf{E}_2^{(2)}) - \mathbf{E}_1^{(2)} \cdot \mathbf{E}_2^{(1)}) \tag{6.8}$$

Q_{e11}, Q_{e22}, and Q_{e12} each contain off-diagonal terms which make the integrals too complex to analytically solve. The following assumptions are therefore invoked in order to simplify the equations: (1) $Q_{12} \ll Q_{11}$ and $Q_{12} \ll Q_{22}$; (2) each component of the composite is homogeneous and isotropic. The first assumption allows for the coupled terms in equations (6.6), (6.7), and (6.8) to be neglected, and the second assumption allows the transport coefficients to be pulled out of the integrand since they would be isotropic and homogeneous and therefore independent of volume. After further simplifying it was found that the effective figure of merit for the composite could never exceed the figure of merit of any one of the

components alone. This negative result was the first theoretical study of composites and showed that working with composites would not show promising results.

In 1993 Hicks and Dresselhaus established that if composites could be made which were nanostructured the figure of merit of a material could be substantially enhanced.[49] The original work by Bergman and Levy assumed that the composite media were large in nature (μm and larger). Hicks and Dresselhaus found that nanostructured composites did not fall under the original assumptions of the composite medium theory and could therefore be used to alter the electronic density of states, which in turn would enhance the Seebeck coefficient. Energy filtering, which was essentially an extension of the work by Hicks and Dresselhaus, theoretically showed that using nanostructured secondary phases with specific band gap offsets relative to the host matrix could result in a "filtering" of the hot electrons, which in turn would lead to enhanced power factor.[145] Bulk nanostructured thermoelectric materials have repeatedly been shown to yield enhancements in ZT for a number of materials.[146, 147, 140, 101, 148]

In 1999 Bergman and Fel found that the power factor of a composite mixture of two materials could be enhanced.[149] When such an enhancement is possible based on the materials it is realized for a microstructure with parallel slabs or coated spheres. In the study, it was theoretically proposed that composites of Ni-$CoSb_3$, PbTe-Bi_2Te_3, Ni-$YbAl_3$, Al-$(Bi_2Te_3)_{0.2}(Sb_2Te_3)_{0.8}$, and constantan-$(Bi_2Te_3)_{0.2}(Sb_2Te_3)_{0.8}$ would all exhibit increased power factor. Recently a number of studies have shown that using secondary phases can lead to enhancements in ZT. Zhang, *et al* synthesized PbTe with MnTe secondary phases. The result was an increase in the thermoelectric performance as well as the hardness of the material.[150] Wu, *et al* synthesized PbTe-with precipitated PbS secondary phases, which resulted in a broad plateau in ZT and a ZT_{avg} value of approximately 1.5.[151]. It was

recently shown that the incorporation of ZnO as a secondary phase in the chalcopyrite compound $CuInTe_2$ can lead to enhancements in power factor and the ZT overall.[152] A number of studies on the skutterudite compound $CoSb_3$ have shown that the incorporation of secondary phases such as $AgSbTe_2$ and InSb can result in the decrease of thermal conductivity as well as an enhancement of power factor and therefore ZT.[153, 140] In 2014 Zou, *et al* used the secondary phase of β-Zn_4Sb_3 in Cu_3SbSe_4 to enhance the ZT value up to 1.3 by increasing the energy dependence of the scattering relaxation time.[154]

Perhaps more interesting are the recent studies on Ge-Sb-Te compounds and using secondary phases to enhance the thermoelectric performance. In 2015 Fahrnbauer, *et al* used microstructured $CoSb_3$ in $(GeTe)_mSb_2Te_3$ alloys to enhance the ZT.[155] In the same year Fahrnbauer *et al* found that secondary phases of $CoGe_2$ were effective in enhancing the ZT of $Ge_{12}Sb_2Te_{15}$, $Ge_{17}Sb_2Te_{20}$, and $Ge_{19}Sb_2Te_{22}$.[156] The results of these studies were similar in nature to the work described in the previous sections on using Sb and Ge secondary phases to enhance the ZT of $Ge_{17}Sb_2Te_{20}$. Figure 6.17 shows the ZT versus temperature results for a number of Ge-Sb-Te compounds from this work and others, which use microstructured secondary phases to enhance ZT.

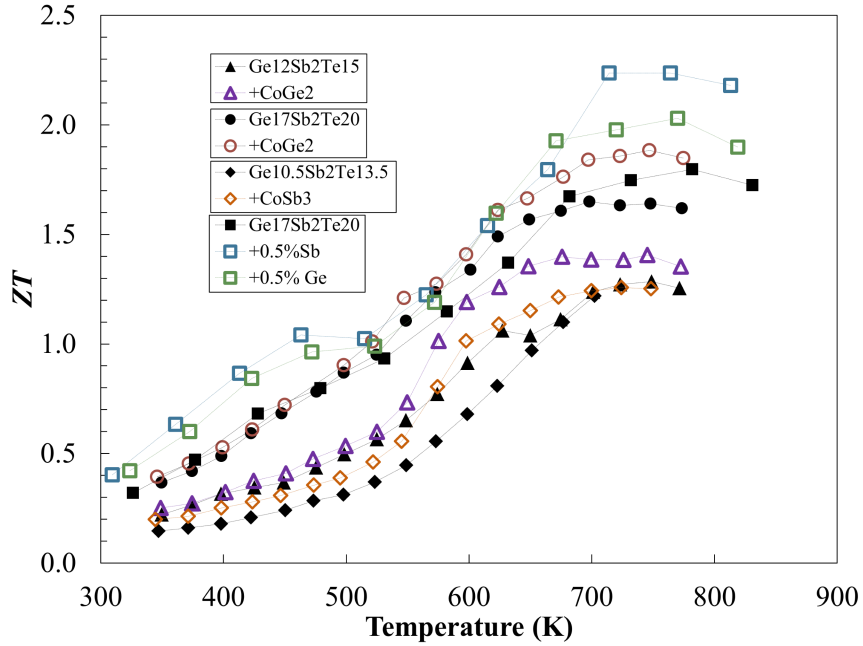

Figure 6.17: ZT as a function of temperature for a number of microstructured composites which utilize $(GeTe)_xSb_2Te_3$ alloys. Specifically $Ge_{12}Sb_2Te_{15}$ with precipitates of $CoGe_2$ from [156]. $Ge_{17}Sb_2Te_{20}$ with precipitates of $CoGe_2$ from [156]. $Ge_{10.5}Sb_2Te_{13.5}$ with precipitated $CoSb_3$ from [155]. $Ge_{17}Sb_2Te_{20}$ with impurities of Sb and Ge from [144] and [157], respectively.

The results seen in Figure 6.17 directly contradict the conclusions reached by Bergman and Levy. The caveat to the potential for using composites in thermoelectric applications can be pinpointed to the assumptions made by Bergman and Levy in their original paper. The assumptions that $Q_{12} \ll Q_{11}$ and $Q_{12} \ll Q_{22}$ have important implications for the overall conclusions one would reach when developing an effective medium theory for thermoelectrics. Recall the earlier equation for the figure of merit in terms of $\widehat{Q}$:

$$ZT = \frac{Q_{12}^2}{det\widehat{Q}} = \left(\frac{Q_{11}Q_{22}}{Q_{12}^2} - 1 \right)^{-1} \tag{6.9}$$

The important part of the equation lies in the components of $\widehat{Q}$. One can therefore

condense the argument down to Δ_e, which is defined in equation (6.10).

$$\Delta_e = \frac{Q_{e12}^2}{Q_{e11}Q_{e22}} \tag{6.10}$$

The simplicity of this equation stems from the assumptions made about the relative magnitudes of Q_{e11}, Q_{e22}, and Q_{e12}. If one does not assume/neglect the off-diagonal terms from (6.6), (6.7), and (6.8), Δ_e becomes

$$\Delta_e = \frac{[Q_{12}\int dV(\mathbf{E}_1^{(1)}\cdot\mathbf{E}_2^{(2)}) - \int dV(\mathbf{E}_1^{(2)}\cdot\mathbf{E}_2^{(1)})]^2}{(Q_{11}\int dV {E_1^{(1)}}^2 - Q_{22}\int dV {E_2^{(1)}}^2)(Q_{22}\int dV {E_2^{(2)}}^2 - Q_{11}\int dV {E_1^{(2)}}^2)} \tag{6.11}$$

Equation (6.11) contains terms which are nonsymmetric with respect to the matrix $\widehat{Q}$, and essentially imply that the intrinsic electrical and thermal properties of each component of the composite are coupled and not independent of one another. The original assumptions on Q_{11}, Q_{22}, and Q_{12} effectively lead to the conclusion that ZT is much less than unity for all components of the composite. The apparent disagreement between this theoretical work and the recent experimental findings on composite thermoelectrics then becomes resolved in that, for materials with $ZT \geq 1$ the constraints may not apply. This leaves room for developing new thermoelectric composite materials with greater thermoelectric efficiency and improved mechanical stability.

6.4 $\mathbf{Ge_{17+x}Sb_{2-x}Te_{20}}$

The charge carrier concentration in semiconductors is a highly sensitive variable which is important for the optimization of thermoelectric performance. An effective means of tun-

ing the carrier concentration for thermoelectric materials is through the incorporation of foreign atoms which either introduce an acceptor state (p-type) or a donor state (n-type). The compound of interest, $Ge_{17}Sb_2Te_{20}$, has yet to be studied for optimization of the carrier concentration. However, other studies on doping various $(GeTe)_xSb_2Te_3$ alloys show the potential to enhance the ZT of $Ge_{17}Sb_2Te_{20}$. Welzmiller, *et al* studied Mn doping in $Ge_4Sb_2Te_7$, which resulted in a ZT enhancement as well as the introduction of a ferromagnetic phase from the Mn ions.[131] Welzmiller, *et al* also observed a nearly 300% increase in ZT by doping Cr on the Ge site in $GeSb_2Te_4$.[132] In 2015 Welzmiller, *et al* studied the effects of Cd doping on $(GeTe)_nSb_2Te_3$ and $(SnTe)_nSb_2Te_3$ compounds and found that Cd increased the density of states effective mass and led to an increase in the Seebeck coefficient, which allowed for slight increases in the power factor, and ZT overall.[122] Perumal, et al used Sb and Bi to optimize the carrier concentration and power factor of GeTe, resulting in ZT values well in excess of unity.[158, 159]

The following work studied the thermoelectric properties of $Ge_{17+x}Sb_{2-x}Te_{20}$. Doping on the nominally trivalent Sb site with divalent Ge should introduce one acceptor (or hole) per atomic substitution, increase the carrier concentration, and therefore decrease the electrical resistivity. Also, by adjusting the Ge and Sb stoichiometry we avoid using additional elements for doping and therefore keep the cost of synthesis down.

6.4.1 Experimental Procedures

Samples of $Ge_{17+x}Sb_{2-x}Te_{20}$ ($x = 0, 0.04, 0.16, 0.20, 0.24, 0.30, 0.40$, which correspond to $0, 2, 8, 10, 12, 15$, and 20% Ge, respectively) were synthesized by placing stoichiometric amounts of elemental Ge, Sb, and Te in evacuated and sealed silica ampoules. The samples were then melted at 1173K, held for 12h, and water quenched. After quenching, the samples were

annealed at 863K, for 24h and water quenched. The obtained ingots were ball milled for 5min. The powder was densified using SPS at 738K for 5min under 45MPa of pressure. All samples had density $\geq 99\%$ theoretical density. High temperature Hall measurements were measured by Alexander Page at the University of Michigan, Department of Physics, under the advice of Dr. Ctirad Uher. The carrier concentration was determined using the Hall effect, under the single carrier approximation using the relation $R_h = 1/pe$. The Hall coefficient was measured using an AC 4-probe method in a custom built apparatus from 293K to 773K under a maximum field of $\pm$1T. The samples were in a 1atm Argon environment to prevent oxidation.

6.4.2 Results and Discussion

All samples were single phase and showed no secondary phases, which was verified using X-ray diffraction and SEM/EDS. As Ge was doped onto the Sb site of $Ge_{17}Sb_2Te_{20}$ the rocksalt symmetry began to degrade to a rhombohedral structure. Specifically, at $x = 0.16$ significant peak splitting began to take place above 40° two-theta and below 30° two-theta. The X-ray patterns for all samples as well as a reference GeTe sample can be seen in Figure 6.18.

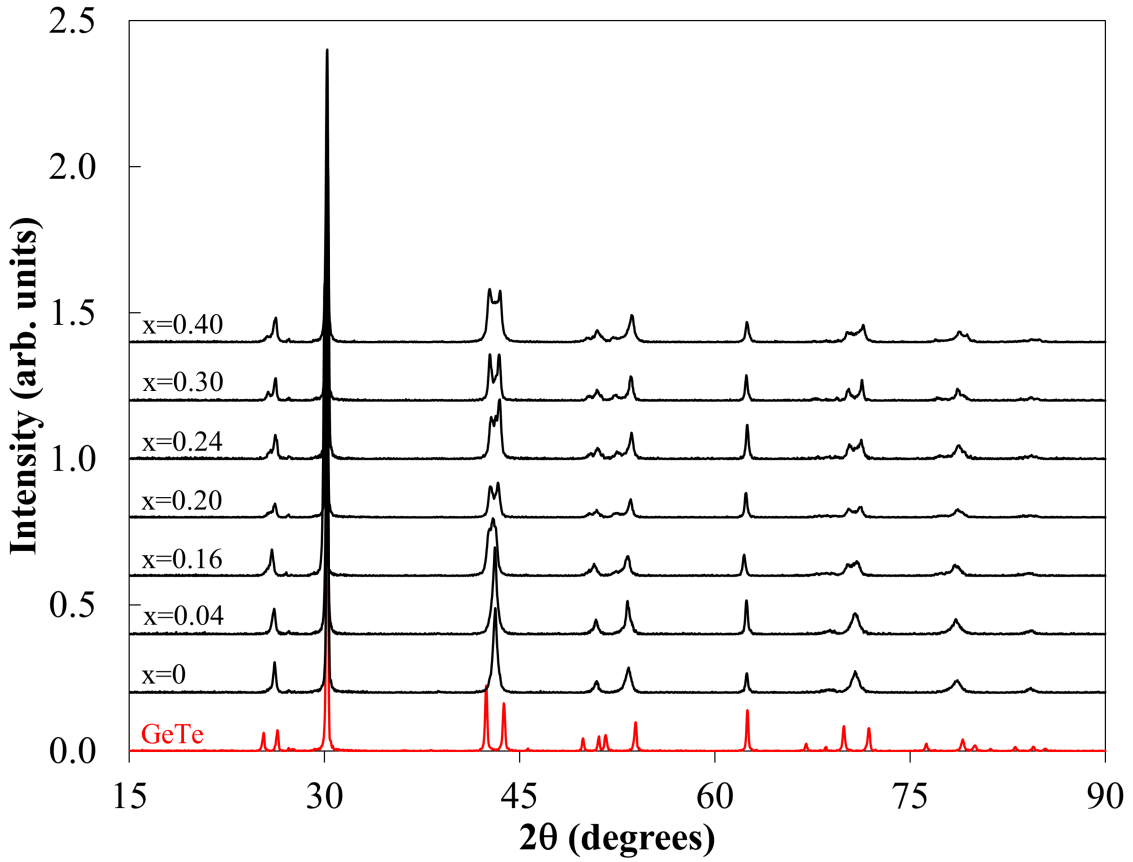

Figure 6.18: X-ray patterns for $Ge_{17+x}Sb_{2-x}Te_{20}$ showing $x = 0$, 0.04, 0.16, 0.20, 0.24, 0.30, and 0.40. The rocksalt structure of $Ge_{17}Sb_2Te_{20}$ begins to transition to rhombohedral as Ge content is increased. GeTe is shown as a reference for the rhombohedral peak splitting taking place.

Quenching $Ge_{17}Sb_2Te_{20}$ from the annealing temperature of 863K yields a rocksalt crystal structure with a lattice parameter of 5.92Å. The rhombohedral crystal is typically described in mathematical terms as a hexagonal cell, but can also be visualized as a distortion along the [111] direction of the rocksalt unit cell. The angle between the **a**,**b**, and **c** crystal directions can also be used to characterize the rhombohedral crystal structure, i.e. for GeTe the distorted cubic angle is 88.26°.[160] As the amount of Ge doped for Sb is increased the c-axis lattice parameter of the hexagonal unit cell is increased and the cubic angle of the rocksalt structure is decreased, as can be seen in Figure 6.19.

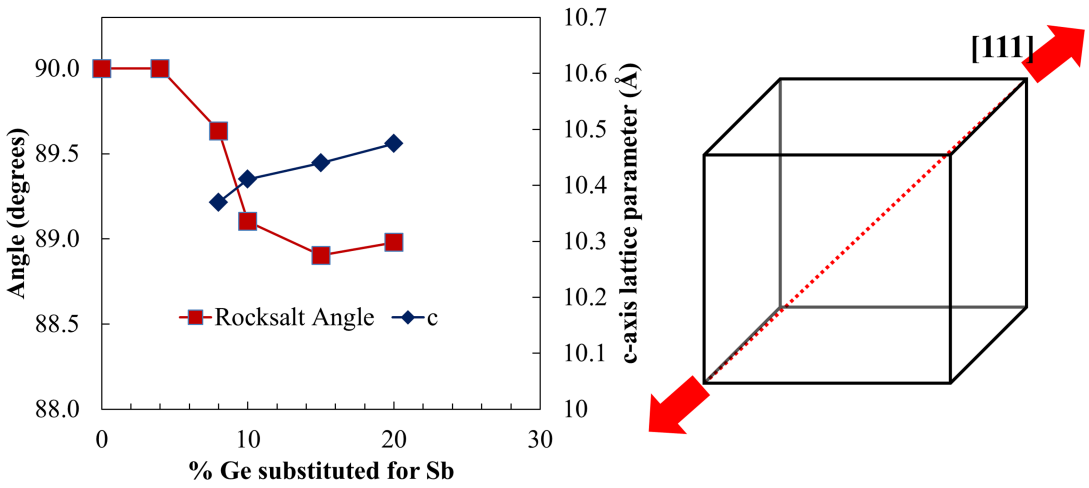

rystal direction of the rocksalt unit cell. The transition is fundamentally driven by the expansion of the c-axis lattice parameter of the rhombohedral-hexagonal unit cell.]As the amount of Ge doped onto the Sb site of $Ge_{17}Sb_2Te_{20}$ is increased the angle of the rocksalt unit cell (normally 90°) is decreased. This can be understood as a distortion along the [111] crystal direction of the rocksalt unit cell. The transition is fundamentally driven by the expansion of the c-axis lattice parameter of the rhombohedral-hexagonal unit cell.

Figure 6.19: c

The electrical resistivity as a function of temperature can be seen in Figure 6.20. The electrical resistivity is decreased with increased Ge content, from a value of 1.6mΩ cm for $Ge_{17}Sb_2Te_{20}$ at 300K to 0.5mΩ cm for $Ge_{17.4}Sb_{1.6}Te_{20}$ (20% Ge) at room temperature. This trend is suggestive that Ge is replacing Sb and increasing the hole concentration. Most interesting to note is the changing nature of the phase transition. For $Ge_{17}Sb_2Te_{20}$ there is a sharp decrease in the electrical resistivity, which is due to the phase transition from cubic to rhombohedral. However, the resistivity of the 20% doped sample displays a true metallic nature and continues to increase with temperature. It is hypothesized that this occurs because the increased number of holes makes the electronic transition, which is originally

due to an increase in hole mobility, less pronounced, as the hole mobility should decrease with increased hole concentration.[12]

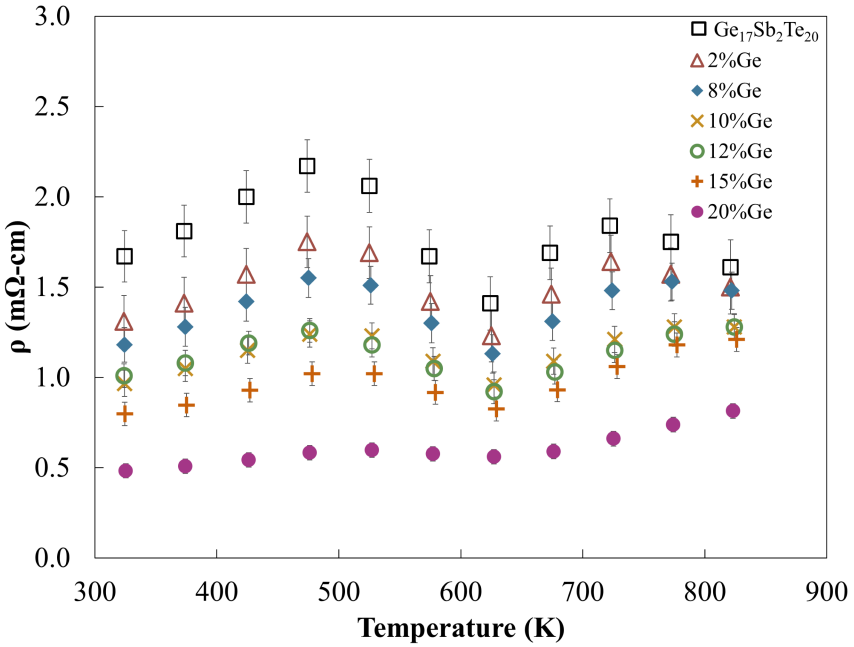

Figure 6.20: Electrical resistivity versus temperature $Ge_{17+x}Sb_{2-x}Te_{20}$. As the amount of Ge dopant is increased the electrical is decreased to values below 1.0mΩ cm.

The Seebeck coefficient is also decreased with increased Ge dopant, as can be seen in Figure 6.21. The Seebeck coefficient, in general, is inversely proportional to the Seebeck coefficient. The decreasing Seebeck coefficient seen in Figure 6.21 is further indication that the carrier concentration is increased due to Ge doping.

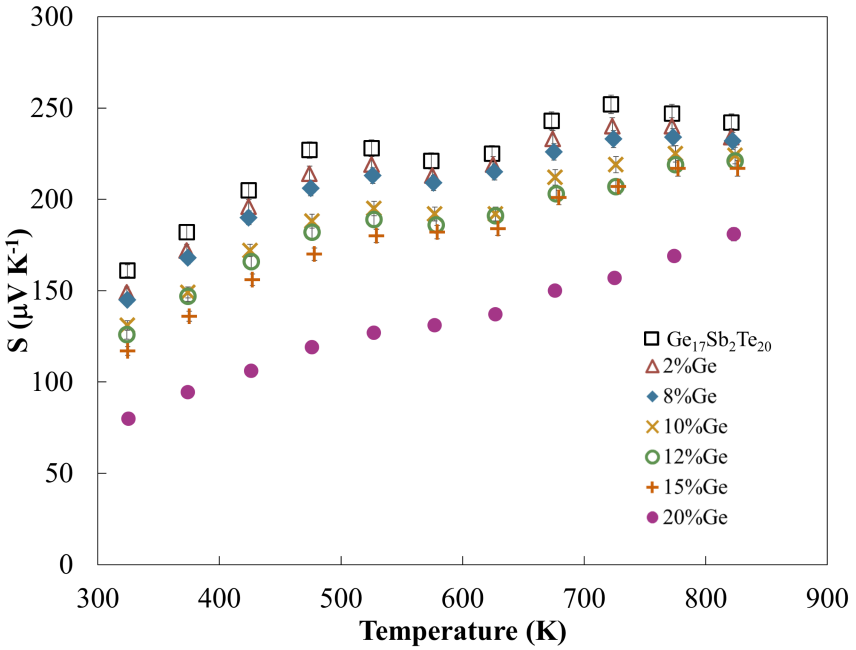

Figure 6.21: Seebeck coefficient versus temperature for $Ge_{17+x}Sb_{2-x}Te_{20}$. The decrease in Seebeck coefficient as the concentration of Ge dopant is increased is further indication that the hole concentration is increased from doping.

Because of the decreased Seebeck coefficient and electrical resistivity the power factor was increased approximately 30% from a peak value of $35\mu Wcm^{-1}K^{-2}$ for $Ge_{17}Sb_2Te_{20}$ to a peak value of $43\mu Wcm^{-1}K^{-2}$ for 15% Ge doped $Ge_{17}Sb_2Te_{20}$. For higher dopant concentrations the power factor is decreased. The power factor as a function of temperature can be seen in Figure 6.22.

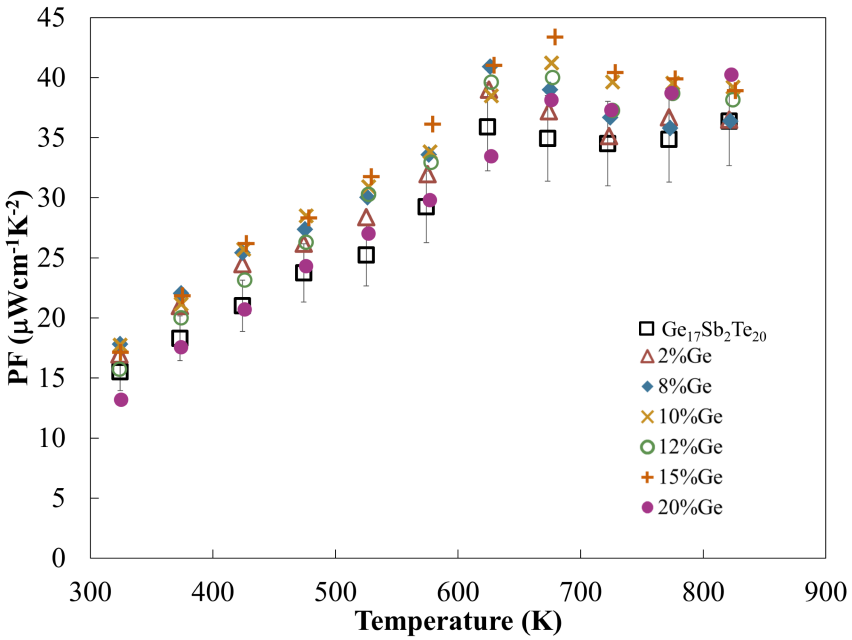

Figure 6.22: Power factor versus temperature for $Ge_{17+x}Sb_{2-x}Te_{20}$, seen here with the calculated error bars of approximately ±10% for $Ge_{17}Sb_2Te_{20}$. An optimal power factor was reached for 15%Ge; higher concentrations caused a decrease.

The thermal conductivity was increased with increased Ge content, with 20%Ge showing values in excess of 2 across the entire temperature range. The thermal conductivity as a function of temperature can be seen in Figure 6.23(a). The increase in thermal conductivity is believed to come primarily from the electronic contribution to thermal conductivity. To estimate the lattice thermal conductivity, the electronic contribution to thermal conductivity was subtracted from the total thermal conductivity. The Lorenz number was calculated by fitting the Seebeck coefficient to a single parabolic band model with acoustic phonon scattering assumed to be the dominant scattering mechanism. The result of the calculated lattice thermal conductivity as a function of temperature can be seen in Figure 6.23(b). All values display temperature independence with values around $1 Wm^{-1}K^{-1}$. There is a slight spread in the values, but all agree within the uncertainty of ±10%.

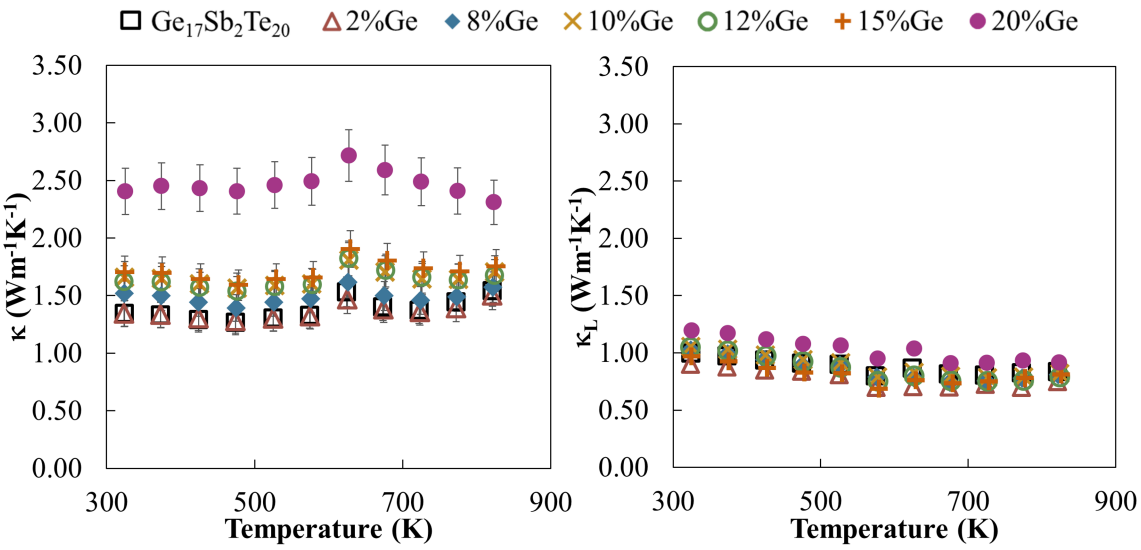

Figure 6.23: (a) Thermal conductivity versus temperature, with calculated error bars of on average 9%. The increasing trend in total thermal conductivity is due to an increased electronic contribution, as was verified from calculating the lattice thermal conductivity (b).

Despite an increase in the power factor, the ZT for $Ge_{17+x}Sb_{2-x}Te_{20}$ is decreased as the concentration of Ge is increased, as can be seen in Figure 6.24. As aforementioned in the introductory chapters, the thermoelectric properties which comprise ZT are contraindicated and there is an optimum charge carrier concentration to maximize ZT for a given material and temperature. The decreased ZT is therefore indicative of *overdoping*, which would mean the carrier concentration is either already optimized for $Ge_{17}Sb_2Te_{20}$ or should be decreased. To confirm this hypothesis the hole concentration from $300 - 723$K was measured using the Hall effect on $Ge_{17}Sb_2Te_{20}$ and 10%, 15%, and 20% Ge doped $Ge_{17}Sb_2Te_{20}$. The carrier concentration for the samples as a function of temperature can be seen in Figure 6.25

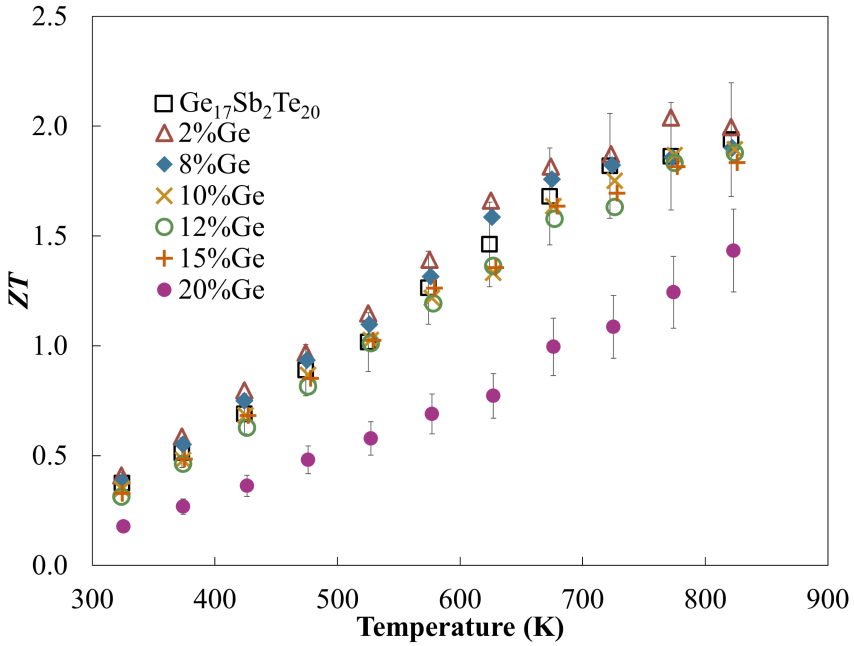

Figure 6.24: ZT versus temperature for $Ge_{17+x}Sb_{2+x}Te_{20}$, seen here with the calculated error bars of on average $\pm 13\%$ on $Ge_{17}Sb_2Te_{20}$ and $Ge_{17.4}Sb_{1.6}Te_{20}$ (20% Ge). There is a systematic decrease with increased Ge doping.

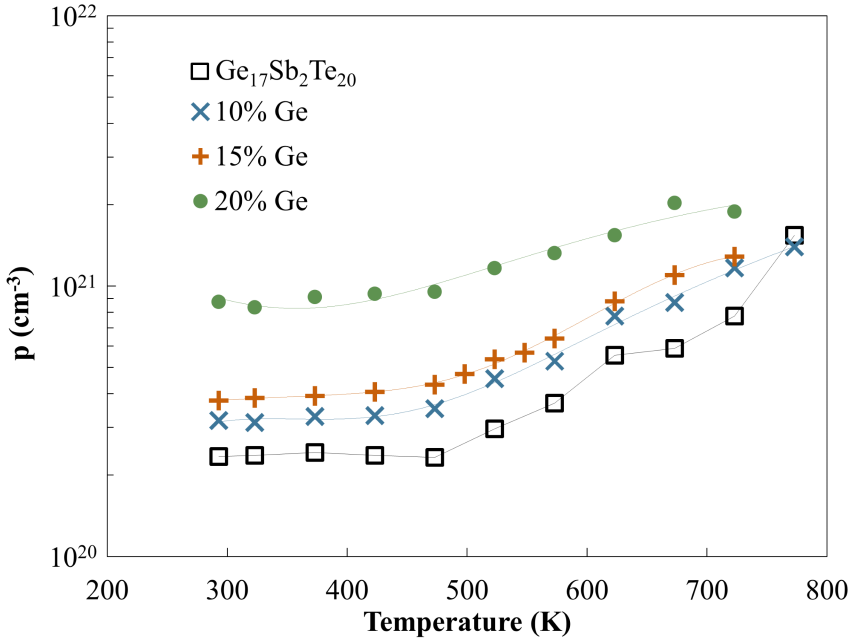

Figure 6.25: Hole concentration versus temperature ($300 - 700$K) for 0%, 10%, 15%, and 20% Ge doped $Ge_{17}Sb_2Te_{20}$.

To better understand the nature of doping and electrical transport a single parabolic band

model was used to determine the maximum ZT as a function of carrier concentration for $Ge_{17}Sb_2Te_{20}$. The specific parameters used can be seen in Table 6.2. The Seebeck coefficient versus carrier concentration for 300K, 423K, 523K, 623K, and 723K can be seen along with experimental values in Figure 6.26(b). There is good agreement between experiment and model aside from experimental values which are lower than expected. These deviations could be due to additional contributions to transport from a degenerate light band, which has been observed in other IV-VI compounds.[161]

The expected ZT values as a function of carrier concentration can be seen in Figure 6.26(a) along with experimental values. The undoped $Ge_{17}Sb_2Te_{20}$ was shown to yield the highest ZT values at each temperature, which was further verified by experiment.

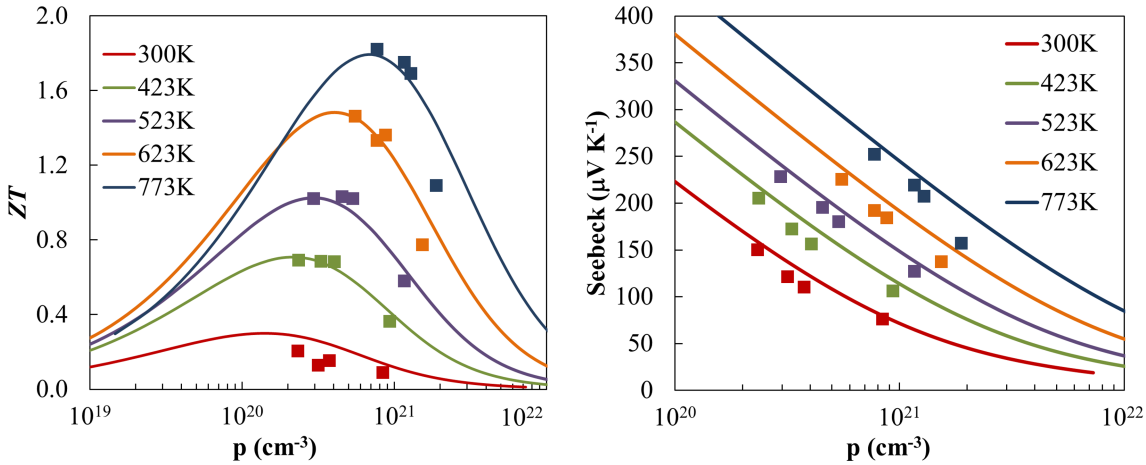

Figure 6.26: (a) Calculated ZT values as a function of carrier concentration for $Ge_{17}Sb_2Te_{20}$ assuming single parabolic band behavior for 300K, 423K, 523K, 623K, and 773K. Experimental values are plotted as squares for each temperature, showcasing the optimized ZT values of $Ge_{17}Sb_2Te_{20}$. (b) Seebeck coefficient versus carrier concentration (Pisarenko plot) for $Ge_{17}Sb_2Te_{20}$ at 300K, 423K, 523K, 623K, and 773K assuming single parabolic band behavior, with experimental points shown as squares for each temperature.

Table 6.2: The parameters necessary for calculating the thermoelectric properties of $Ge_{17}Sb_2Te_{20}$ using a single parabolic band model. Temperature, T, lattice thermal conductivity, κ_L, effective mass, m^* (determined from Seebeck coefficient), and intrinsic carrier mobility, μ_o, calculated using the mobility found from Hall measurements.

SPB Model Parameters for $Ge_{17}Sb_2Te_{20}$			
T	κ_L	m*	μ_o
300	0.995	3.52	23.54
423	0.935	4.2	16.65
523	0.899	4.84	12.5
623	0.805	6.01	9.58
773	0.823	7.3	5.51

6.4.3 Conclusion

In this study Ge was substituted onto the Sb site in $Ge_{17}Sb_2Te_{20}$ in an attempt to increase the hole concentration and optimize the thermoelectric properties. It was found that the rocksalt unit cell of $Ge_{17}Sb_2Te_{20}$ was distorted along the [111] crystal direction as the Ge content increased. The electrical resistivity and Seebeck coefficient were consistently and significantly reduced which resulted in a maximization of power factor, with values around $40\mu Wcm^{-1}K^{-2}$ for $Ge_{17.3}Sb_{1.7}Te_{20}$. The lattice thermal conductivity was unchanged, but because of the decreased electrical resistivity the electronic contribution to thermal conductivity increased which resulted in an increased total thermal conductivity. The ZT was therefore decreased for the higher doping percentages of Ge. Using the results from temperature dependent Hall measurements the thermoelectric properties were modeled using a single parabolic band model, where it was shown that the ZT is maximized between 300K and 700K for carrier concentrations coinciding with $Ge_{17}Sb_2Te_{20}$. To increase ZT for this compound the focus of future work should therefore rest on either reducing lattice thermal conductivity or increasing hole mobility and/or Seebeck coefficient.

Chapter 7

Concluding Remarks

Thermoelectric materials represent a unique research endeavor for alleviating the energy demands of society. By means of the Seebeck effect, thermoelectric materials can directly convert wasted heat into electrical energy. Unfortunately the efficiency of power generation is constrained by a unitless parameter called the figure of merit, ZT, which is dependent on materials properties which are by their nature contraindicated. Novel materials engineering such as reduced dimensionality, doping, particle size control, and intuitive materials selection are needed to enhance ZT and achieve commercial viability.

This work studied the synthesis, processing, and thermoelectric properties of Ge-Sb-Te based compounds and alloys. GeTe rich alloys of GeTe and Sb_2Te_3 were synthesized using a conventional solid state process and spark plasma sintering. It was found that the thermoelectric properties were highly sensitive to the concentration of vacancies in theses alloys. The thermal conductivity was decreased with the introduction of Sb_2Te_3, but the power factor was also decreased. This resulted in an optimized peak ZT of approximately 1.9 for $Ge_{17}Sb_2Te_{20}$.

The compound Ge_4SbTe_5 was studied for thermoelectric applications. This compound does not lie on the GeTe-Sb_2Te_3 tie-line and contains no vacancies in the unit cell. The compound exhibited inherently high ZT values due to the low thermal conductivity and high

temperature metallic state, which resulted in power factor values in excess of $20\mu Wcm^{-1}K^{-2}$. Studies of substituting Sn on the Ge atomic site and Bi on the Sb atomic site were conducted. It was found that the introduction of these point defects successfully lowered the thermal conductivity. The band gap of Ge_4SbTe_5 was sensitive to atomic substitutions and decreased upon introduction of Bi and Sb, which resulted in an overall decrease of the power factor, and therefore ZT. Doping was also performed to tune the concentration. Na, which is monovalent, was substituted for divalent Ge. This resulted in an increase in the hole concentration, as was hypothesized. The Seebeck coefficient also decreased with Na doping, and resulted in a decrease in overall power factor and ZT. Ga, which has one less electron than Ge, was also studied as a dopant. Ga was shown to not be stable as a dopant, even for small amounts such as 1%. This resulted in the creation of the secondary phase Ga_2Te_3.

The alloy $Ge_{17}Sb_2Te_{20}$ was also studied. This stoichiometry was found to exhibit the highest thermoelectric properties among the GeTe-Sb_2Te_3 alloys from Chapter 3. After a typical solid state synthesis of melting, quenching, and annealing the material was found to exist in a metastable rocksalt phase. Upon heating a phase transition to the stable rhombohedral phase takes place. This phase transition occurs because of the ordering of vacancies, which are randomly assorted on the cation site of the metastable rocksalt unit cell. The phase transition from metastable rocksalt to rhombohedral has also been classified as a insulator-metal transition, because of the change in electrical resistivity. It was found that the method of synthesis has a direct effect on the crystal structure and microstructure of $Ge_{17}Sb_2Te_{20}$. By quenching directly from the melt, microstructured secondary phases of Ge and Sb exist and were found to enhance the thermoelectric performance. The effects of both Sb as a secondary phase and Ge as secondary phase in $Ge_{17}Sb_2Te_{20}$ were isolated and studied. It was found that these secondary phases enhance the charge carrier scattering and

provide an enhancement in the Seebeck coefficient. Additionally, the thermal conductivity was reduced with the introduction of these secondary phases. These enhancements led to consistent ZT values in excess of 2 for both Sb and Ge secondary phases. Finally, a study on altering the carrier concentration through doping was conducted, $Ge_{17+x}Sb_{2-x}Te_{20}$. It was found that altering the Ge/Sb ratio was a method towards successfully tuning the hole concentration. The power factor and thermal conductivity were enhanced, which ultimately led to decreases in ZT. Fortunately this work also allowed for modeling of the thermoelectric properties as a function of carrier concentration. It was found that $Ge_{17}Sb_2Te_{20}$ has an ideal carrier concentration. Therefore, to enhance the ZT of this specific compound reductions in the lattice thermal conductivity through ball-milling and atomic substitutions should be conducted.

7.1 Future Work and Interesting Projects

There is much work needed on GeTe-Sb_2Te_3 alloys and compounds to understand their potential for thermoelectric power generation. This thesis showed the impressive thermoelectric performance of these materials, specifically $Ge_{17}Sb_2Te_{20}$. There lacks sufficient studies in the literature on the crystallographic nature of $Ge_{17}Sb_2Te_{20}$. It would therefore be wise to conduct a more thorough study of the fundamental elastic and crystallographic properties of this compound. Here we give a brief presentation of ideas for future projects which would be fruitful for understanding and engineering this interesting class of materials.

Recently, Levin *et al* showed that rare earth dopants such Yb, Dy, and Er enhanced that Seebeck coefficient in GeTe and TAGS-85 by introduction of a magnetic moment.[162, 163] This enhancement in Seebeck resulted in an increase in power factor as well. Based on

the similarity between these compounds and $Ge_{17}Sb_2Te_{20}$, it is believed that these dopants could yield positive results. The study of adjusting the Ge/Sb ratio in $Ge_{17}Sb_2Te_{20}$ showed that the charge carrier concentration of this compound was ideal for optimized ZT. However, it would be interesting to study the effects of increased vacancy concentration on the thermoelectric properties of $Ge_{17}Sb_2Te_{20}$. Introduction of vacancies could potentially lower the lattice thermal conductivity and enhance the Seebeck coefficient be introducing additional point defect scattering for both phonons and holes.

The studies in this work along with others in the field on using secondary phases to enhance thermoelectric performance warrants substantial attention. Future work on this subject should include studies on the size of the secondary phases, the importance of geometry, and types of materials used as a secondary phase. It is believed that magnetic materials and ultra-low thermal conductivity materials could be of particular interest as a secondary phase.

Lowering the lattice thermal conductivity is an avenue that has not been explored yet. To achieve this, future studies on reducing particle/grain size using high energy ball milling would be fruitful. It has been shown in this work and others that substituting isovalent atoms such as Sn on the Ge site and Se on the Te site can reduce lattice thermal conductivity, but can also change the electronic bandgap, which reduces the power factor. Co-substituting Sn and Se, written as $Ge_{17-x}Sn_xSb_2Te_{20-y}Se_y$, could be used to control the bandgap and reduce thermal conductivity. This method would introduce phonon scattering point defects, but also the bandgap could be specifically engineered as Sn substitution would decrease the bandgap while Se would increase the bandgap. It should be noted however that the rate of change for Sn and Se could be unequal and should be studied independently first. Also, the solubility of Sn and Se has been shown to not be 100% in other Ge-Sb-Te compounds.[164,

157] These represent just some of the interesting avenues to further understand the complex nature of thermoelectric phenomena in Ge-Sb-Te compounds.

Ge-Sb-Te phase change materials have been extensively researched for nonvolatile memory storage and are now the front runner for replacing less attractive RAM based technologies. It is now being realized that these materials, which are Pb-free and easy to synthesize, are competitive with today's state of the art thermoelectric compounds. If the thermoelectric properties could be optimized, one might envision a future application which incorporates these materials in a hybrid setup. By exploiting the memory storage capabilities and high thermoelectric performance, the memory technologies of tomorrow could also utilize the wasted heat in computers and electronic devices.

REFERENCES

REFERENCES

[1] Lawrence Livermore National Laboratory. Estimated U.S. Energy Use in 2014, 2015.

[2] Lawrence Livermore National Laboratory. US Carbon 2013, 2014.

[3] Daniel A. Lashof and Dilip R. Ahuja. Relative contributions of greenhouse gas emissions to global warming. *Nature*, 344(6266):529–531, apr 1990.

[4] Xu Lu, Donald T. Morelli, Yi Xia, Fei Zhou, Vidvuds Ozolins, Hang Chi, Xiaoyuan Zhou, and Ctirad Uher. High Performance Thermoelectricity in Earth-Abundant Compounds Based on Natural Mineral Tetrahedrites. *Adv. Energy Mater.*, 3(3):342–348, mar 2013.

[5] Bruce A. Cook, Matthew J. Kramer, Joel L. Harringa, Mi-Kyung Han, Duck-Young Chung, and Mercouri G. Kanatzidis. Analysis of Nanostructuring in High Figure-of-Merit Ag1-xPbmSbTe2+m Thermoelectric Materials. *Adv. Funct. Mater.*, 19(8):1254–1259, apr 2009.

[6] I. Kudman. Thermoelectric properties of p-type PbTe-PbSe alloys. *J. Mater. Sci.*, 7(9):1027–1029, sep 1972.

[7] Osamu Yamashita, Shoichi Tomiyoshi, and Ken Makita. Bismuth telluride compounds with high thermoelectric figures of merit. *J. Appl. Phys.*, 93(1):368–374, jan 2003.

[8] T.J J. Seebeck. Ueber die magnetische Polarisation der Metalle und Erze durch Temperaturdifferenz. *Ann. Phys.*, 82(3):253–286, 1826.

[9] J. C. Peltier. Nouvelles expériences sur la caloricité des courants électriques. *Ann. Chim. Phys.*, 56(371):371, 1834.

[10] H J Goldsmid and R W Douglas. the Use of Semiconductors in Thermoelectric Refrigeration. *Br. J. Appl. Phys.*, 5(NOV):386–390, 1954.

[11] H J Goldsmid. Principles of thermoelectric devices. *Br. J. Appl. Phys.*, 11(6):209–217, jun 1960.

[12] S. O. Kasap. Principles of electronic materials and devices, 2006.

[13] V. Fistul. *Heavily Doped Semiconductors*. Plenum Press, New York, 1969.

[14] A. F. Ioffe. *Physics of Semiconductors*. Academic Press, New York, 1960.

[15] Charles Kittel. *Introduction to Solid State Physics*. John Wiley & Sons Inc., New York, 3 edition, 1967.

[16] V. Fistul. *Heavily Doped Semiconductors*. Plenum Press, New York, 1969.

[17] S. M. Sze. *Physics of Semiconductor Devices*. Wiley-Interscience, second edition, 1981.

[18] A. I. Anselm and B. M. Askerov. Quantum theory of the Nernst-Ettinghasen effect in semiconductors(Nerst-Ettingshausen coefficient calculated for scattering at short duration potential, at impurity ions and at acoustic oscillations. *Fiz. Tverd. Tela*, (9):31–41, 1967.

[19] J. Bardeen and W. Shockley. Deformation Potentials and Mobilities in Non-Polar Crystals. *Phys. Rev.*, 80(1):72–80, oct 1950.

[20] E. Conwell and V. F. Weisskopf. Theory of Impurity Scattering in Semiconductors. *Phys. Rev.*, 77(3):388–390, feb 1950.

[21] Raymond Serway and John Jewett. *Principles of Physics*. Brooks/Cole-Thomson Learning, 4 edition, 2006.

[22] R. A. Matula. Electrical resistivity of copper, gold, palladium, and silver. *J. Phys. Chem. Ref. Data*, 8(4):1147–1298, oct 1979.

[23] Terry M. Tritt. Thermoelectric Phenomena, Materials, and Applications. *Annu. Rev. Mater. Res.*, 41:433–448, 2011.

[24] N Cusack and P Kendall. The Absolute Scale of Thermoelectric Power at High Temperature. *Proc. Phys. Soc.*, 72(5):898–901, nov 1958.

[25] A. Bentien, S. Johnsen, G. K. H. Madsen, B. B. Iversen, and F. Steglich. Colossal Seebeck coefficient in strongly correlated semiconductor FeSb 2. *Europhys. Lett.*, 80(1):17008, oct 2007.

[26] P. M. Chaikin. An Introduction to Thermopower for Those Who Might Want to Use It to Study Organic Conductors and Superconductors. In V.Z. Kresin and W.A. Little, editors, *Org. Supercond.*, pages 101–115. Plenum Press, New York, 1990.

[27] R. W. Christy. Ionic Materials. In Irving B. Cadoff and Edward Miller, editors, *Thermoelectr. Mater. Devices*, pages 173–183. Reinhold Publishing Corporation, New York, 1960.

[28] R. W. Fritts. Lead Telluride Alloys and Junctions. In Irving Cadoff and Edward Miller, editors, *Thermoelectr. Mater. Devices1*, pages 143–172. Reinhold Publishing Corporation, New York, 1960.

[29] G Jeffrey Snyder and Eric S Toberer. Complex thermoelectric materials. *Nat. Mater.*, 7, 2008.

[30] Baron Fourier and Joseph Jean-Baptiste. *The analytical theory of heat*. The University Press, 1878.

[31] R. Berman. *Thermal Conduction in Solids*. Oxford University Press, Oxford, 1 edition, 1976.

[32] P.J. Price. CXXXV. Ambipolar thermodiffusion of electrons and holes in semiconductors. *London, Edinburgh, Dublin Philos. Mag. J. Sci.*, 46(382):1252–1260, nov 1955.

[33] G. E. Pikus. Thermo-and galvanomagnetic effects in semiconductors taking account of variations in carrier concentration. II. Galvanomagnetic effects in strong fields. Thermal conductivity of electrons and excitons. *Zk. tekh. Fiz.*, 26:36–50, 1956.

[34] L. Genzel. Der Anteil der Warmestrahlung bei Warmeleitungsvorgangen. *Zeitschrift fu Phys.*, 135(2):177–195, apr 1953.

[35] David J. Griffiths. *Intoduction to Quantum Mechanics*. Pearson Prentice Hall, Upper Saddle River, 2 edition, 2005.

[36] R. Peierls. Zur kinetischen Theorie der Wärmeleitung in Kristallen. *Ann. Phys.*, 395(8):1055–1101, 1929.

[37] Donald T. Morelli and Glen a. Slack. High Lattice Thermal Conductivity Solids. In *High Therm. Conduct. Mater.*, pages 37–68. Springer-Verlag, New York, 2006.

[38] Micheline Roufosse and P. G. Klemens. Thermal Conductivity of Complex Dielectric Crystals. *Phys. Rev. B*, 7(12):5379–5386, jun 1973.

[39] R. Berman, E. L. Foster, and J. M. Ziman. Thermal Conduction in Artificial Sapphire Crystals at Low Temperatures. I. Nearly Perfect Crystals. *Proc. R. Soc. London A Math. Phys. Eng. Sci.*, 231(1184), 1955.

[40] F D Rosi, J P Dismukes, and E F Hockings. Semiconductor materials for thermoelectric power generation up to 700 C. *Electr. Eng.*, 79(6):450–459, 1960.

[41] Hiromichi Ohta, Kenji Sugiura, and Kunihito Koumoto. Recent progress in oxide thermoelectric materials: P-type Ca3Co4O9 and n-Type SrTiO3. *Inorg. Chem.*, 47(19):8429–8436, 2008.

[42] Jing Li, Jiehe Sui, Yanling Pei, Celine Barreteau, David Berardan, Nita Dragoe, Wei Cai, Jiaqing He, and Li-Dong Zhao. A high thermoelectric figure of merit ZT $>$ 1 in Ba heavily doped BiCuSeO oxyselenides. *Energy Environ. Sci.*, 5(9):8543, 2012.

[43] G. S. Nolas, D. T. Morelli, and Terry M. Tritt. SKUTTERUDITES: A Phonon-Glass-Electron Crystal Approach to Advanced Thermoelectric Energy Conversion Applications. *Annu. Rev. Mater. Sci.*, 29(1):89–116, aug 1999.

[44] Jihui Yang and Thierry Caillat. T hermoelectric Materials for Space. 31(March 2006):224–229, 2017.

[45] D. Berthebaud, O.I. Lebedev, and A. Maignan. Thermoelectric properties of n-type cobalt doped chalcopyrite Cu1xCoxFeS2 and p-type eskebornite CuFeSe2. *J. Mater.*, 1(1):68–74, mar 2015.

[46] Winston D. Carr and Donald T. Morelli. Influence of doping and solid solution formation on the thermoelectric properties of chalcopyrite semiconductors. *J. Alloys Compd.*, 630(630):277–281, may 2015.

[47] Xu Lu and Donald T Morelli. Natural mineral tetrahedrite as a direct source of thermoelectric materials. *Phys. Chem. Chem. Phys.*, 15(16):5762–6, apr 2013.

[48] Tiejun Zhu, Yintu Liu, Chenguang Fu, Joseph P. Heremans, Jeffrey G. Snyder, and Xinbing Zhao. Compromise and Synergy in High-Efficiency Thermoelectric Materials. *Adv. Mater.*, page 1605884, mar 2017.

[49] L. D. Hicks and M. S. Dresselhaus. Effect of quantum-well structures on the thermomagnetic figure of merit. *Phys. Rev. B*, 47(19):727–731, 1993.

[50] T. C. Harman, D. L. Spears, and M. J. Manfra. High thermoelectric figures of merit in PbTe quantum wells. *J. Electron. Mater.*, 25(7):1121–1127, 1996.

[51] T Koga, Tc Harman, Sb Cronin, and Ms Dresselhaus. Mechanism of the enhanced thermoelectric power in (111)-oriented n-type PbTe/Pb(1-x)Eu(x) Te multiple quantum wells. *Phys. Rev. B*, 60(20):14286, 1999.

[52] Yanzhong Pei, Heng Wang, and G J Snyder. Band engineering of thermoelectric materials. *Adv. Mater.*, 24(46):6125–35, dec 2012.

[53] Yanzhong Pei, Xiaoya Shi, Aaron LaLonde, Heng Wang, Lidong Chen, and G Jeffrey Snyder. Convergence of electronic bands for high performance bulk thermoelectrics. *Nature*, 473(7345):66–9, may 2011.

[54] SK Mishra, S Satpathy, and O Jepsen. Electronic structure and thermoelectric properties of bismuth telluride and bismuth selenide. *J. Phys. Condens. Matter*, 9(2):461–470, 1997.

[55] Jiong Yang, P. Qiu, R. Liu, L. Xi, S. Zheng, W. Zhang, L. Chen, D. J. Singh, and Jihui Yang. Trends in electrical transport of p-type skutterudites RFe 4Sb 12 (R = Na, K, Ca, Sr, Ba, La, Ce, Pr, Yb) from first-principles calculations and Boltzmann transport theory. *Phys. Rev. B - Condens. Matter Mater. Phys.*, 84(23):20–24, 2011.

[56] L.-D. Zhao, Gangjian Tan, Shiqiang Hao, Jiaqing He, Yanling Pei, Hang Chi, Heng Wang, Shengkai Gong, Huibin Xu, Vinayak P Dravid, Ctirad Uher, G Jeffrey Snyder, Chris Wolverton, and Mercouri G Kanatzidis. Ultrahigh power factor and thermoelectric performance in hole-doped single-crystal SnSe. *Science (80-.).*, 351(6269):141–144, 2016.

[57] A. F. Ioffe. *Semiconductor Thermoelements and Thermoelectric Cooling*. Infosearch Limited, London, 1957.

[58] R. Berman, P. T. Nettley, F. W. Sheard, A. N. Spencer, R. W. H. Stevenson, and J. M. Ziman. The Effect of Point Imperfections on Lattice Conduction in Solids. *Proc. R. Soc. A Math. Phys. Eng. Sci.*, 253(1274):403–419, dec 1959.

[59] B. Abeles. Lattice thermal conductivity of disordered semiconductor alloys at high temperatures. *Phys. Rev.*, 131(5):1906–1911, 1963.

[60] Glen A. Slack. Design Concepts for Improved Thermoelectric Materials. *MRS Proc.*, 478:47, jan 1997.

[61] Glen Slack. New Materials and Performance Limits for Thermoelectric Cooling. In *CRC Handb. Thermoelectr.*, chapter 34. CRC Press, jul 1995.

[62] G. S. Nolas, J. L. Cohn, G. A. Slack, and S. B. Schujman. Semiconducting Ge clathrates: Promising candidates for thermoelectric applications. *Appl. Phys. Lett.*, 73(2):178–180, 1998.

[63] D. T. Morelli, T. Caillat, J. P. Fleurial, A. Borshchevsky, J. Vandersande, B. Chen, and C. Uher. Low-temperature transport properties of p-type CoSb3. *Phys. Rev. B*, 51(15):9622–9628, 1995.

[64] G. S. Nolas, G. a. Slack, D. T. Morelli, T. M. Tritt, and a. C. Ehrlich. The effect of rare-earth filling on the lattice thermal conductivity of skutterudites. *J. Appl. Phys.*, 79(8):4002, 1996.

[65] Xu Lu, Donald T. Morelli, Yi Xia, Fei Zhou, Vidvuds Ozolins, Hang Chi, Xiaoyuan Zhou, and Ctirad Uher. High Performance Thermoelectricity in Earth-Abundant Compounds Based on Natural Mineral Tetrahedrites. *Adv. Energy Mater.*, 3(3):342–348, mar 2013.

[66] Wei Lai, Yuxing Wang, Donald T. Morelli, and Xu Lu. From Bonding Asymmetry to Anharmonic Rattling in Cu12Sb4S13 Tetrahedrites: When Lone-Pair Electrons Are Not So Lonely. *Adv. Funct. Mater.*, 25(24):3648–3657, jun 2015.

[67] Kanishka Biswas, Jiaqing He, Ivan D. Blum, Chun-IWu, Timothy P. Hogan, David N. Seidman, Vinayak P. Dravid, and Mercouri G. Kanatzidis. High-performance bulk thermoelectrics with all-scale hierarchical architectures. *Nature*, 490(7421):570–570, 2012.

[68] R R Schaller. Moore's law: past, present and future. *Spectrum, IEEE*, 34(6):52–59, 1997.

[69] References Cited, Oklahoma City, and Related U-s-Application Data. (12) United States Patent. 1(12):0–4, 2003.

[70] A. T. Waterman. The Electrical Conductivity of Molybdenite. *Phys. Rev.*, 21(5):540–549, may 1923.

[71] Stanford R. Ovshinsky. Reversible Electrical Switching Phenomena in Disordered Structures. *Phys. Rev. Lett.*, 21(20):1450–1453, nov 1968.

[72] Inventors Michael P Doyle, Glenn Dale, Hojae Choi, and B City. (12) UnIted States Patent. 2(12), 2012.

[73] S. Raoux, G. W. Burr, M. J. Breitwisch, C. T. Rettner, Y.-C. Chen, R. M. Shelby, M. Salinga, D. Krebs, S.-H. Chen, H.-L. Lung, and C. H. Lam. Phase-change random access memory: A scalable technology. *IBM J. Res. Dev.*, 52(4.5):465–479, 2008.

[74] Noboru Yamada, Eiji Ohno, Kenichi Nishiuchi, Nobuo Akahira, and Masatoshi Takao. Rapid-phase transitions of GeTe-Sb2Te3 pseudobinary amorphous thin films for an optical disk memory. *J. Appl. Phys.*, 69(5):2849–2856, 1991.

[75] Noboru Yamada. Erasable Optical Materials. (September):1–3, 1996.

[76] M. Libera and M. Chen. Time-resolved reflection and transmission studies of amorphous Ge-Te thin-film crystallization. *J. Appl. Phys.*, 73(5):2272–2282, 1993.

[77] Matthias Wuttig and Noboru Yamada. Phase-change materials for rewriteable data storage. *Nat. Mater.*, 6(11):824–832, 2007.

[78] F Curtis Michel. Physical review letters 1. 48(9):1392–1395, 1982.

[79] Wojciech Wełnic, Silvana Botti, Lucia Reining, and Matthias Wuttig. Origin of the optical contrast in phase-change materials. *Phys. Rev. Lett.*, 98(23):1–4, 2007.

[80] Kostiantyn Shportko, Stephan Kremers, Michael Woda, Dominic Lencer, John Robertson, and Matthias Wuttig. Resonant bonding in crystalline phase-change materials. *Nat. Mater.*, 7(8):653–658, aug 2008.

[81] Linus Pauling. The Nature of the Chemical Bond. *J. Chem. Educ.*, 69(7):656, jul 1992.

[82] G. Lucovsky and R. M. White. Effects of Resonance Bonding on the Properties of Crystalline and Amorphous Semiconductors. *Phys. Rev. B*, 8(2):660, 1973.

[83] Saikat Mukhopadhyay, Jifeng Sun, Alaska Subedi, Theo Siegrist, and David J. Singh. Competing covalent and ionic bonding in Ge-Sb-Te phase change materials. *Sci. Rep.*, 6:25981, may 2016.

[84] M. P. Jiang, M. Trigo, I. Savić, S. Fahy, É. D. Murray, C. Bray, J. Clark, T. Henighan, M. Kozina, M. Chollet, J. M. Glownia, M. C. Hoffmann, D. Zhu, O. Delaire, A. F. May, B. C. Sales, A. M. Lindenberg, P. Zalden, T. Sato, R. Merlin, and D. A. Reis. The origin of incipient ferroelectricity in lead telluride. *Nat. Commun.*, 7:12291, jul 2016.

[85] Jean-Pierre Gaspard. Structure of covalently bonded materials: From the Peierls distortion to Phase-Change Materials. *Comptes Rendus Phys.*, 17(3-4):389–405, mar 2016.

[86] Wei Zhang, Matthias Wuttig, and Riccardo Mazzarello. Effects of stoichiometry on the transport properties of crystalline phase-change materials. *Sci. Rep.*, 5:13496, jan 2015.

[87] Sangyeop Lee, Keivan Esfarjani, Tengfei Luo, Jiawei Zhou, Zhiting Tian, and Gang Chen. Resonant bonding leads to low lattice thermal conductivity. *Nat. Commun.*, 5:1–8, apr 2014.

[88] Saikat Mukhopadhyay, Lucas Lindsay, and David J Singh. Optic phonons and anisotropic thermal conductivity in hexagonal Ge2Sb2Te5. *Sci. Rep.*, 6:37076, nov 2016.

[89] K S Siegert, F R L Lange, E R Sittner, H Volker, C Schlockermann, T Siegrist, and M Wuttig. Impact of vacancy ordering on thermal transport in crystalline phase-change materials. *Reports Prog. Phys.*, 78(1):013001, 2015.

[90] Peter B. Littlewood. Structure and bonding in narrow gap semiconductors. *Crit. Rev. Solid State Mater. Sci.*, 11(3):229–285, 1983.

[91] K. Momma and F. Izumi. VESTA 3 for three-dimensional visualization of crystal, volumetric and morphology data. *J. Appl. Crystallogr.*, 44:1272–1276, 2011.

[92] N. F. Mott. Metal-insulator transition. *Rev. Mod. Phys.*, 40(4):677–683, 1968.

[93] T Siegrist, P Jost, H Volker, M Woda, P Merkelbach, C Schlockermann, and M Wuttig. Disorder-induced localization in crystalline phase-change materials. *Nat. Mater.*, 10(3):202–208, 2011.

[94] Sergei Baranovski, editor. *Charge Transport in Disordered Solids with Applications in Electronics*. John Wiley & Sons Inc., England, 2006.

[95] P. W. Anderson. Absence of diffusion in certain random lattices. *Phys. Rev.*, 109(5):1492–1505, 1958.

[96] Mordechai Segev, Yaron Silberberg, and Dimitris Christofilos. Anderson localization of light. *Nat. Photonics*, 7(February):197–204, 2013.

[97] Giulia Semeghini, Manuele Landini, Patricia Castilho, Sanjukta Roy, Giacomo Spagnolli, Andreas Trenkwalder, Marco Fattori, Massimo Inguscio, and Giovanni Modugno. Measurement of the mobility edge for 3D Anderson localization. *Nat. Phys.*, 11(7):554–559, 2015.

[98] Tianping Ying, Yueqiang Gu, Xiao Chen, Xinbo Wang, Shifeng Jin, Linlin Zhao, Wei Zhang, and Xiaolong Chen. Anderson localization of electrons in single crystals: LixFe7Se8. *Sci. Adv.*, 2(2):4–11, 2016.

[99] Peter Jost, Hanno Volker, Annika Poitz, Christian Poltorak, Peter Zalden, Tobias Schäfer, Felix R. L. Lange, Rüdiger M. Schmidt, Bernd Holländer, Matti R. Wirtssohn, and Matthias Wuttig. Disorder-Induced Localization in Crystalline Pseudo-Binary GeTe-Sb2Te3 Alloys between Ge3Sb2Te6 and GeTe. *Adv. Funct. Mater.*, pages n/a–n/a, may 2015.

[100] W Williams, E H Putley, R Mansfield, S A Salam, A F Joffe, L S Stil, and R W Wright. Thermoelectric and Galvanomagnetic effects in Lead Selenide and Telluride. *Proc. Phys. Soc.*, 68(1):35–42, 1954.

[101] Gangjian Tan, Fengyuan Shi, Shiqiang Hao, Li-Dong Zhao, Hang Chi, Xiaomi Zhang, Ctirad Uher, Chris Wolverton, Vinayak P. Dravid, and Mercouri G. Kanatzidis. Non-equilibrium processing leads to record high thermoelectric figure of merit in PbTeSrTe. *Nat. Commun.*, 7:12167, jul 2016.

[102] A. F. Ioffe. Heat transfer in semiconductorsl. *1Canadian J. Phys.*, pages 1342–1355, 1956.

[103] Yi Zhang, Jianjun Dong, Paul R C Kent, Jihui Yang, and Changfeng Chen. Intrinsic low thermal conductivity in weakly ionic rocksalt structures. 020301:4–8, 2015.

[104] Z. A. Munir, U. Anselmi-Tamburini, and M. Ohyanagi. The effect of electric field and pressure on the synthesis and consolidation of materials: A review of the spark plasma sintering method. *J. Mater. Sci.*, 41(3):763–777, feb 2006.

[105] P.W. Ratke, L., Voorhees. *Growth and Coarsening: Ostwald Ripening in Material Processing*. Springer Berlin Heidelberg, Berlin, Heidelberg, 2002.

[106] Jared Williams. Spark Plasma Sintering: A Brief Survey of Recent Patents. *Recent Patents Mater. Sci.*, 5(3), aug 2012.

[107] W. L. Bragg. The Diffraction of Short Electromagnetic Waves by a Crystal. *Scientia*, 23(45):153, 1929.

[108] S. Cullity, B., Stock. *Elements of X-Ray Diffraction*. Pearson Education Limited, 3rd edition, 2013.

[109] Edwin H. Hall. On the New Action of Magnetism on a Permanent Electric Current. *Am. J. Sci.*, 20(117):161–186, 1880.

[110] Josef Stefan. Über die Beziehung zwischen der Wärmestrahlung und der Temperatur, 1879.

[111] Defoe C. Ginnings. The Measurement of Thermal Conductivity. In Irving Cadoff and Edward Miller, editors, *Thermoelectr. Mater. Devices*, pages 113–132. Reinhold Publishing Corporation, New York, 1960.

[112] G.C. Christakudis, S.K. Plachkova, L.E. Shelimova, and E.S. Avilov. Thermoelectric Figure of Merit of Some Compositions in the System (GeTe)1-x[(Ag2Te)1-y(Sb2Te3)y]x. *Phys. Stat. Sol.*, 128:465, 2006.

[113] P. P. Konstantinov, L. E. Shelimova, E. S. Avilov, M. a. Kretova, and V. S. Zemskov. Thermoelectric Properties of n GeTe · m Sb 2 Te 3 Layered Compounds. *Inorg. Mater.*, 37(7):662, 2001.

[114] Tobias Rosenthal, Matthias N. Schneider, Christian Stiewe, Markus Döblinger, and Oliver Oeckler. Real structure and thermoelectric properties of GeTe-Rich germanium antimony tellurides. *Chem. Mater.*, 23(19):4349–4356, 2011.

[115] Chao An Jong, Weileung Fang, Chain Ming Lee, and Tsung Shune Chin. Mechanical properties of phase-change recording media: GeSbTe films. *Japanese J. Appl. Physics, Part 1 Regul. Pap. Short Notes Rev. Pap.*, 40(5 A):3320–3325, 2001.

[116] Jared B Williams, Edgar Lara-Curzio, Ercan Cakmak, Thomas Watkins, and Donald T Morelli. Enhanced thermoelectric performance driven by high-temperature phase transition in the phase change material Ge4SbTe5. *J. Mater. Res.*, 30(17):2605–2610, sep 2015.

[117] E. Skrabek and D. Trimmer. Properties of General TAGS System. In David Rowe, editor, *CRC Handb. Thermoelectr.*, chapter Thermoelec, pages 267–275. CRC Press LLC, Boca Raton, 1995.

[118] Terry M. Tritt. Thermoelectric Phenomena, Materials, and Applications. *Annu. Rev. Mater. Res.*, 41(1):433–448, aug 2011.

[119] C Wood. Materials for thermoelectric energy conversion. *Reports Prog. Phys.*, 51(4):459–539, apr 1988.

[120] Saskia Buller, Christine Koch, Wolfgang Bensch, Peter Zalden, Roland Sittner, Stephan Kremers, Matthias Wuttig, Ulrich Schürmann, Lorenz Kienle, Thomas Leichtweiß, Jürgen Janek, and Boyke Schönborn. Influence of partial substitution of Te by Se and Ge by Sn on the properties of the blu-ray phase-change material Ge 8Sb 2Te 11. *Chem. Mater.*, 24(18):3582–3590, 2012.

[121] Simon Welzmiller, Tobias Rosenthal, Pirmin Ganter, Lukas Neudert, Felix Fahrnbauer, Philipp Urban, Christian Stiewe, Johannes de Boor, and Oliver Oeckler. Layered germanium tin antimony tellurides: element distribution, nanostructures and thermoelectric properties. *Dalton Trans.*, 43(27):10529–40, jul 2014.

[122] Simon Welzmiller, Felix Fahrnbauer, Felix Hennersdorf, Sascha Dittmann, Michael Liebau, Christina Fraunhofer, Wolfgang G. Zeier, G. Jeffrey Snyder, and Oliver Oeckler. Increasing Seebeck Coefficients and Thermoelectric Performance of Sn/Sb/Te and Ge/Sb/Te Materials by Cd Doping. *Adv. Electron. Mater.*, 1(12):1500266, dec 2015.

[123] L. Vegard. Die Konstitution der Mischkristalle und die Raumfllung der Atome. *Zeitschrift fr Phys.*, 5(1):17–26, jan 1921.

[124] James E. Bernard and Alex Zunger. Optical bowing in zinc chalcogenide semiconductor alloys. *Phys. Rev. B*, 34(8):5992–5995, 1986.

[125] S. Larach, R. E. Shrader, and C. F. Stocker. Anomalous variation of band gap with composition in zinc sulfo- and seleno-tellurides. *Phys. Rev.*, 108(3):587–589, 1957.

[126] Glen A. Slack and C. Glassbrenner. Thermal Conductivity of Germanium from 3K to 1020K. *Phys. Rev.*, 120(3):782–789, nov 1960.

[127] V L Kuznetsov, L A Kuznetsova, and D M Rowe. Effect of nonstoichiometry on the thermoelectric properties of GeBi4Te7. *J. Appl. Phys.*, 85(6):3207–3210, 1999.

[128] Toshiyuki Matsunaga, Rie Kojima, Noboru Yamada, Kouichi Kifune, Yoshiki Kubota, and Masaki Takata. Structures of stable and metastable Ge2Bi2Te 5, an intermetallic compound in a GeTe-Bi2Te3 pseudobinary system. *Acta Crystallogr. Sect. B Struct. Sci.*, 63(3):346–352, 2007.

[129] L E Shelimova, O G Karpinsku, V S Zemskov, and P P Konstantinov. Structural and Electrical Properties of Layered Tetradymite-like Compounds in the GeTe-Bi2Te3 and GeTe–Sb2Te3 Systems. *Inorg. Mater.*, 36(3):235–242, 2000.

[130] Tae-Jin Park, Se-Young Choi, and Myung-Jin Kang. Phase transition characteristics of Bi/Sn doped Ge2Sb2Te5thin film for PRAM application. *Thin Solid Films*, 515(12):5049–5053, 2007.

[131] Simon Welzmiller, Frank Heinke, Paula Huth, Georg Bothmann, Ernst-Wilhelm Scheidt, Gerald Wagner, Wolfgang Scherer, Andreas Pöppl, and Oliver Oeckler. The influence of Mn doping on the properties of Ge4Sb2Te7. *J. Alloys Compd.*, 652:74–82, dec 2015.

[132] Simon Welzmiller, Robert Schlegel, Andreas Pöppl, Georg Bothmann, Ernst-Wilhelm Scheidt, Wolfgang Scherer, and Oliver Oeckler. Doping GeSb2Te4 with Cr3+: Structure and Temperature-Dependent Physical Properties. *Zeitschrift für Anorg. und Allg. Chemie*, 641(12-13):2350–2356, 2015.

[133] Pierre F P Poudeu, Jonathan D'Angelo, Adam D. Downey, Jarrod L. Short, Timothy P. Hogan, and Mercouri G. Kanatzidis. High thermoelectric figure of merit and nanostructuring in bulk p-type Na1-xPbmSbyTem+2. *Angew. Chemie - Int. Ed.*, 45(23):3835–3839, 2006.

[134] Songting Cai, Zihang Liu, Jianyong Sun, Rui Li, Weidong Fei, and Jiehe Sui. Enhancement of thermoelectric properties by Na doping in Te-free p-type AgSbSe2. *Dalt. Trans.*, 44(3):1046–1051, 2015.

[135] Thorsten Schröder, Stefan Schwarzmüller, Christian Stiewe, Johannes de Boor, Markus Hölzel, and Oliver Oeckler. The Solid Solution Series (GeTe)x(LiSbTe2)2(1<x<11) and the Thermoelectric Properties of (GeTe)11(LiSbTe2)2. *Inorg. Chem.*, 2:130916160317001, 2013.

[136] Chang-eun Kim, Ken Kurosaki, Manabu Ishimaru, Hiroaki Muta, and Shinsuke Yamanaka. Effect of Vacancy Distribution on the Thermal Conductivity of Ga2Te3 and Ga2Se3. *J. Electron. Mater.*, 40(5):999–1004, 2011.

[137] S. Sen and D. N. Bose. Electrical and Optical Properties of Single Crystal In2Te3 and Ga2Te3. *Solid State Commun.*, 50(1):39–42, 1984.

[138] Hao Zhu, Jiang Yin, Yidong Xia, and Zhiguo Liu. Ga2Te3 phase change material for low-power phase change memory application. *Appl. Phys. Lett.*, 97(8):083504, 2010.

[139] David J. Bergman and Ohad Levy. Thermoelectric properties of a composite medium. *J. Appl. Phys.*, 70(11):6821, dec 1991.

[140] Jiangying Peng, Liangwei Fu, Qiongzhen Liu, Ming Liu, Junyou Yang, Dale Hitchcock, Menghan Zhou, and Jian He. A study of Yb 0.2 Co 4 Sb 12 AgSbTe 2 nanocomposites: simultaneous enhancement of all three thermoelectric properties. *J. Mater. Chem. A*, 2(1):73–79, nov 2014.

[141] Noboru Yamada. Origin, secret, and application of the ideal phase-change material GeSbTe. *Phys. Status Solidi Basic Res.*, 249(10):1837–1842, 2012.

[142] Joseph P. Heremans, Christopher M. Thrush, and Donald T. Morelli. Thermopower enhancement in PbTe with Pb precipitates. *J. Appl. Phys.*, 98(6):063703, sep 2005.

[143] J E Parrott. The Theory of the Nernst Effect in Semiconductors. *Proc. Phys. Soc.*, 71(1):82–87, 1958.

[144] Jared B. Williams and Donald T. Morelli. Understanding the superior thermoelectric performance of Sb precipitated Ge17Sb2Te20. *J. Mater. Chem. C*, 4(42):10011–10017, 2016.

[145] Yichi Zhang, Je Hyeong Bahk, Joun Lee, Christina S. Birkel, Matthew L. Snedaker, Deyu Liu, Hongmei Zeng, Martin Moskovits, Ali Shakouri, and Galen D. Stucky. Hot carrier filtering in solution processed heterostructures: A paradigm for improving thermoelectric efficiency. *Adv. Mater.*, 26(17):2755–2761, 2014.

[146] S. N. Zhang, T. J. Zhu, S. H. Yang, C. Yu, and X. B. Zhao. Improved thermoelectric properties of AgSbTe2 based compounds with nanoscale Ag2Te in situ precipitates. *J. Alloys Compd.*, 499(2):215–220, 2010.

[147] Zahra Zamanipour and Daryoosh Vashaee. Comparison of thermoelectric properties of p-type nanostructured bulk Si0.8Ge0.2 alloy with Si0.8Ge0.2 composites embedded with CrSi2 nano-inclusisons. *J. Appl. Phys.*, 112(9):0–9, 2012.

[148] T. H. Zou, X. Y. Qin, D. Li, G. L. Sun, Y. C. Dou, Q. Q. Wang, B. J. Ren, J. Zhang, H. X. Xin, and Y. Y. Li. Simultaneous enhancement in thermoelectric power factor and phonon blocking in hierarchical nanostructured beta-Zn4Sb3-Cu3SbSe4. *Appl. Phys. Lett.*, 104(1):013904, jan 2014.

[149] David J. Bergman and Leonid G. Fel. Enhancement of thermoelectric power factor in composite thermoelectrics. *J. Appl. Phys.*, 85(12):8205, 1999.

[150] Yu Zhang, Lihua Wu, Jiye Zhang, Juanjuan Xing, and Jun Luo. Eutectic microstructures and thermoelectric properties of MnTe-rich precipitates hardened PbTe. *Acta Mater.*, 111:202–209, jun 2016.

[151] H J Wu, L D Zhao, F S Zheng, D Wu, Y L Pei, X Tong, M G Kanatzidis, and J Q He. Broad temperature plateau for thermoelectric figure of merit ZT>2 in phase-separated PbTe0.7S0.3. *Nat Commun*, 5:4515, 2014.

[152] Yubo Luo, Junyou Yang, Qinghui Jiang, Weixin Li, Dan Zhang, Zhiwei Zhou, Yudong Cheng, Yangyang Ren, and Xu He. Progressive Regulation of Electrical and Thermal Transport Properties to High-Performance CuInTe 2 Thermoelectric Materials. *Adv. Energy Mater.*, 6(12):1600007, jun 2016.

[153] Han Li, Xinfeng Tang, Qingjie Zhang, and Ctirad Uher. High performance InxCeyCo4Sb12 thermoelectric materials with in situ forming nanostructured InSb phase. *Appl. Phys. Lett.*, 94(10):102114, mar 2009.

[154] T. H. Zou, X. Y. Qin, D. Li, G. L. Sun, Y. C. Dou, Q. Q. Wang, B. J. Ren, J. Zhang, H. X. Xin, and Y. Y. Li. Simultaneous enhancement in thermoelectric power factor and phonon blocking in hierarchical nanostructured β-Zn4Sb3-Cu3SbSe4. *Appl. Phys. Lett.*, 104(1):013904, jan 2014.

[155] Felix Fahrnbauer, Stefan Maier, Martin Grundei, Nadja Giesbrecht, Markus Nentwig, Tobias Rosenthal, Gerald Wagner, G. Jeffrey Snyder, and Oliver Oeckler. Heterostructures of skutterudites and germanium antimony tellurides structure analysis and thermoelectric properties of bulk samples. *J. Mater. Chem. C*, 3(40):10525–10533, aug 2015.

[156] Felix Fahrnbauer, Daniel Souchay, Gerald Wagner, and Oliver Oeckler. High Thermoelectric Figure of Merit Values of Germanium Antimony Tellurides with Kinetically Stable Cobalt Germanide Precipitates. *J. Am. Chem. Soc.*, 137(39):12633–12638, oct 2015.

[157] Jared B. Williams and Donald T. Morelli. Using Ge Secondary Phases to Enhance the Power Factor and Figure of Merit of Ge17Sb2Te20. *J. Electron. Mater.*, 46(5):2652–2661, may 2017.

[158] Suresh Perumal, Subhajit Roychowdhury, Devendra S. Negi, Ranjan Datta, and Kanishka Biswas. High Thermoelectric Performance and Enhanced Mechanical Stability of p-type Ge1-xSbxTe. *Chem. Mater.*, 27(20):7171–7178, oct 2015.

[159] Suresh Perumal, Subhajit Roychowdhury, and Kanishka Biswas. Reduction of thermal conductivity through nanostructuring enhances the thermoelectric figure of merit in Ge 1x Bi x Te. *Inorg. Chem. Front.*, 3(1):125–132, 2016.

[160] Tapan Chatterji, C. M. N. Kumar, and Urszula D. Wdowik. Anomalous temperature-induced volume contraction in GeTe. *Phys. Rev. B*, 91(5):054110, feb 2015.

[161] Hong Zhu, Wenhao Sun, Rickard Armiento, Predrag Lazic, and Gerbrand Ceder. Band structure engineering through orbital interaction for enhanced thermoelectric power factor. *Appl. Phys. Lett.*, 104(8):082107, feb 2014.

[162] E. M. Levin, S. L. Bud'ko, and K. Schmidt-Rohr. Enhancement of Thermopower of TAGS-85 High-Performance Thermoelectric Material by Doping with the Rare Earth Dy. *Adv. Funct. Mater.*, 22(13):2766–2774, jul 2012.

[163] E.M. Levin, C. Cooling, S.L. Bud'ko, W.E. Straszheim, and T.A. Lograsso. Crystal structure, magnetization, 125Te NMR, and Seebeck coefficient of Ge49Te50R1 (R=La, Pr, Gd, Dy, and Yb). *Mater. Chem. Phys.*, 192:58–66, 2017.

[164] Tobias Rosenthal, Philipp Urban, Kathleen Nimmrich, Ludwig Schenk, Johannes de Boor, Christian Stiewe, and Oliver Oeckler. Enhancing the Thermoelectric Properties of Germanium Antimony Tellurides by Substitution with Selenium in Compounds GenSb2(Te1-xSex)n+3(0< x<0.5;n>7). *Chem. Mater.*, 26(8):2567–2578, 2014.